Final Report of the P̄ANDA PID TAG

G. Schepers, GSI Darmstadt, **et al.**

Contents

1 Introduction

The $\bar{\text{P}}$ANDA ([1]) PID TAG (Particle Identification Technical Assessment Group) was installed to give to the collaboration a complete set of parameters for an optimal set of particle detectors. The task given to this TAG is described in more detail:

Subject

- − Requirements from physics
- − Evaluate potential of each subsystem
- − Matching of systems

Deliverables

- − Definition of global PID scheme
- − Optimized set of detectors and parameters

This list reflects roughly the structure of the PID TAG work and of this report. In an additional subsection the tools available for the PID TAG work are presented and explained (see also [2]) . The PID TAG evaluated the necessity of mapping the "Separation Power" in dependence of the momentum and the polar angle of the reaction products which is described in section 4.1. Since a "full simulation" was not available to calculate the performance of all the sub detectors, the TAG gathered parameterizations of the single sub detectors which went into a "Fast Simulation" explained in section 4.3. For single physics channels a "Full Simulation" was used.

Amongst others some important questions to solve were:

- PID informations from the Central Tracker (Strawtube Tracker (STT) or Time Projection Chamber (TPC))

- PID with and with out a Barrel ToF detector

- PID with and with out an Forward Endcap Cherenkov, and with different forms (Focusing Disc DIRC, Time of Propagation Disc DIRC and Proximity RICH)

- PID with and with out a Forward RICH

The PID TAG had about 10 presence meetings and over 20 online meetings. First PID subsystems were defined. Each subsystem has its responsible representative. Each representative had a replacement of his own group to guarantee always the same level of knowledge in all subsystems. For special subjects experts were asked to present informations in the meeting or to give answers to questions which arose.

The members of the TAG and their special responsibilities are listed at the end of the document (section 9).

2 Physics Requirements

The HESR (High Energy Storage Ring) of the new FAIR (Facility for Antiproton and Ion Research) project provides an Antiproton beam of high resolution (down to $\Delta p = 1 \times 10^{-5}$) and intensity from 1.5 GeV/c to 15 GeV/c momentum.

This offers the unique possibility of investigating a broad filed of physics. The vast variety of reaction types from meson-production over Charmonium decays to Hyper nuclear reactions demands a complete and compact detector system.

The physics requirements to the detectors are:

- to cover the full angular range of the physics products

- to detect all momenta of the reaction products

- to separate particle types with a defined level of separation over the full range of momenta of the reaction products.

The full solid angle can only be covered by the full set of detectors. Sometimes the momentum coverage has to be fulfilled by a combination of two or even three sub detectors.

The rich experimental program can only be pursued with a universal and hermetic detector capable of detecting charged and neutral particles with nearly 4 solid angle coverage and high resolution. The basic elements are:

Hidden-charm physics and the search for exotics require the concurrent detection of lepton pairs as well as good kaon identification and high efficiency for open-charm final states. In addition, the detection of low energy photons, either from radiative decays and/or background channels, is extremely important. Thus, muon detection capability and a highly-segmented low-threshold electromagnetic calorimeter are important for the tagging and precise reconstruction of hidden-charm and the reduction of background. Good vertex recognition and particle identification for charged kaons from very low energies up to a few GeV/c is mandatory to reconstruct light hadronic and open charm final states.

The detector must withstand large radiation dosage from hadrons emitted from the spallation process when using nuclear targets. Spallation products are dominated by neutrons down to thermal energies.

The specific demands for experiments with a secondary target require good detection of antihyperons and low momentum K+ in the forward region. A compact high resolution solid state tracker for absorption and tracking of low momentum hyperons at large angles is needed. The geometry of the secondary target is determined by the short mean life time of the Ξ^- of only 0.164 ns. A high resolution and highefficiency Ge-array for γ-ray detection is envisaged in order to measure radiative transitions.

Open-charm spectroscopy and electromagnetic reactions have similar demands as are envisaged in the hidden-charm and exotics programs that the decay of a charmed hadron releases rather high pt (up to 1.5 GeV/c) as compared to light and even strange meson decays. This leads to large opening angles of particles in the laboratory reference frame.

Channel	Final state	Related to detector
$\bar{p}p \rightarrow (n)\pi^+\pi^-$	$(n)\pi^+\pi^-$	EMC
$\bar{p}p \rightarrow \psi(3770) \rightarrow D^+D^-$	$2K\,4\pi$	DIRCs, ToF, STT/TPC
$\bar{p}p \rightarrow \eta_c \rightarrow \phi\phi$	4K	DIRCs, STT/TPC
$\bar{p}p \rightarrow D_S D_{S0}^*(2317)$	$\pi^\pm K^+K^-$	DIRCs, STT/TPC
		muon
		Forward RICH

Table 1: Benchmark channels to evaluate the performance of the different PID detectors.

116 For the single subsystems benchmark-channels had to be identified (Table 1) and simulated.

117 At $\bar{\text{P}}$ANDA 2×10^7 reactions per second with up to 10 charged particles per reaction have to be
118 digested by the detectors.

3 PID Subsystems

The different behavior of charged particles traversing active and passive detector material can be used to identify (on a probabilistic level) the nature of a charged particle. The PID detectors used in PANDA take advantage of the following effects:

- Specific Energy Loss. The mean energy loss of charged particles per unit length, usually referred to as dE/dx, is described by the Bethe-Bloch equation which depends on the velocity rather than momentum of the charged particle.

- Cherenkov Effect. Charged particles in a medium with refractive index n propagating with velocity $\beta > 1/n$ emit radiation at an angle $\Theta_C = arccos(1/n\beta)$. Thus, the mass of the detected particle can be determined by combining the velocity information determined from Θ_C with momentum information from the tracking detectors.

- Time-of-flight. Particles with the same momentum, but different masses travel with different velocities, thus reaching a time-of-flight counter at different times relative to a common start.

- Absorption. A thick layer of passive material absorb most particles due to electromagnetic (e+e-, γ) or hadronic interactions (all charged and neutral hadrons). After a certain amount of material only muons and neutrinos survive. The muons can then be detected easily with any kind of charged particle detector, depending on the desired speed and resolution.

The group of subsystems building the particle identification system of $\bar{\text{P}}$ANDA are listed with growing distance to the Target point:

- Time Projection Chamber

- Time of Flight

- Barrel DIRC

- Barrel Calorimeter

- Forward Cherenkov

- Forward Calorimeter

- Muon Counter

3.1   Central Tracker

Since the central tracker depending on the detector type provides as a surplus a dE/dx-information it can give important help for the particle identification in the low momentum regime (¡700MeV). For PANDA there are two options for the central tracker which is a Straw Tube Tracker on the one hand and a Time Projection Chamber on the other hand.

3.1.1 Micro Vertex Detector (MVD)

The Micro Vertex Detector will provide precise space point measurements for particle tracking and the reconstruction of decay vertices. The detector will be build of state-of-the-art silicon semiconductor detector layers of pixel and strip type. A schematic overview is given in figure 1.
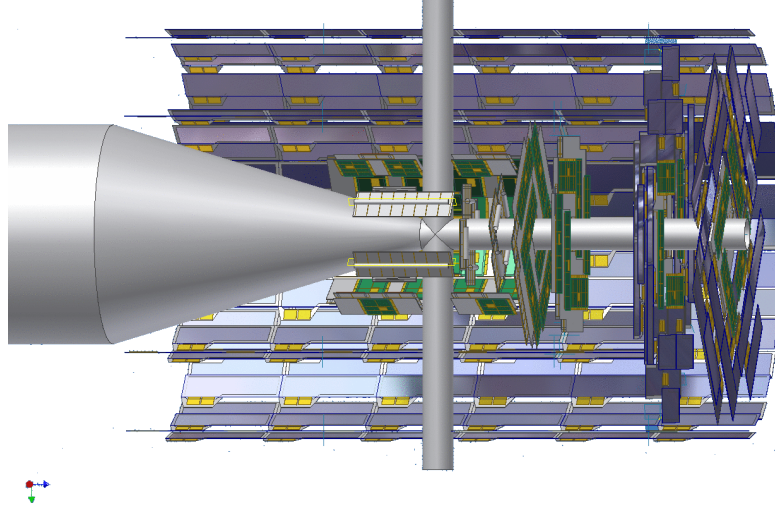

Figure 1: Artist view of the MVD design together with beam and target pipe cross. A half shell of the barrel section has been removed for insight. The inner detector elements (green) are pixel sensors, the outer (blue) are strip sensors.

Although the number of reconstructed MVD hit points per track is limited to 4 in the barrel section and 5-6 in the forward domain the energy loss information provided by the readout electronics can be used as part of the particle identification decision. The ability of separating different particle species rely on an accurate energy loss information and a good knowledge of the track position with respect to the sensors. Figure 2 shows the computed dE/dx information for tracks of different particle types in a momentum range from 50 MeV/c to 1.2 GeV/c.

In general the MVD might be able to contribute to the global PID for particle momenta below $\approx$ 600 MeV/c. Protons (highest band) and kaons (middle) can be separated from pions, muons and electrons (lowest band). In Figure 2,b) a typical dE/dx signal for protons with momentum of 400 MeV/c is shown. The signal can only be described sufficiently by a convolution of a gaussian and a Landau component by using:

$$w(s) = \int L(x)\, G(s-x)dx \tag{1}$$

The used parametrizations are

$$G_\sigma(x) = \frac{1}{\sqrt{2\pi}\sigma} e^{-x^2/\sigma^2} \tag{2}$$

for the Gauss distribution and

$$L_\tau(x) = \frac{1}{\pi\tau} \int_0^\infty e^{-t(\ln t - x/\tau)} \sin(\pi t)dt \tag{3}$$
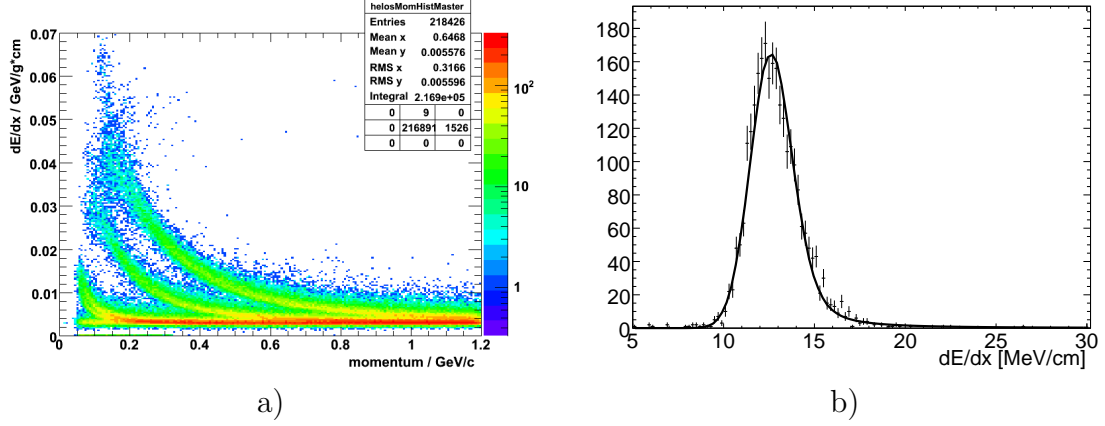
Figure 2: Energy loss information for different particle species and its dependence on momentum (a). The upper band corresponds to protons, whereas the middle band show kaons and the lowest band is a superposition of pions, muons and electrons. Part (b) shows and individual fit of the dE/dx signal from protons with a momentum of 400 MeV/c.

for the scaled Landau distribution. The sensors, where the deposited charge is collected, are very thin silicon devices of typical thicknesses of $200 - 300 \ \mu m$. Therefore the energy signal will be dominated by Landau fluctuations, which can not be fully suppressed by a truncated mean method. The remaining tail for the proton signal is still visible in figure 2,b). The dE/dx signal can be than described by only three parameters,the Gauss width σ_G , σ_τ respectively for the Landau width and s, which is the most probable value of the Landau distribution.

The dE/dx bands for individual particle types are following the well known Bethe-Bloch relation given in equation 18 in section 4.6. The method described here makes use of a full detector simulation using a combined tracking of the MVD and the outer tracking detectors. To very low momenta the momentum uncertainty increases, which causes a widening of the individual bands. In order to estimate the separation ability the momentum axis has been divided in 25 MeV/c wide bins and for each bin the shape of the the dE/dx distribution has been determined. The momentum dependence of the three parameters σ_G, σ_τ and s was input for the probability for each particle type. Based on the obtained parametrizations for each particle type and each track the probability was calculated and input for the global PID decision.

The likelihood for proton trajectories is shown in Figure 3. The upper picture shows the calculated proton probability and its dependence with momentum. The figure shows additional the probability to misidentify the track as kaon (lower left), or pion (lower right) respectively. Muons and electrons can not further separated from each other and their probability is equal to the pion case. The calculation takes the full convolution integral into account which causes a smearing to lower likelihood values apart from the maximum value.

As explained above the calculation was done for fully reconstructed single particle events under the assumption of equally abundance[1]. Several additional error sources have not been considered and will be subject to further investigation. The properties of the frontend electronics are not yet fully fixed and an additional uncertainty ΔdE was omitted. This is usually in the order of a few percent but in connection with the gain of the energy measurement of the frontend. The sensors

---

[1]This is not true for most physics channels and in particular for annihilation background, e.g. strange production is suppressed, but a common way to compare directly the efficiency for particular particle types.
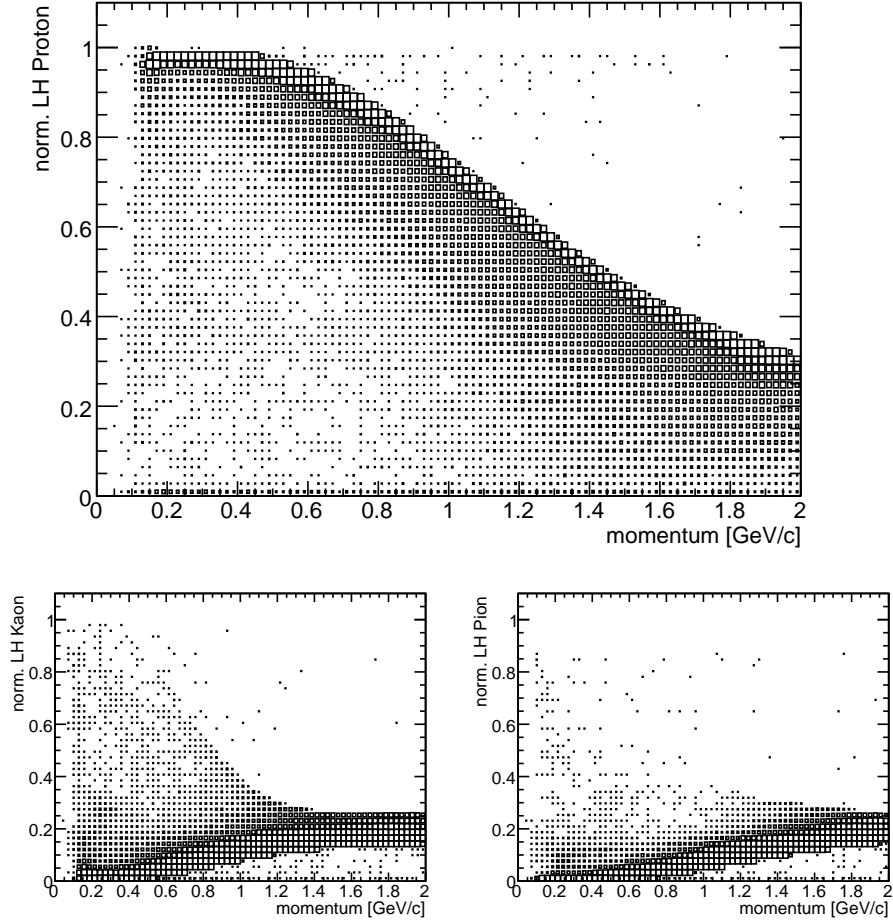
Figure 3: Computed normalized likelihood for proton tracks in a momentum range $p = 0.1 \ldots 2.0$ GeV/c. The upper picture show the proton probability, whereas the lower left shows the kaon misidentification probability and the lower right the pion miss identification, respectively.)

were assumed to be perfectly aligned. The position calibration in the final experiment has to be in the order of the hit reconstruction accuracy in order to avoid a larger additional smearing.

The MVD can contribute to the global PID in the momentum region below 1 GeV/c to separate protons and kaons from the other particle species. It is therefore together with the outer tracking detector complementary to the DIRC measurement and can improve the global PID information.

3.1.2 Time Projection Chamber (TPC)

The working principle of a GEM-based TPC and the geometrical design of the PANDA TPC [1] are sketched in Figs. 4 and 5. Charged particles traversing the detector volume ionize the counting gas and an electric field separates positive ions from electrons. The cylinder axis of the TPC coincides with the direction of the electrical field lines and also the direction of the solenoid magnetic field of the target spectrometer. The primary electrons are guided towards an amplification stage, which consists of a triple-GEM stack. No gating grid is foreseen for the PANDA TPC to allow a continuous operation at the HESR antiproton storage ring. In order to keep the build-up of space charge inside the drift volume at a minimum, the back flow of slow ions from the amplification stage has to be suppressed as much as possible. GEM foils [3] offer an intrinsic ion suppression if the settings of the whole stack are optimized accordingly. A continuous readout including online tracklet reconstruction is envisaged for the TPC.

In order to accommodate the target pipe, the TPC is split into two half-cylinders of a length of 150 cm. The inner and outer radius is 15 cm and 42 cm, respectively. 65 000 to 100 000 pads of an area of 4-6 mm^2 are planned. A Ne/CO$_2$ gas mixture (90/10), possibly with a small admixture of CH$_4$, and a gain of a few thousand are furthermore foreseen. The drift field is 400 V/cm. Under these conditions $\approx$ 50-100 energy loss measurements per track are feasible. This allows, in combination with a truncated mean algorithm, the identification of charged particles via their mean energy loss per track length dE/dx (Bethe-Bloch-formula, see equation 18). The TPC therefore contributes significantly to the overall PID performance of PANDA, in particular in the momentum regime below 1 GeV/c^2. In Fig. 6 the energy loss distributions for different particle types are shown up to 1.5 GeV/c^2. The plot has been obtained from the "Fast Simulation" described in section 4.3 assuming a dE/dx resolution of 8% for the TPC (cf. table 10).
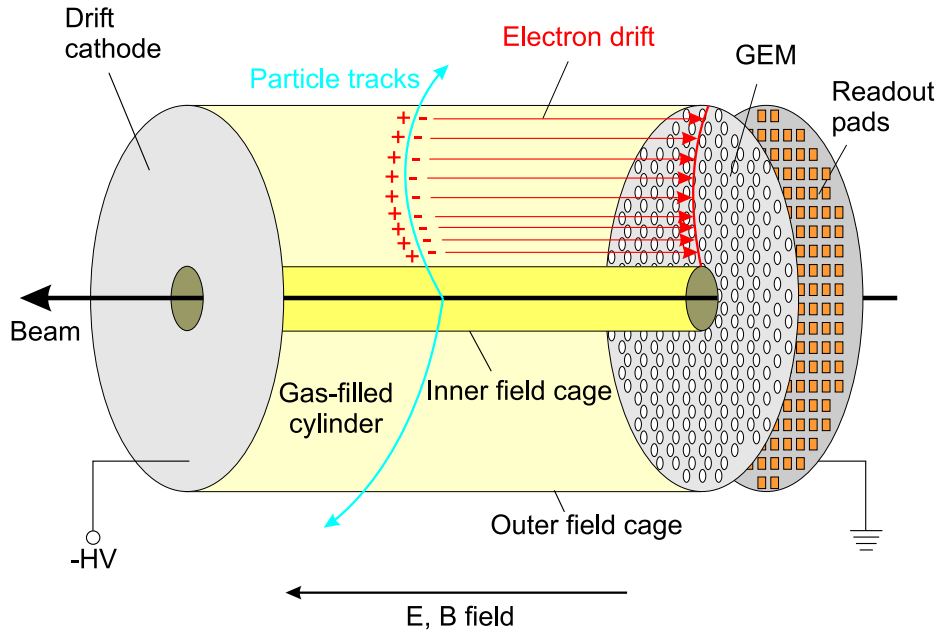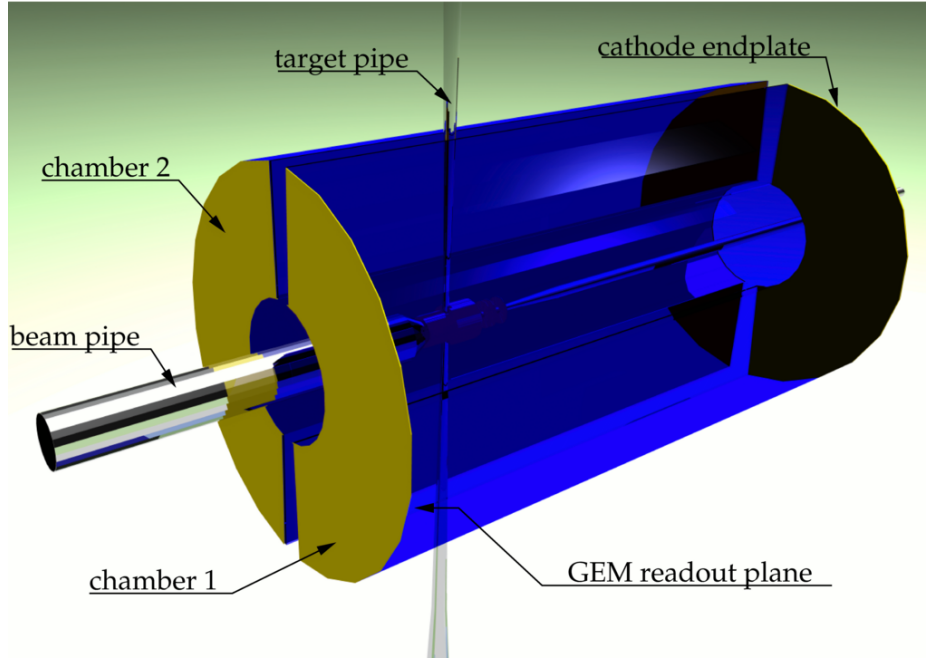

Figure 4: Working principle of a GEM-TPC (see text).

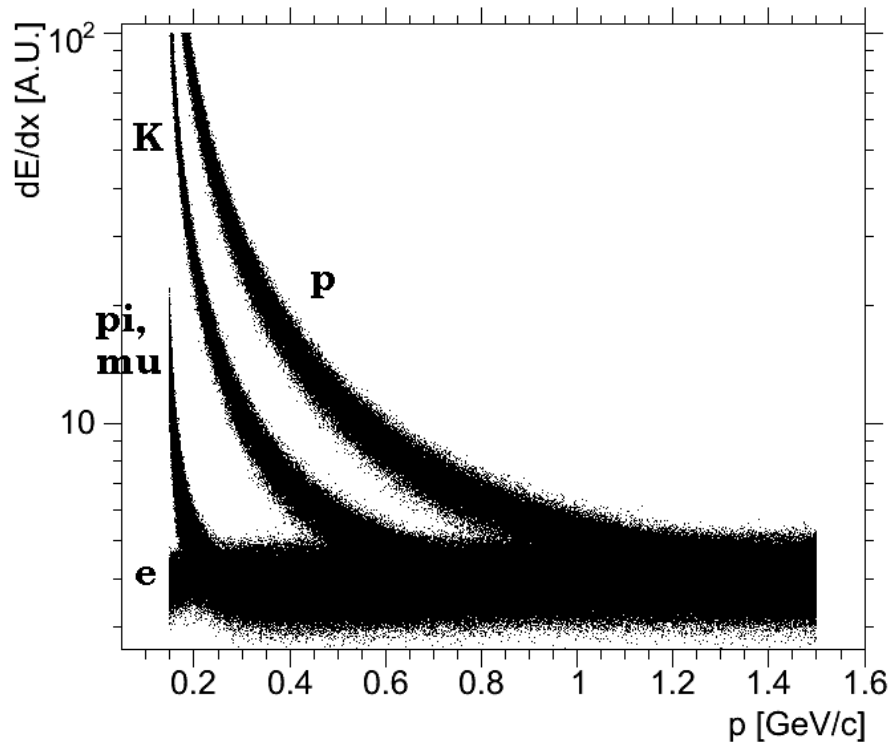Figure 5: Geometry of the PANDA TPC; for further details see text and [1].

Figure 6: Energy loss in the TPC vs. particle momentum up to $1.5\,\mathrm{GeV}/c^2$.

3.1.3 Straw Tube Tracker (STT)

The single straw tube is a gas filled tube with a wire along its axis. The wire is the anode the inner conductive wall is the cathode and a high voltage of some kV is applied between the two. An electric field is then present in the gas filled area: when a charged particle transverses it, ionization takes place; the electrons drift toward the wire, while the ions drift toward the wall. Once the electrons are near enough to the wire ($\simeq 50\mu m$), an avalanche multiplication takes place with an amplification of $10^4 - 10^5$ of the primary charge signal which allows the readout of the electric signal. Concerning the gas choice, it is necessary to find a compromise between the material budget, which must be small to minimize the multiple scattering, and a good spatial resolution. An Ar/CO_2 gas mixture (90/10) has been chosen, since the simulations with Garfield [4] have demonstrated that even though He would give a lower material budget, it would worsen the resolution. The arrival time of the signal defines the drift radius and the charge collected is proportional to the particle energy lost by ionization.

The Straw Tube Tracker consists of an ensemble of 150 cm long drift tubes, arranged in an hexagonal shape around the beam axis. The present solution consists of about 4204 tubes, disposed in double layers, 2800 of which parallel to the beam axis, the others inclined with respect to the beam axis (skewed tubes); the skewed tubes are necessary to allow the z coordinate determination. The present layout of the Straw Tube tracker is shown in fig.7. The tubes in two consecutive layers are staggered in order to resolve the left-right ambiguity.

The geometric characteristics used for the simulations are summarized in tab.2. Among the STT advantages we recall:

- the small signal's cross-talk;

- the insensitivity of neighboring straws in case of broken wires;

- the high mechanical stability if the straws are arranged in close-packed multi-layers;

STT characteristics		
internal radius	15	cm
external radius	42	cm
skew angle	3°	
tube wall thickness	30	μm
tube diameter	1.006	cm
tube standard length	150	cm
wire diameter	20	μm
wall material	mylar	
wire material	gold plated W	
gas mixture	2 atm argon Ar/CO_2 (90/10)	
transparency X/X_0	$< 1\%$	
r-ϕ plane resolution	$< 100~\mu m$	

Table 2: Dimensions and material budget of the Straw Tube detector. X/X_0 is the thickness expressed as the radiation length fraction. The quantities listed in this table are under study and the final layout of the STT could be different.
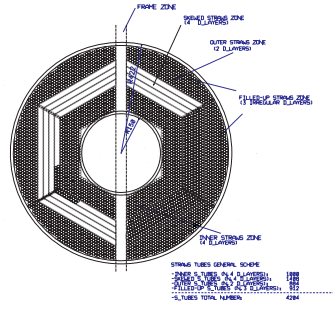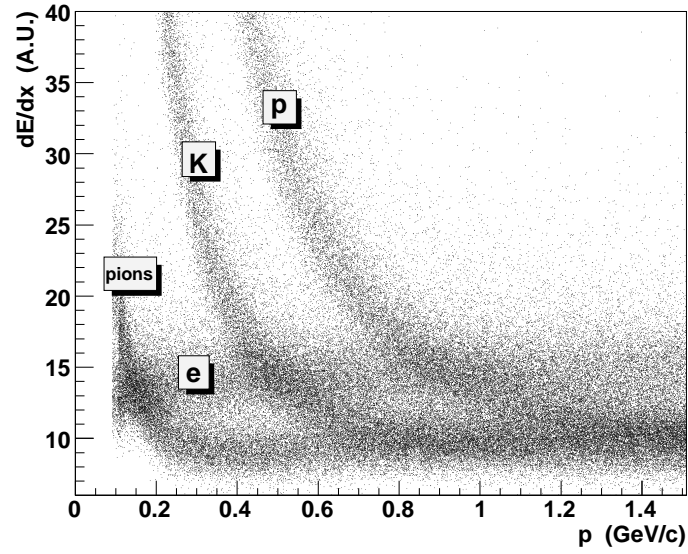
Figure 7: Present layout of Straw Tube Tracker

Figure 8: Energy loss by a truncated mean algorithm in a layer of 22 straw tubes vs. particle momentum. The fluctuations in charge collection and the uncertainty in the drift radius are taken into account

245   • the high tracking efficiency;

246   • the good spatial resolutions

247   • the high rate capability.
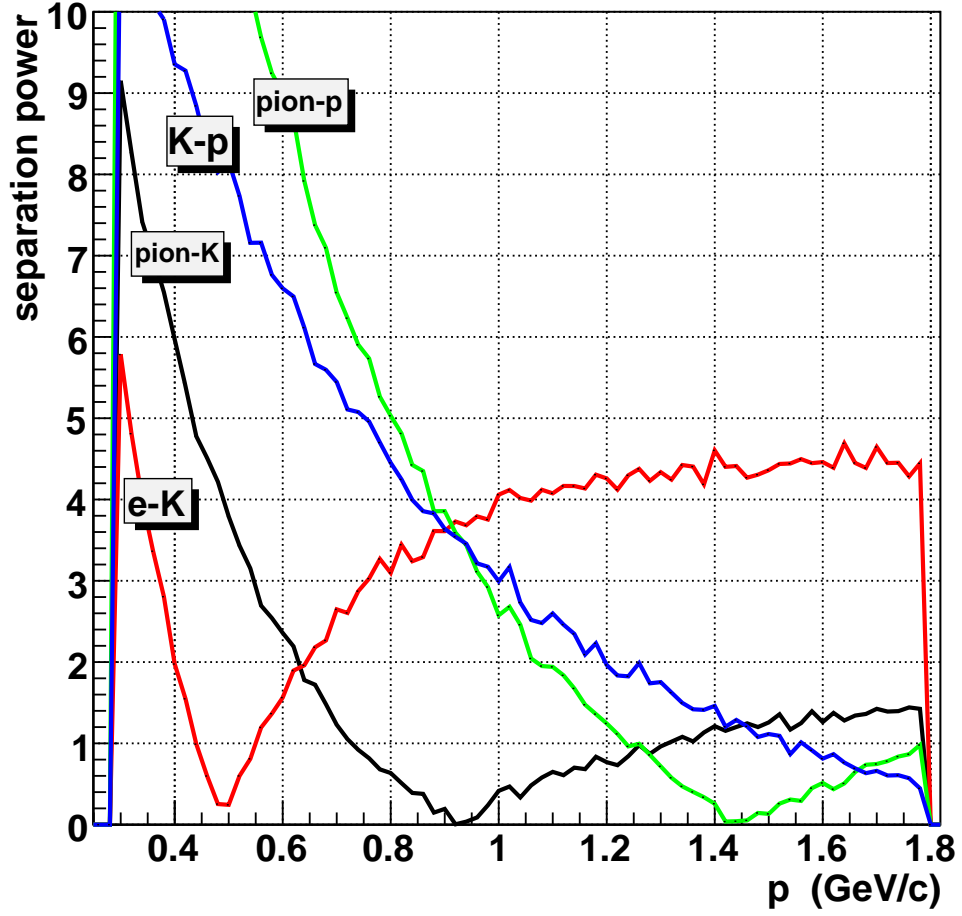
Figure 9: Separation power curve corresponding to the truncated mean data of fig 8

The STT detector allows a maximum of 24 energy loss measurements. A detailed simulation of the tube signals and of the charge collection has shown that, in spite of this poor sampling, with the truncated mean algorithm some capability of particle identification exists below 1 GeV/c^2. The result of a sampling of 22 tubes, shown in figure 8 and figure 8, demonstrates that in principle also the STT detector could contribute to the low energy PID. The PID studies with the STT detector integrated in the general structure are under way.

3.2 Time of Flight (ToF)

The Barrel Time-of-Flight detector (TOF) has to be placed inside solenoidal magnet and provide identification for soft particles at large polar angles from 22 to 140 degrees. The recently developed timing Resistive Plate Chambers (RPC) represent currently the optimal choice for Barrel TOF detector that in principle offers the required resolution of better than 70 ps. The identification of pions, kaons and protons is possible up to few GeV/c.

A stable operation of the such RPCs was observed in extensive tests during many years in various experiments. The RPCs were found to be fully efficient and low-noise chambers. One of useful feature of the RPC is its immunity to magnetic field. Proposed here design is based on experience obtained during work for the HARP experiment[5].
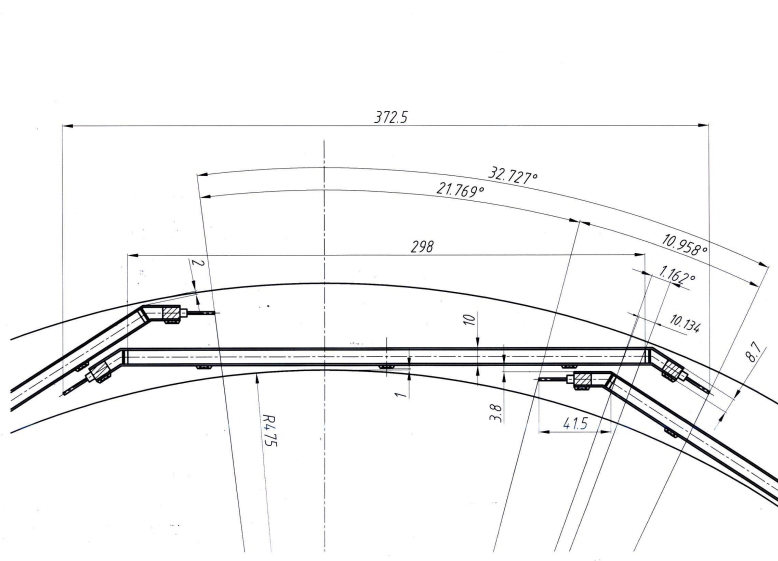

Figure 10: Possible arrangement of 11 barrel RPCs.

The RPC-TOF consists of 11 modules arranged around TPC (or STT) in the way shown schematically in fig.10 Length of each module is $\sim 190\ cm$, width of its active area is $\sim 30\ cm$. Each module is multi-gap glass RPC placed inside aluminium case. To have full coverage in azimuthal angle, active areas of neighbour modules will be overlapped as it shown in fig.10. PCB with FEE electronics will go along both long sides.

Because of hard demands on amount of material for the Barrel-TOF detector, variant of four-gap glass RPC was chosen. Beam test [6] of four-gap RPCs has demonstrated that time resolution of $\sim 75\ ps$ can be reached even with old HARP FEE. The RPCs can be made from a "standard" float glass with thickness of 0.6 mm. The gaps between glass plates are kept with spacers made of fishing line. Thickness of the TOF module (including aluminium box) is $X/X_0 \approx 6.0\%$

Each RPC will equipped with 64 strips with double ended readout. Each strip have a length of $\sim 30\ cm$ at 30 mm width. Already existed data[7] on multi-gap RPC with strips (strip length: 95 cm and width: 25mm) inspire a hope that time resolution of 60-70 ps can be reached with double-end readout. Signals will be amplified and digitized at the RPCs to use the Time-Over-Threshold (TOT) method for slewing correction as it was proposed in[8]. Total number of HPTDC channels needed to read all strips is about ~ 1410. The development of the read-out system has to be a major task during $R\&D$ study for the PANDA RPC.

281 Set of eleven TOF modules having total gas volume of ~ 60 liters is operating with a non-flammable
282 gas mixture containing $90\% R134A$, 5% isobutane and $5\% SF_6$. The flows of three gas components
283 are metered with "electronic mass flow meters". At total flow rate of about 200 cm^3/min, a gas
284 exchange of one volume will be every ~ 5 hours. The TOF modules are supplied with gas in
285 groups, say, of four. Each group has its own control and protection systems.

286 Very important question is the rate capability. Since the bulk resistivity of glass is $\sim 10^{13}\Omega \cdot cm$,
287 the rate capability of a glass RPC could bring a potential problem due to the time needed to
288 neutralize the charge deposited on the resistive plates after discharge inside gas gaps. During
289 measurements performed in the GIF test area for the ALICE TOF detector, it was observed
290 that there was no deterioration of the efficiency and the resolution for the ALICE MRPCs up
291 to 1 kHz/cm^2. This result found for 10-gap glass RPC should be well for 4-gap chamber too.
292 The estimations using DPM generator for minimal bias events showed that particle flux in the
293 PANDA barrel for momenta of the incident anti-proton between 1.5 GeV/c and 15 GeV/c is less
294 than 1 kHz/cm^2.

295 **Particle Identification.** The Barrel RPC-TOF provides a particle identification using a mea-
296 surement of a particle arrival time and a momentum and length of a track information from the
297 tracking detectors (TPC or STT). In the PandaRoot framework, we generated events of K, Pi,
298 proton production isotropically through the RPC-TOF with momenta from 0.1 to 2.1 GeV/c.
299 We simulated and reconstructed the events using RPC-TOF, and calculated velocity and squared
300 mass of the particles by formulas: $1/v = t/l$ and $M^2 = P^2(1/v^2 - 1)$. Fig. 11 give results of a
301 particle identification using $1/v$ and M^2 information from the RPC-TOF.
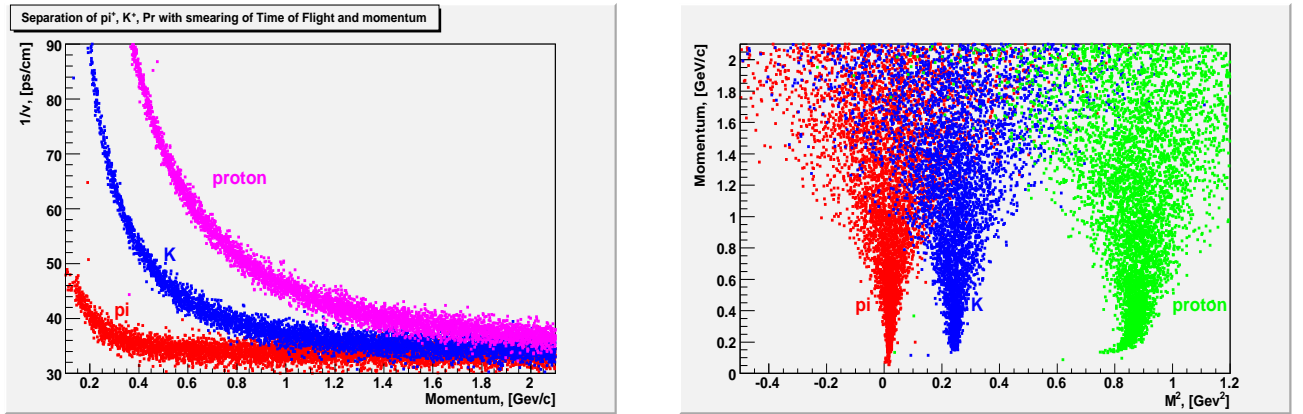
Figure 11: Inverse velocity of particles vs. momentum (left figure) and momentum of particles vs. squared mass reconstructed with RPC-TOF (right figure).

302 **Separation power.** Fig.12 shows calculation of a separation power. Difference between time of
303 flight of two different particles divided by the TOF resolution, $(t_1 - t_2)/\sigma_t$ ("separation power"),
304 is presented in this figure for different pairs of particles for the most hard case - for polar angle
305 $\Theta = 90^0$, and for polar angle $\Theta = 30^0$. The computation was done for two values of σ_t: 70 ps
306 and 100 ps.

307 The calculations of the separation power for angle $\Theta = 30^0$ demonstrate that the barrel TOF
308 with resolution of ~ 70 ps will be able identify hadrons with momentum up to few GeV/c. The
309 RPC-TOF providing the particle identification at low momentum can be good supplement to
310 DIRC.
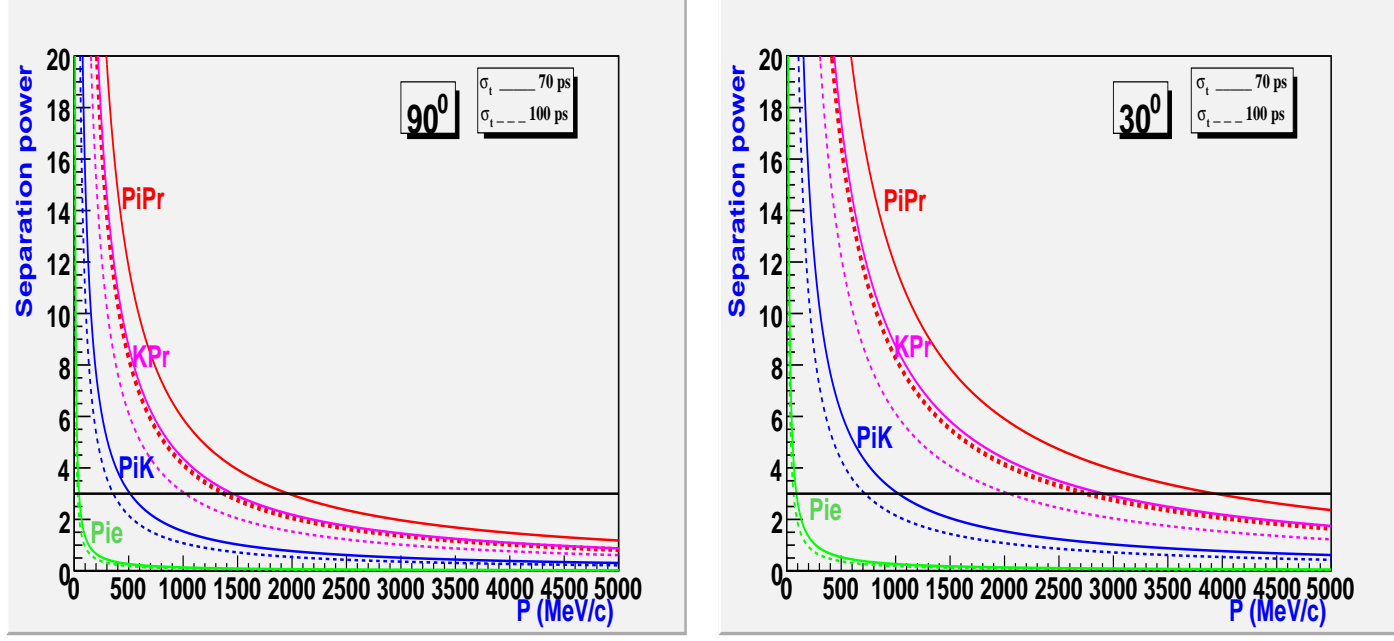
Figure 12: Separation as a function of momentum for polar angles $\Theta = 90^0$ and $\Theta = 30^0$.

Furthermore, the RPC-TOF can help as a reference detector for the one-dimensional DIRC.

In ideal case, the time-of-flight is measured with information from two detectors: start time, t_0, from a reference detector placed somewhere near target and stop time of flight t from the barrel TOF. However, even in case of no start detector, t_0 can be found by fitting measured values of t in multiparticle events with different hypothesis.

3.3   Barrel DIRC

The purpose of the Barrel DIRC (Detection of Internal Reflected Cherenkov photons) is to provide
a particle identification. The mass of the particle can be achieved by combining the velocity
information of the DIRC with momentum information from the tracking detectors. In addition
the distinction between gammas and relativistic charged particles entering the EMC behind the
DIRC is possible.

Basis for the calculations and simulations are the bar dimensions taken from the BaBar DIRC [9].
With the length adapted to the $\bar{\mathrm{P}}$ANDA setup there are quartz bars of $17 \times 35 \times 2300\ mm^3$ and
a distance of 480 mm to the target point. Thus the barrel DIRC covers the solid angle between
22 and 140 degrees. The lower momentum threshold for kaons which produce Cherenkov light is
for an envisaged refractive index of n=1.47 as low as 460 MeV/c for single photon production.
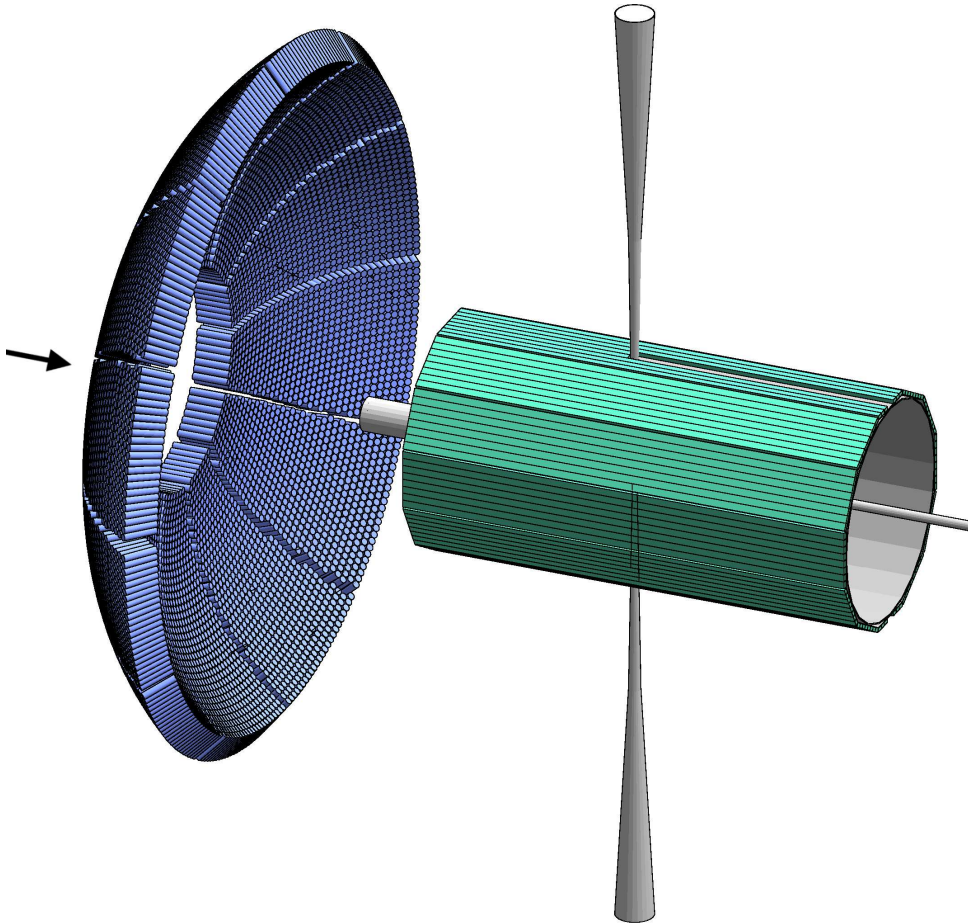For larger photon numbers the threshold increases. With 17mm (of thickness) of fused silica the

Figure 13: The $\bar{\mathrm{P}}$ANDA barrel DIRC as a version of the BaBar-DIRC scaled down in size. The
diameter of the barrel is 1 m.

DIRC bars present approximately 14% of a radiation length to normal incident particles. The
support structure will add 3%.

This design is initially based on the BaBar DIRC [9] (Fig. 13) but at $\bar{\text{P}}$ANDA further improvements of the performance are under development. The combination of the spatial image of the photons with their time of arrival gives access not only to their velocity but also to the wavelength of the photons. Thus dispersion correction at the lower and upper detection threshold becomes possible. Further on the reduction of the photon readout in size and number of photon detectors is envisaged. A lens or a set of lenses at the exit of the quartz bar focus the photons to a focal plane behind a readout volume of about 30 cm length. When this volume is filled with a medium with the same refractive index as the radiator material ($n_{medium}=n_{radiator}=1.5$) additional dispersion effects and other image distortions are avoided.
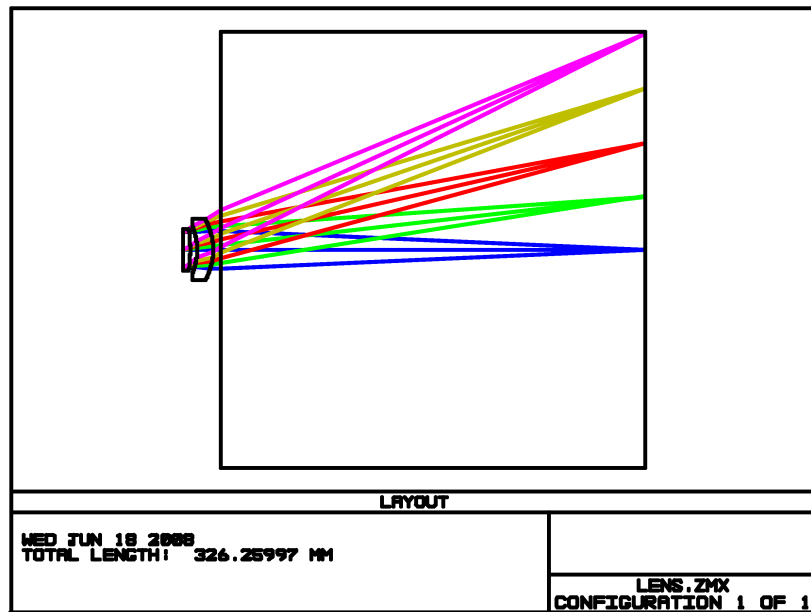
Figure 14: Design of a lens doublet with the optical software ZEMAX. The photon detector box is 300 mm in size.

A major issue is the maintenance of the barrel DIRC. While in the Babar DIRC a removal of the radiator barrel and the photon detector was not foreseen, the PANDA barrel DIRC is planned removable. The disassembly is not planned as default operation during maintenance breaks. Rather the access to other detector parts and the replacement of broken DIRC items need a removal procedure. For that purpose a photon detector smaller in size is favorable. The segmentation of the radiator barrel and the optical joints between radiator and photon detector need also careful design. As shown below the design of the photon detector and its link to the radiator define the geometric dimensions of the latter.

Without having focussing elements each single PMT of the photon detector of the Babar-DIRC can measure photons coming from all of the radiator slabs. The only optical limitation is some space around the beam line which blocks photons from the other side. Introducing focussing elements like lenses or mirrors define a focal surface. A possible orientation of this focal surface would be a flat plane perpendicular to the beam line. In this way each radiator slab focusses

its photons on the same plane and each photon detector element can measure the photons from all radiator slabs. The design with different focal planes for different subsections (bar boxes) of the radiator barrel would cause split ring images caused by photons from one subsection entering the photon detector of another subsection. Blocking these photons reduces the photon detection probability by factors of two to three.

The design of a flat focal plane with a lens doublet consisting out of the glass NLAK33 and fused silica is shown in Fig. 14. This lens combination was designed with the help of the ZEMAX optical program [10] focusses on a flat focal plane at a distance of 30 cm even for large angles of up to 40 degree. The implementation in a ray tracer program (drcprop) within the PANDAROOT frame work is shown by a the results in Fig. 15. The coordinates show the position on the
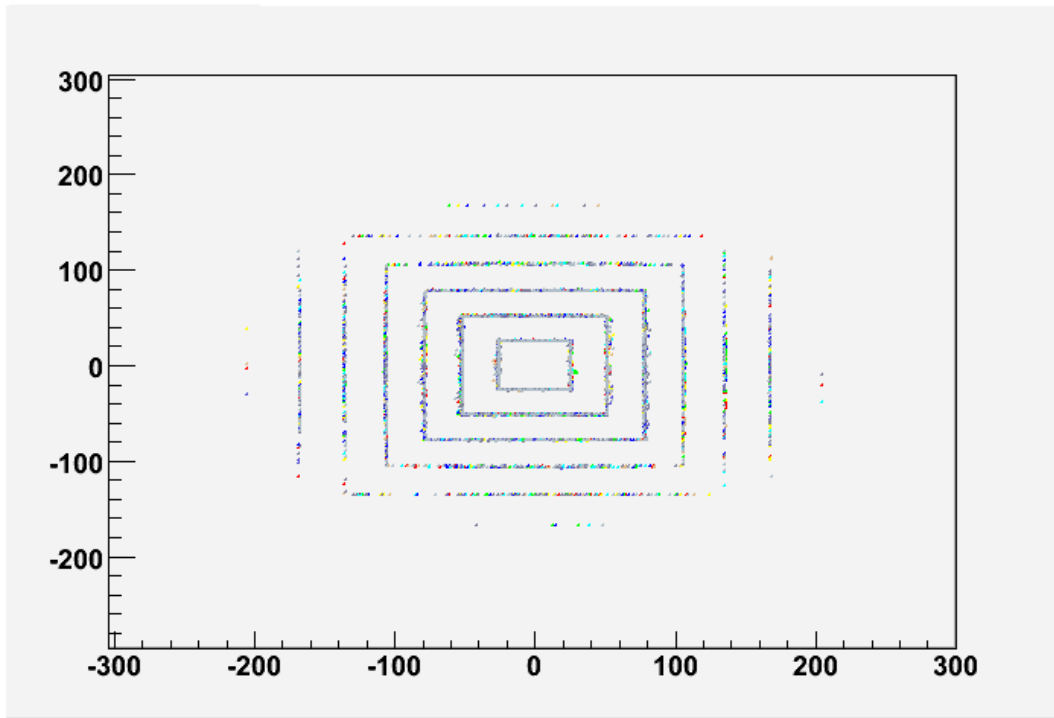
Figure 15: Test pattern of photon images on the focal plane of a photon detector 300mm by 300mm in size. For a perfect image rectangular structures are expected to be observerd.

photondetector in millimeter for photons coming from one of the slabs. In case of a perfect image one expects rectangular structures. The structures are for different opening angles which are from 5- 30 degree in 5 degree steps measured where one of the coordinates is zero. They allow to identify pin-cushion like or barrel like distortions. It is seen that here the photons are focussed up to angles of 30 degree. Large angles hit the side of the lens combination. There is still optimization for the design needed in order to keep the lens combination more compact.

368 3.4 Barrel Calorimeter

3.5 Forward Cherenkov

Two DIRC design options exist for the endcap part of the target spectrometer section. These differ in the photon readout design but both use an amorphous fused silica radiator disc. The endcap detector position covers forward angles of up to $\vartheta = 22°$ excluding an inner rectangular **(is it now elliptical??)** area of $\vartheta_x = 10°$ horizontal and $\vartheta_y = 5°$ vertical half-angles. Simulations using the DPM generator [11] give 1.0±0.8 (at 2 GeV/c) to 2.3±1.8 (at 15 GeV/c) charged particle multiplicity per $\bar{p}p$ interaction emitted from the target vertex into this acceptance.

In such a one-dimensional[2] DIRC type, a photon is transported to the edge of a circular disc while preserving the angle information. Avoiding too much light scattering loss at the surface reflections requires locally (in the order of millimeters) a surface roughness not exceeding several nanometers RMS.

The lower velocity threshold, which is common to both designs, depends on the onset of total internal reflection for a part of the photons emitted in the Cherenkov cone.

There are several boundary conditions for the disc thickness. Radiation length considerations as the detector is upstream of the endcap EMC call for a thin disc. The focussing design is workable with a 10mm thickness (X_0=126mm). Regarding the mechanical stability and handling during polishing, current company feedback recommends 20mm minimum thickness. The resulting thickness of the radiator disc has to be a compromise.

---

[2]Light is only reflected on surfaces of one spatial orientation, here the two disc surfaces both normal to the z axis.

3.5.1   Focussing Disc DIRC

In the Focussing Light guide Dispersion-Correcting design (Figures 16 and 17), when a photon arrives at the edge of the circular or polygonal disc, it enters into one of about hundred optical elements on the rim. Here the two-fold angular ambiguity (up-down) is lifted, the chromatic dispersion corrected and the photon focused onto a readout plane. While the optical element entered determines the ϕ coordinate, measuring the position in the dispersive direction on the focal plane of the focussing light guide yields the θ coordinate.
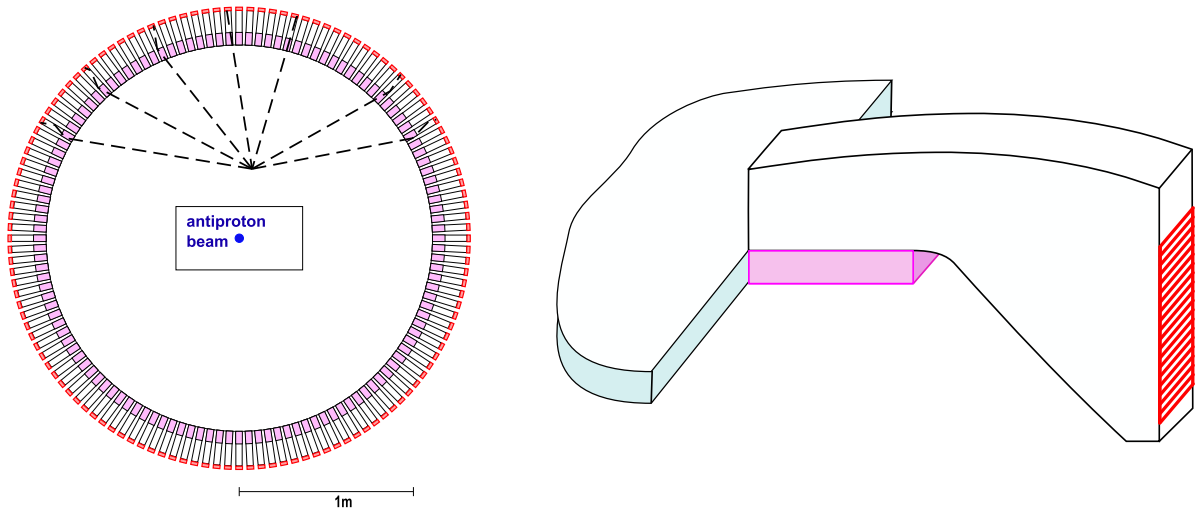
Figure 16: Polygonal disc with focussing light guides attached to the rim used as optical readout components.

Lithium fluoride (LiF) is UV transparent and has particularly low dispersion. Proton beam irradiation of a test sample shows that radiation-produced color centers are confined to sufficiently small wavelength ranges, and are only partially absorbing at the expected $\bar{\text{P}}$ANDA lifetime dose. Hence we believe we can use LiF as a prism element (see Fig. 17) to correct the Cherenkov
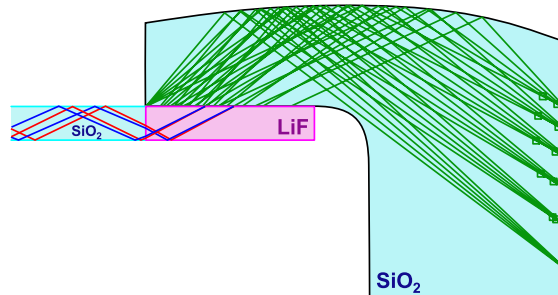
Figure 17: Light guide side view shown with a set of rays used for optimising the light guide curvature. Reflections at the parallel front and back surfaces keep the light inside but do not affect the focussing properties.
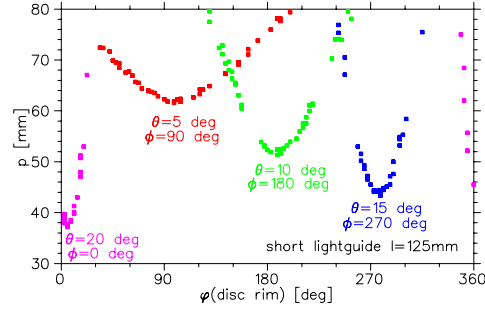
Figure 18: Simulated photon hit pattern for four particles emitted at different angles θ and ϕ from the target vertex.
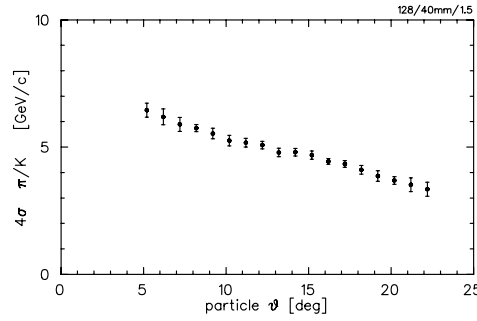
Figure 19: Simulation-derived pion-kaon separation power for a focussing lightguide design with a 15 mm thick amorphous fused silica disc and 0.4 eV photon detection efficiency. Calculation February 2008.

radiation dispersion. The two boundary surfaces, with the radiator disc and the subsequent light guide, make the chromatic dispersion correction angle-independent to first order.

As with the radiator, the light impinging on the inside of the light guide's curved surface undergoes total internal reflection, hence no mirror coating is needed. This reflection makes the focussing also independent of the wavelength.

With the light staying within the dense optical material of the light guide, most of the incoming light phase space from the disc is mapped onto the focal plane with its one-coordinate readout. The focussing surface with cylindrical shape of varying curvature has been optimised to give an overall minimum for the focus spot sizes of the different angles on the focal plane, individual standard deviations being well below 1 mm for the instrumented area.

For an Endcap DIRC detector with 128 lightguides and 4096 detector pixels that fits inside the target spectrometer return yoke, Figure 19 shows the angle-dependent upper momentum limit being about 4–6 GeV/c for 4σ pion-kaon separation within the acceptance ϑ=5°–22°.

Typically all of the 40 detected photons per particle arrive within a 4 ns time window.

Each lightguide can individually be assigned its own 0.4 ns acceptance window. For the pixel size used in this simulation they are contained inside a 40 pixel·ns volume, which at 4K detector pixels amounts to 10 ps detector occupancy time per particle signature.
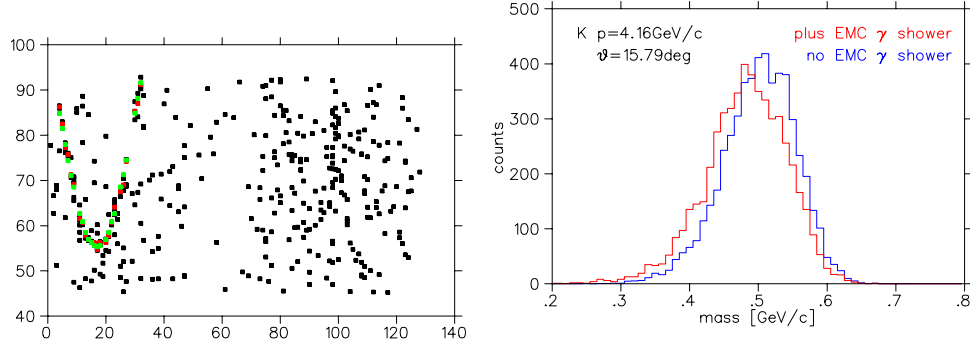
Figure 20: Left: Measured photon distribution from a γ Barrel EMC shower leaking out of the EMC edge towards the Endcap. Photons from one kaon of 4.16GeV/c^2 are added, and the kaon velocity is derived from candidate kaon photons. Right: Analysed mass distributions for kaon with and without shower. The road for kaon photon acceptance is derived from simulations, and within some simulation simplifications the bounds are set such to include (almost) 100 percent of the photons. The systematic offset with the onset of background is though to be caused by the true kaon photon centre of gravity being off the middle of the road interval, probably explained by the coma aberration of the curved lightguide focussing (an improved interval algorithm should help). At this level of background there is a small increase in the width of the reconstructed kaon mass distribution.

The detected photon rate (source: presentation KF 2007-03-27 Genova, 2E7 interactions; scaled to 4K pixels) is 3E7 s^{-1} per PMT and 1E6 s^{-1} per detector pixel.
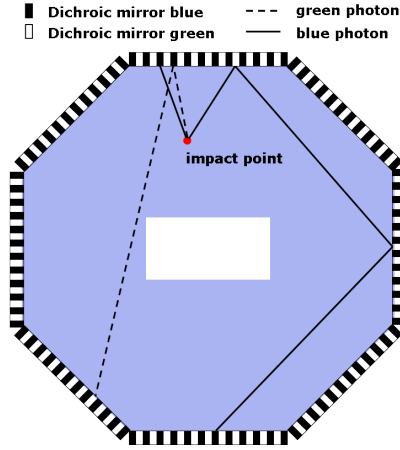
Figure 21: Sketch of the flight-path in the ToP Disc

3.5.2 Time of Propagation Disc DIRC

In the Multi-Chromatic Time-of-Propagation design ([12]) small detectors measure the arrival time of photons on the disc rim, requiring σ_t=30–50 ps single photon time resolution. For any given wavelength, the disc edge is effectively covered alternately with mirrors and detectors. Only due to the resulting different light path-lengths one can determine accurately enough the start reference time, i.e. the time when the initial charged particle enters the radiator, as the stored anti proton beam in the HESR has no suitable time structure to be used as an external time start.

As some of the light is reflected several times before hitting a detector, the longer path lengths allow a better relative time resolution.

The use of dichroic mirrors as color filters allows the use of multiple wavelength bands within the same radiator (the current design suggesting two bands) resulting in higher photon statistics. The narrow wavelength bands minimize the dispersion effects, and the quantum efficiency curve of the photo cathode material could be optimized for each wavelength band individually.

To verify the Principe of TOP DISC the geometry of the disk was implemented into PANDAROOT system and multiple set of Monte-Carlo data was generated with subsequent reconstruction of generated particle type. The fig.22, below shows the DISC implementation into PANDAROOT(left) and generated photons from incident pion and their path from impact point on disc(right).

Reconstruction of particle types using different methods, like Pattern fitting or Slope fitting in two-dimensional(detector number and time of propagation(fig.23) in first case, the calculated arrival time of Cherenkov photons and MC time from GEANT in second case) space yields acceptable separation and low percentage of misidentification. See fig.24 for example in case of Kaons and Pions.

Already first simulations indicate the possible hurdles in particle identifications in DIRC. One of them is the smearing of the patterns from secondary particles, marked as blue points in fig.23. The possible effect from this is depicted on next figures, where we present the misidentification between Kaons and Pions without inclusion of secondaries, see fig.25 and with inclusion of them ,see fig.26.
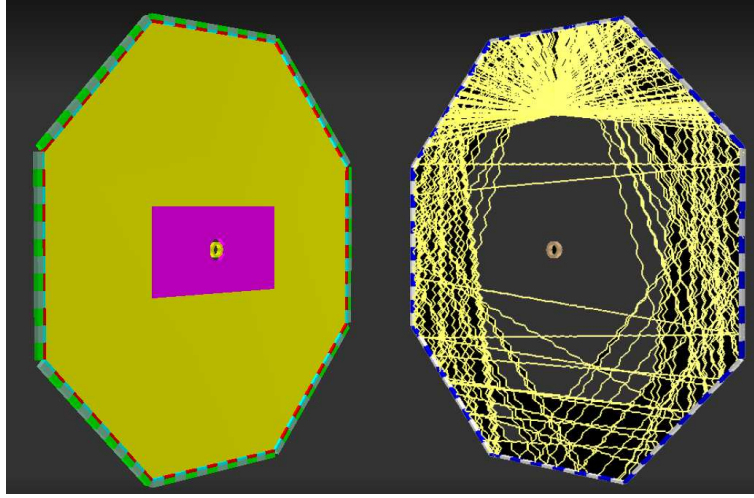
Figure 22: Current scheme of TOP DIRC, 960 photon detectors mounted at rims of octagon disc, located at 180cm from Z=0 point in PANDA coordinate system(left side). On right side disc was hit by 4 GeV/c pion at 15°, the yellow lines shows the path of generated Cherenkov photons. Some of them, if they hit dichroic mirrors, gets reflected and travel longer.

To check the effect of this one and to measure the time resolution of possible candidates for photon detection , $MCP - PMT's$ from Budker Institute of Novosibirsk in real beam situation, we have scheduled TestBeam measurements on DESY site with electron beams in energy range between 1-6 GeV/c. To show that electrons can imitate Cherenkov radiation like Pions we have performed MC simulation of passage of pions and electrons through 2cm thick quartz glass. The resulting spectra are depicted in next fig.27. As we can see $\approx 60\%$ of electrons pass the glass without showering(red spectra), like most of the pions(magenta spectra). In both cases we have secondaries , significantly more from electrons(blue) than from Pions(green). This is the more difficult situation than in case of pions, but for the test, its better to have checks done in difficult case than in simplified ones. The time resolution, that we want achieve in PANDA final design, is a subject for the Lab tests before Test beam. As it will have not only the component coming
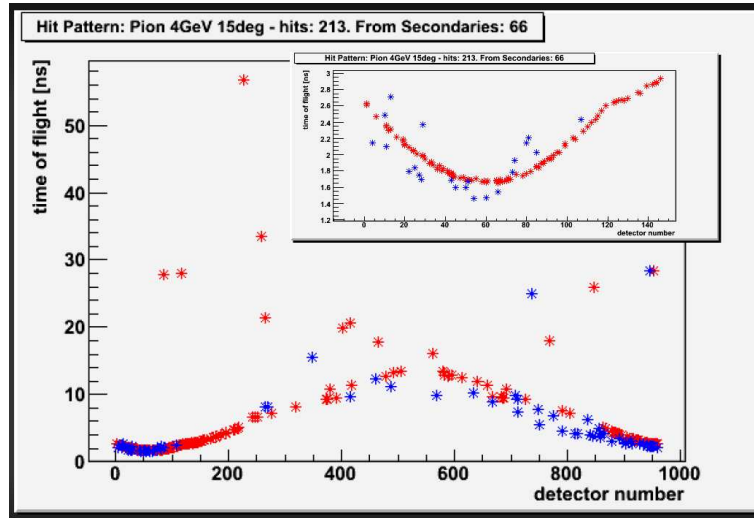
Figure 23: Hit pattern of photons in two-dimensional(ϕ,t) space. The Cherenkov photons coming from primary particle are marked red and from secondary particles , marked blue.

from MCP-PMT's, but also from neccesary electronics, their contribution was tested in the Lab using approximately the same chain as it awaited in final electronic design, see fig. 28. Currently, with available electronics, we achieve $\approx$ 40 ps resolution as it depicted in next fig.29, along with electronic scheme(fig.28) used in measurements.
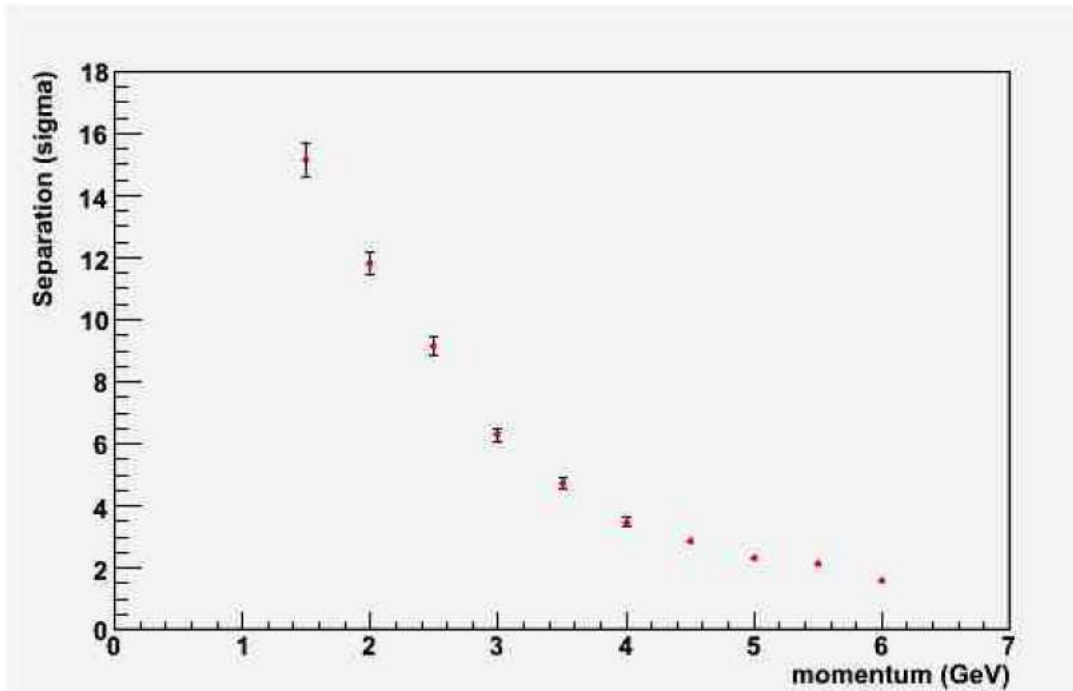
Figure 24: Separation power between Kaons and Pions from Slope fitting.
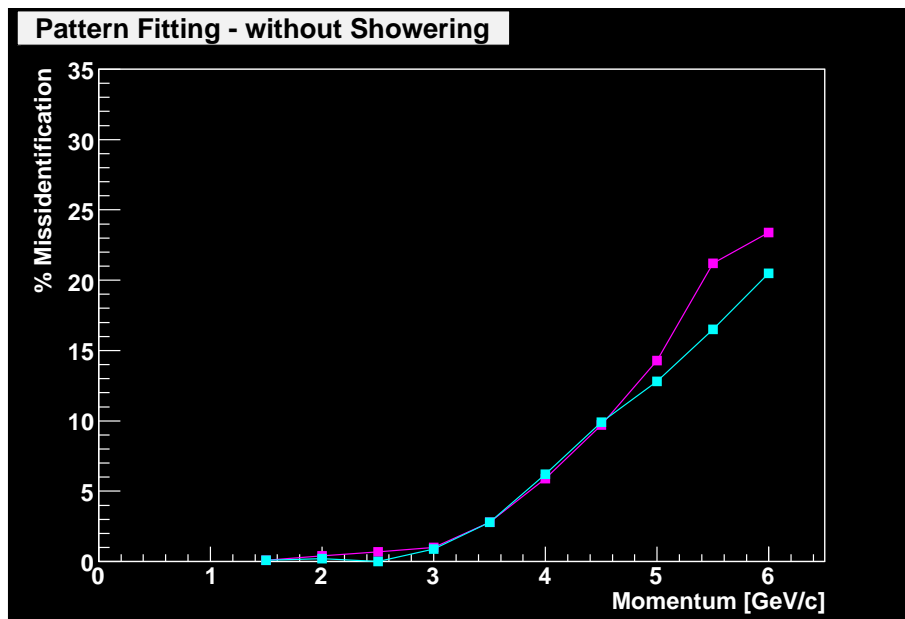
Figure 25: Misidentification between Kaons and Pions without inclusion of Cherenkov photons from secondaries into reconstruction.
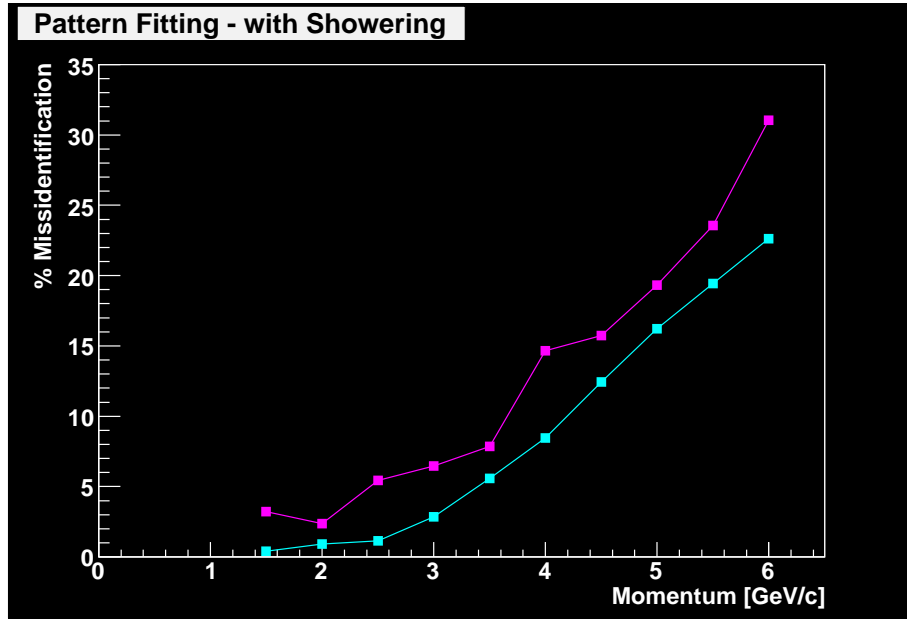
Figure 26: Misidentification between Kaons and Pions with inclusion of Cherenkov photons from secondaries into reconstruction.
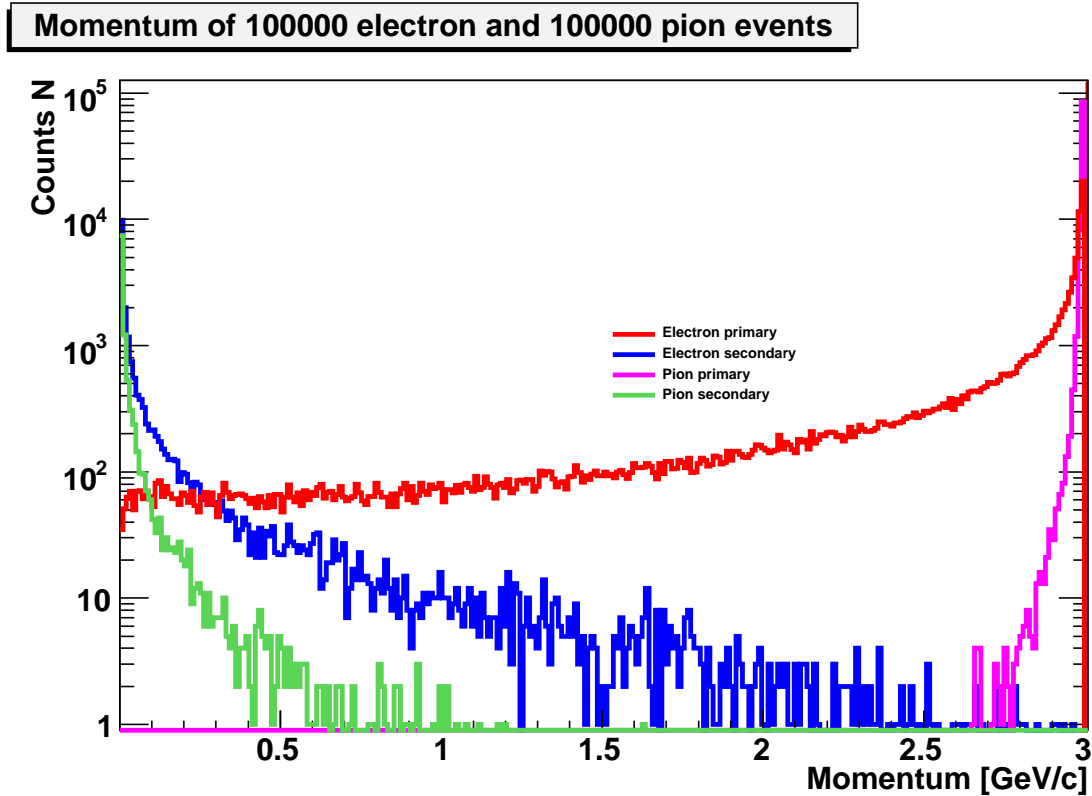
Figure 27: Energy spectra of primary and secondary charged particles inside 2cm thick glass after hitting it with electrons(pions) with 3.0 GeV energy. Unfortunately the energy of secondary particles are high enough to create Cherenkov photons and as they doesn't have the same direction as the primary particle, the photons created by them smear coordinate or timing pattern of primary particle, hence, making reconstruction difficult.
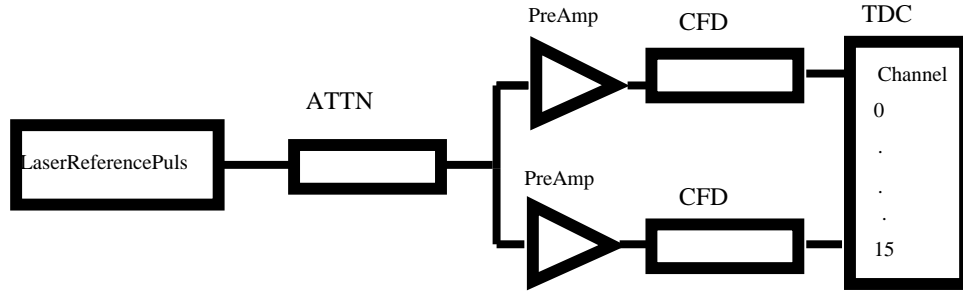
Figure 28: Used electronic scheme to measure contribution of each electronic module in time resolution. Note that TDC 1 channel is 25 ps.
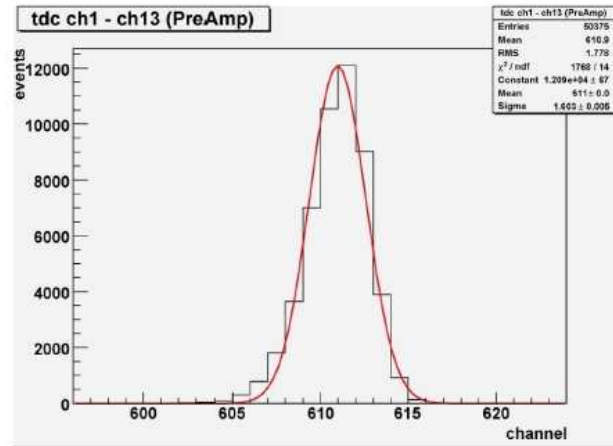
Figure 29: Achieved time resolution in TDC channels. Note that TDC 1 channel is 25 ps, and a Gaussian fit yields a Sigma of 1.4 channel.

3.5.3   Proximity RICH

As alternative approaches Proximity Imaging Solutions were considered.

- Liquid radiator proximity RICH using CsI GEMs: Proximity focusing RICH detectors use the most simplest imaging geometry. Their resolution depends on the optical quality and crucially on the ratio of radiator thickness to stand-off distance, the distance between the creation and detection of the photon. Using liquid or solid radiators yielding enough Cherenkov photons, the radiator can be kept rather slim, which in turn only require moderate stand-off distances on the order of 100 mm. The ALICE HMPID detector is build in this fashion using a C6F14 liquid radiator and CsI-photon cathodes in an MWPC. This requires a UV optic. It is proposed to use the same radiator technique and combine the third tracking station with a CsI coated GEM photon detector. The detector will be thicker along the beam direction than the DIRC detector previously described, but can be essentially moved to any position along the beam axis. The estimated performance and the ALICE/STAR test results show a significant decrease in performance compared to the DIRC solutions.

- Solid radiator proximity RICH using CsI GEMs: One of the main drawbacks of using the ALICE design is the use of C6F14. This radiator is rather sensitive to impurities and radiation damage requiring a purification system. Using a fused silica disc with a properly machined surface as radiator circumvents the problem while keeping the geometrical advantages of the design. Initial studies show a further reduction of performance mainly due to strong dispersive effects in the UV region.

- Aerogel proximity RICH using PMTs: The Belle endcap Cherenkov threshold counter will be replaced by a proximity imaging RICH counter using an Aerogel radiator and conventional BiAlkali based multi-pixel PMTs as photon detectors. Using a so-called focusing radiator scheme, prototypes show excellent performances. The main technological challenge for this detector is to realise a photon detection matrix in a strong magnetic field. Recent developments in the field of proximity focusing HAPDs seem to make such a detector realistic. The large number of pixels required should the detector be placed behind the EMC, but inside the cryostat merit a detailed look at the costs of such a design.

3.5.4 Forward RICH

Forward boost of the reaction products, being a characteristic feature of fixed–target experiments, calls for good particle detection and identification at small scattering angles.

Forward RICH is the solution proposed to perform PID for the ejectiles emitted at laboratory angles $\vartheta_X < 10°$ and $\vartheta_Y < 5°$. Physics, geometrical limitations and location of this detector impose the following requirements on the design of this detector:

- wide momentum range for hadron identification (up to $\sim$10 GeV/c),

- minimum material budget (in order not to deteriorate momentum and energy resolution of the downstream detectors),

- radiation hardness.

The first feature requires a careful choice of radiators. The current design proposes to build the Forward RICH as a dual radiator Cherenkov detector, with aerogel (PID for lower momenta) and perfluorhexane (PID for higher momenta). This option is used in other experiments, *e.g.* HERMES [13] and LHCb [19]. HERMES RICH design ranges of particle separation based on the signal from each of the radiators are shown in fig. 30. The limits were calculated assuming realistic photon resolution of $\sigma(\vartheta) = 7$ mrad, and the number of photons produced in the gas and the aerogel as 12 and 10, respectively. In the calculation of upper momentum limit of the separation, the demanded number of standard deviations between the two distributions $n_\sigma = 4.652$.
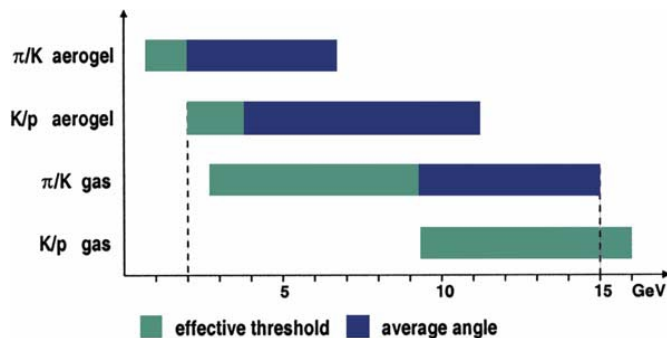
Figure 30: Momentum ranges for hadron separation in aerogel and perfluorhexane (C_4F_{10}). Between the dashed lines, the hadrons can be separated (figure from [13]). Light parts of the bars indicate the momentum regions, where the detector acts as a threshold Cherenkov.

The main disadvantage of this choice of radiators is a relatively high kaon threshold at 2.0 GeV/c. However, at lower momenta identification of ejectiles can be performed with the use of a TOF wall, as discussed in sec. 3.6.

The need to reduce the material budget to the necessary minimum favours mirror imaging. Using carbon–fibre based mirrors allows to move the photon detector outside of the acceptance of the Forward Spectrometer and thus reduce the overall detector thickness to ca. $8 - 11\%$ X_0. Forward RICH of $\overline{\text{P}}$ANDA will be much larger than the HERMES RICH and the space available for it is very limited. This requires a careful study of the optics. One of the currently considered options

includes four spherical mirrors and four detection planes, the other exploits the LHCb design (see fig. 31).
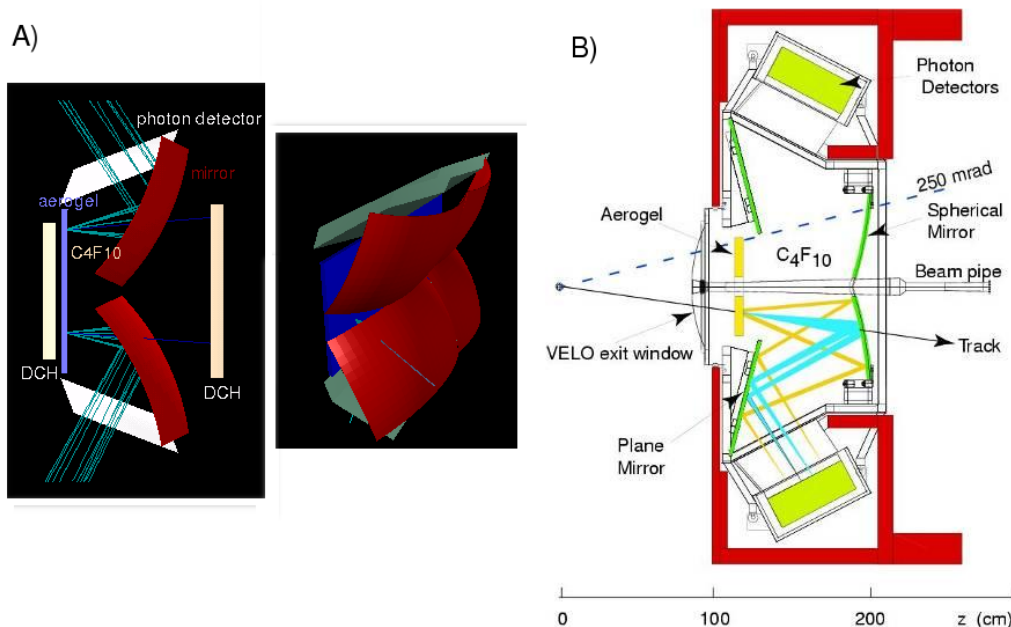
Figure 31: Two options of mirror imaging for the Forward RICH: A) direct, with 4 mirrors looking at different points B) exploiting additional plane mirrors which allow the use of spherical mirrors with a longer focal length.

The last requirement, radiation hardness, can be fulfiled chosing HPDs or MA-PMTs for photon detection. With the appropriate shielding, they have capability to operate in the fringe field of the dipole magnet. The granularity of the photon detectors can only be adjusted when the design of the RICH geometry is finalised.

3.6 Forward ToF

Typical momentum spectra of the charged hadrons produced within the acceptance of the forward spectrometer FS (± 10 deg. in horizontal plane and ± 5 deg. in vertical plane) for primary beam momentum of 15 GeV/c are shown in Fig.3.6. The spectra are calculated in the Pandaroot framework using Dual Parton Model (DPM) Monte Carlo generator. The hadrons with momentum below 4-5 GeV/c are assumed to be identified with the help of time of flight (TOF) technique. Identification of hadrons with higher momenta requires a forward RICH. This is in particular important for identification of anti-hyperons. For example, practically all anti-lambda hyperons produced in the $\bar{p}p \to \bar{\Lambda}X$ reactions (including two-body reaction $X = \Lambda$) are boosted forward such that the anti-protons from the $\bar{\Lambda}$ decay are detected mostly by the FS. In general, a combination of the TOF and RICH looks as the best one for the PID in the whole momentum range of the produced forward hadrons. The combination of TOF and RICH detectors is successfully used in the HERMES experiment [13]. The HERMES RICH thresholds are 2 GeV/c for pions and 4 GeV/c for protons, respectively. Here we focus on PID performed using TOF technique in the forward part of the PANDA detector.
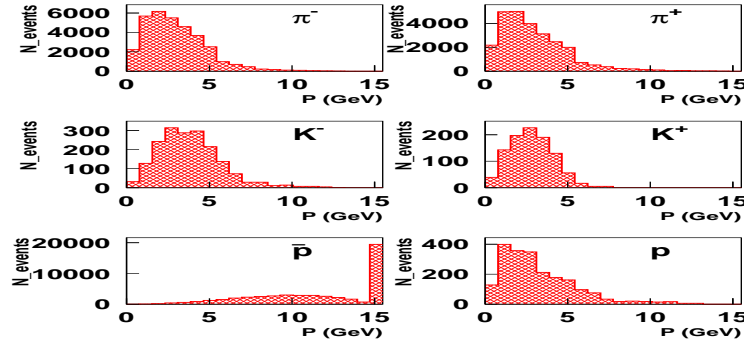
Figure 32: *Momentum spectra of charged hadrons emitted within the FS angular acceptance in $\bar{p}p$ collisions at 15 GeV/c.*

TOF detector performance. High-resolution TOF detectors are widely used in many experimental setups [14]. The PANDA forward detector consists of two parts: the forward TOF wall and two side TOF walls placed inside the FS dipole gap [**?**]. The side detectors are designed for registration of low momentum particles, not being detected by the forward wall as they are bent inside the FS dipole by the magnetic field to the left or to the right towards the magnet yoke. Unfortunately, the exact configuration of the FS dipole magnetic field is not yet available which makes it difficult to simulate tracking through the dipole. According to our estimations, at the primary beam momentum of 15 GeV/c a particle with momentum below 0.8-1.2 GeV/c (depending on scattering angle) is bent to one of the side detectors. Each side detector consists

of 5 vertical scintillation strips with dimensions $100 * 10 * 1.5$ cm^3. It is not decided yet whether a magnetic field protected PMT or SiPM is to be used for light collection in the side detectors. The forward TOF wall is located at 7.5 m downstream the interaction point. Proceeding from the FS angular acceptance and taking into account deviations in the FS dipole of the particles with momenta higher than $\sim \frac{1}{15}$ of the $\bar{p}$ beam momentum, the dimensions of the forward TOF wall are taken to be 1.4 m in vertical and 5.6 m in horizontal direction. It consists of 66 scintillation counters. A scintillation counter consists of a vertical strip made of plastic scintillator BC408 of 1.5 cm thickness (material budget $\frac{X}{X_0} \approx 3.5\%$). The strip is coupled at the both edges via light-guides to the PMT Hamamatsu R2083 or R4998. The central part of the wall which is close to the beam pipe consists of 20 scintillation counters with $140 * 5$ cm^2 strips, and left and right outer parts consist of 46 scintillation counters with $140 * 10$ cm^2 strips. Granularity indicated here for the forward TOF and in particular for the side TOF detectors is optional. It is subject to careful MC simulations and experimental investigations of the TOF resolution. The light-pulse amplitude and shape at each end of the strip depends on a particle hit position which is to be specified in off-line analysis using tracking information. The (off-line) time resolution of a TOF wall-scintillation counter is estimated to be 50-60 ps. It is not yet decided which equipment is to be used as a "start" pulse for the time of flight. If no start counter is available a possibility to measure time correlation between two stop counters is considered provided at least two particles from an event is detected by the TOF wall [15]. In all the cases the time resolution of both pulses (start and stop or two stop ones) not worse than 50-70 ps is needed. The overall TOF time resolution then is expected to be on the level of $\sim$100 ps.

MC simulations of the detector capabilities. The MC-simulations presented in this section have been performed using DPM generator. A simple cut on the FS acceptance has been applied. No magnetic field has been included in the simulations such that a track has been approximated with a straight line coming out of the interaction point. This is a very coarse approximation for low momentum particles, which however underestimates the TOF length and, respectively, overestimate the value of TOF resolution. The hadron rates calculated in this approach for 4π acceptance and for the FS acceptance at luminosity $2 \cdot 10^{32} \text{cm}^{-2}\text{s}^{-1}$ are given in Table 3 and Table 4, respectively.

Table 3: 4π rates for various beam momentum and particles.

Beam momentum (GeV/c)	σ_{tot} (mbarn)	4π rates (1/sec)	$\pi\pm$ (1/sec)	$K\pm$ (1/sec)	Proton (1/sec)	P_{bar} (1/sec)
2	90	$1.8 * 10^7$	$7.17 * 10^6$	$6.47 * 10^4$	$2.23 * 10^6$	$2.25 * 10^6$
5	64.8	$1.3 * 10^7$	$5.4 * 10^6$	$6 * 10^4$	$1.37 * 10^6$	$1.36 * 10^6$
15	50.8	$1 * 10^7$	$4.15 * 10^6$	$1.48 * 10^5$	$9.16 * 10^5$	$9.18 * 10^5$

Distributions of the particle rates over the TOF detector are not uniform and momentum dependent. The forward yields ($\frac{dN}{dcos\theta}$, where θ is the scattering angle) are peaked at $\theta = 0$ with various slopes. As seen from Table 4 the highest rate is expected for anti-protons, mostly for elastically scattered anti-protons (see the peak of elastic $\bar{p}$ scattering in Fig. 3.6). As the cross section for elastic scattering is a very steep function of θ practically all anti-protons are emitted within the FS acceptance. In Fig. 3.6 anti-proton hit distributions for $\bar{p}$ momentum in the range 12 to 15 GeV/c are shown. As seen from the count rate per a scintillation count (lower panel) this rates are low

Table 4: Forward Spectrometer rates for various beam momentum and particles.

| Beam momentum | Forward rates | $\pi\pm$ | $K\pm$ | P | $\bar{P}$ |
(GeV/c)	(1/sec)	(1/sec)	(1/sec)	(1/sec)	(1/sec)
2	$1.8*10^6$	$3.9*10^5$	$2*10^3$	$1.2*10^4$	$1.07*10^6$
5	$2.17*10^6$	$6*10^5$	$7.8*10^3$	$3.8*10^4$	$9.5*10^5$
15	$2.93*10^6$	$9.56*10^5$	$4.7*10^4$	$3.2*10^4$	$8.2*10^5$
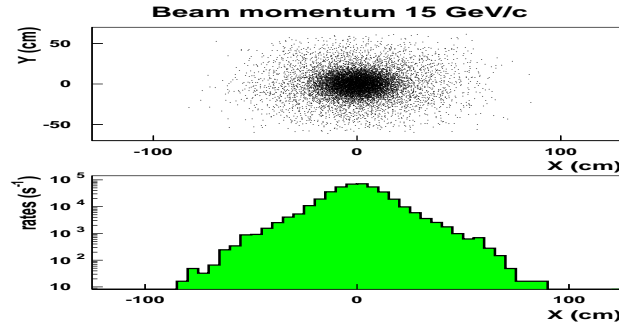
Figure 33: *Anti-proton hit distributions for $\bar{p}$ momentum in the range 12 to 15 GeV/c (mostly elastically scattered anti-protons). Upper panel: areal distribution over XY-plane at the position of the forward TOF wall (X=Y=0 are primary beam coordinates), lower panel: count rate per a scintillation counter. Note that the bin width is taken equal to the central strip width (5 cm).*

enough even in the central part of the detector and does not restrict its operational capabilities. A momentum p and charge sign of a forward emitted particle is measured by tracking through the dipole magnet of the FS with momentum resolution typically better than 1%.

For a detected particle its mass m can be expressed as

$$m = p\sqrt{\frac{t^2}{t_c{}^2} - 1}. \tag{4}$$

Here $t_c = L/c$ where c is speed of light, L is the TOF length, i.e. the length of the particle track counted from the interaction point to a "stop" counter; t is the measured time of flight, $\frac{t}{t_c} = \frac{1}{v}$ where v is the particle velocity ($c = 1$). A fractional uncertainty in determination of the particle mass is

$$\frac{\delta m}{m} = \sqrt{(\frac{\delta p}{p})^2 + \gamma^4(\frac{\delta t}{t})^2}, \tag{5}$$

where $\gamma = \frac{1}{\sqrt{1-v^2}}$. The TOF wall is positioned at 7.5 m from the target which corresponds to
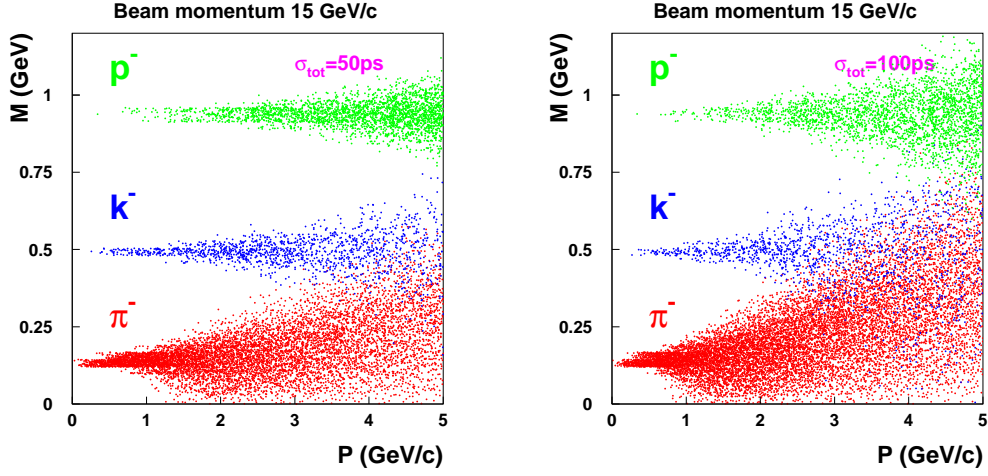
Figure 34: *Reconstructed masses for hadrons of a negative charge.*

$t_c^{min} = 25$ ps. Due to relativistic factor γ^4 the TOF resolution of ~ 100 ps dominates the mass smearing for relativistic particles while the momentum resolution of 1% has just a little effect. An additional δm may come form uncertainty in L (or t_c) due to tracking in the magnetic field of the FS dipole. It is estimated to be on the level of a few ps and ignored. An example of the forward TOF wall capability to identify hadrons is demonstrated in Fig. 34 where the hadron masses calculated with the help of Eq.4 are plotted versus the hadron momentum.

Separation power. PID quality of the TOF wall detector is quantified using a value of Separation Power SP defined in section 4.1 of this document. In these calculations the binning has been done in the hadron momentum in the range 0.5 to 4 GeV/c (7 bins). In each bin the hadron mass distribution is approximated with a gaussian. The central (mass) position has been fixed according to PDG while the dispersion σ_{mass} is found by fit to the experimental histogram. Separation powers for pairs of particles π/K and K/P calculated in such a way are presented in Fig.35.
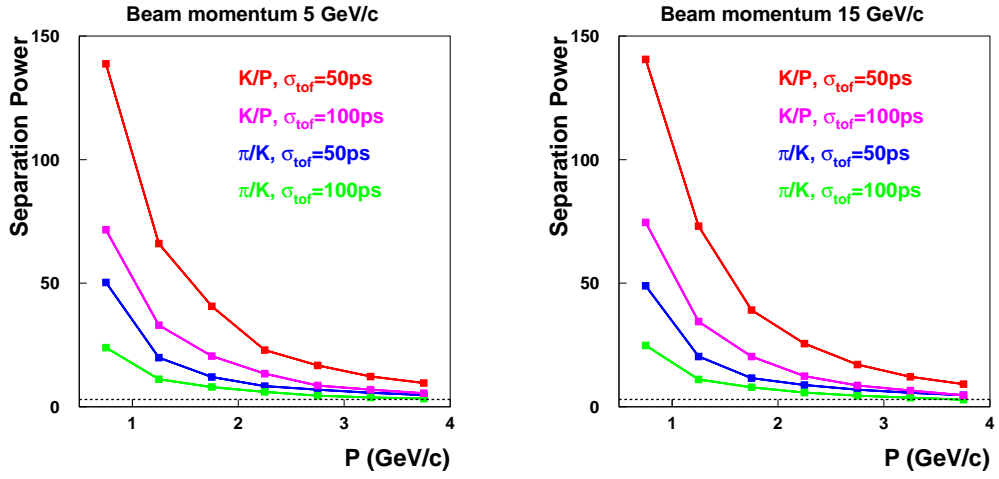
Figure 35: *Separation power vs. particle momentum, dashed line - 3σ separation*

3.7   Forward Calorimeter

The forward calorimeter will consist of two parts, the upstream being electromagnetic, the downstream serving as a muon filter and hadron calorimeter.

3.7.1   Electromagnetic calorimeter

For the electromagnetic calorimeter, for its large size and high energies of impinging particles, the most suitable seems the Shaslyk technique. It has been positively proved to work well in other experiments, *e.g.* E865 [17] and KOPIO [18]. In the latter the achieved energy resolution amounted to $4\%/\sqrt{E}$. Tha calorimeter is built in a form of a lead-scintillator sandwiches that are read out via WLS fibres passing through them. The detector is located at a distance of ca. 7 m downstream the target. Thus, in order to cover the area limited by $\vartheta_X < 10°$ and $\vartheta_Y < 5°$, it should consist of 13×27 modules of rectangular cross-section of the size of 11 cm. The given size is a reasonable compromise between the performance on one hand side (lower size leads to better position resolution), and the cost and complexity on the other. Below the major features of the planned electromagnetic calorimeter are listed:

- 400 layers of Pb ad scintillator (ca. 20 X_0),

- $d(\text{Pb}) = 0.275$ mm (thickness of a single lead layer),

- $d(\text{Scint.}) = 1.5$ mm (thickness of a single scintillator layer),

- number of fibres per module: 72 or 144,

- readout: PMT

- design resolution:$4\%/\sqrt{E}$.

Several test setups with modules of different sizes have been built in IHEP, Protvino, and now they a subject of ongoing beam tests. Fig. 36 presents the 3×3 setup, including the layout of the unpacked modules. The results of the tests are very encouraging. Based on the beam tests
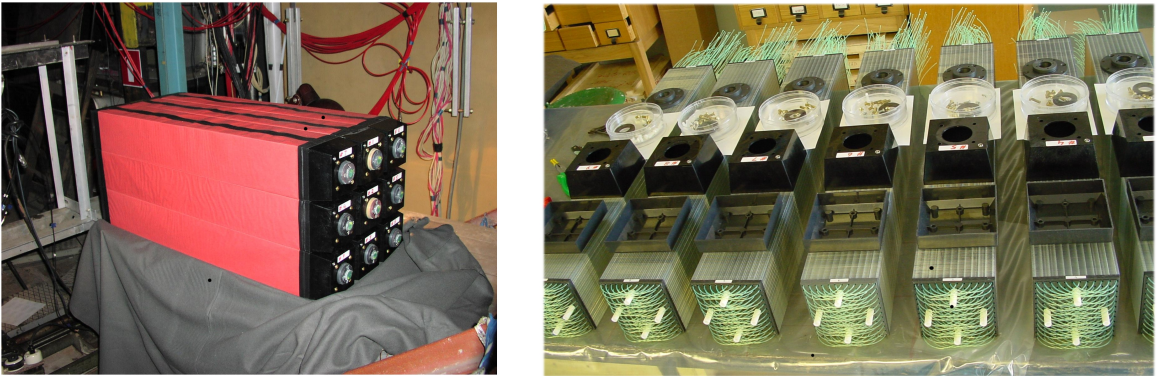
Figure 36: Left: a test setup of 9 modules, right: unpacked shashlyk modules.

performed in 2007, the energy resolution was parametrised as follows:

$$\frac{\sigma_E}{E} = \frac{a}{E} \oplus \frac{b}{\sqrt{E}} \oplus c \quad [\%]$$

where $a = 3.5 \pm 0.3$, $b = 2.8 \pm 02$, $c = 1.3 \pm 0.04$.

A series of simulations, based on the so-called *old code*, have been done in order to investigate performance of calorimeter of this type for electron/pion separation. Different momenta (1 GeV/c and 5 GeV/c) of electrons and pions as well as different lateral dimensions of the modules were simulated. Detector response and cuts imposed in order to select electrons of 5 GeV/c momentum in the 110×110 mm^2 modules are shown as an example of the procedure 37. A particle was identified as an electron if the associated signal was in the three cuts presented in fig. 37 as dashed lines. Results of the simulations are collected in the tables 6 and 5.

Module size [mm^2]	e^- identified [%]	π^- identified as e^- [%]
30×30	84.6	0.2
55×55	93.3	0.4
110×110	97.4	0.8

Table 5: Results of PID using the shashlyk calorimeter for 5 GeV/c electrons.

Module size [mm^2]	e^- identified [%]	π^- identified as e^- [%]
55×55	96.2	4.7
110×110	98.1	8.7

Table 6: Results of PID using the shashlyk calorimeter for 1 GeV/c electrons.

3.7.2   Hadron calorimeter

The hadron calorimeter will be placed around 8 m dowstream the target and extends on 440 cm horizontally and 180 cm vertically. Its task is to measure energies of neutrons and antineutrons, large numbers of which bombard the region of acceptance covered by the Forward Spectrometer. Apart from that, it will be useful to determine energies of other neutral hadrons (*e.g.* K_L) or give fast signal for triggering on reactions with forward scattered hadrons. Last but not least, the detector will be used to discriminate between charged hadrons and muons. This will be achieved by combining the energy loss information with the information obtained from the muon counters.

Of the two design options suitable for the $\overline{\text{P}}$ANDA experiment [1], the muon filter option sems to be the better one. In this design sections of steel–scintillator sandwich are interlaced with gas detectors, which allows much better muon identification than a passive filter made of an absorder block. The pid performance of an active filter is by an order of magnitude better than for a passive one, the measure being misidentification probability.

The hadron part (muon filter) to be continued ??...

Figure 37: Detector response to single pion (red) and single electron (black) events is shown in terms of number of reconstructed clusters (top), number of fired modules (middle) and reconstructed energy (bottom). Cuts shown with the dashed lines were used to select electrons.

3.8 Muon Counter

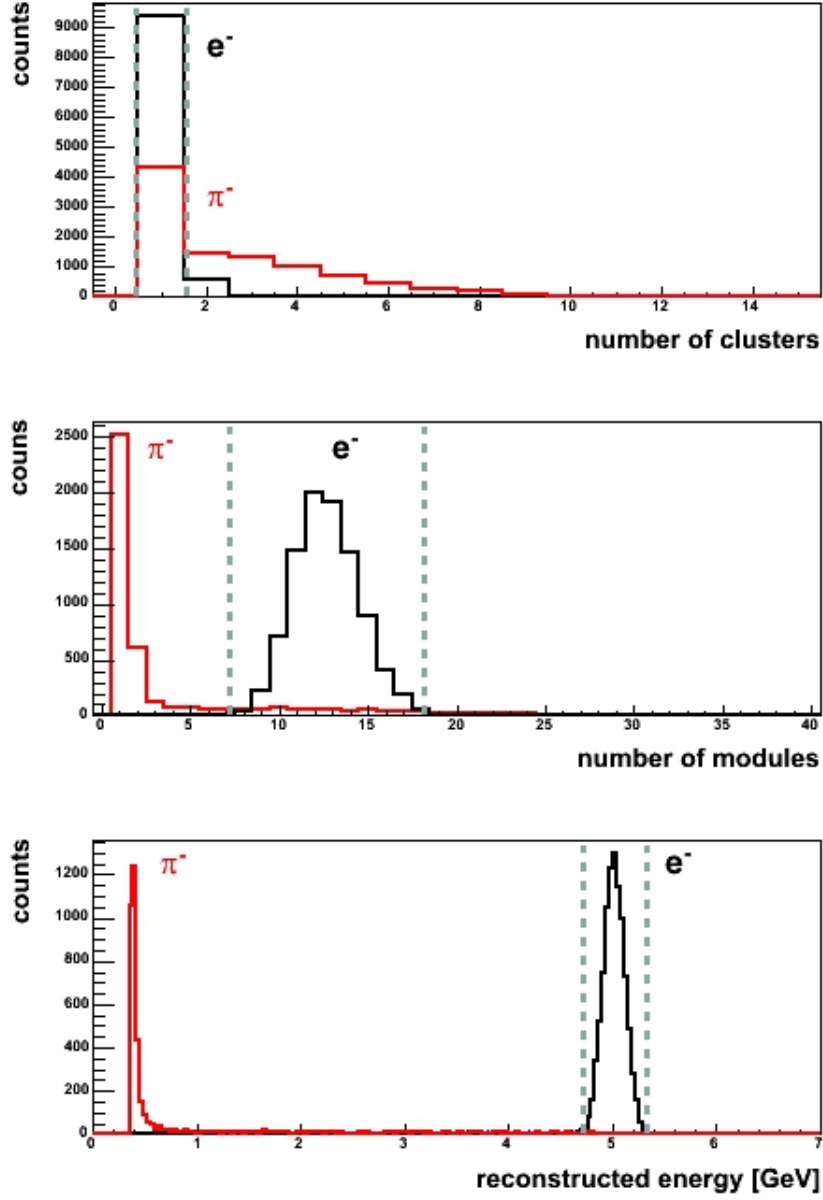The main purpose of the PANDA muon system is to achieve the highest efficiency in identification of muons in the medium-high energy range. Muons are present in the final state of many annihilation channels. Among them the physics program is mostly concentrated on dimuon production from Drell Yan at the maximum HESR momentum of 14.5 GeV/c or J/ψ formation and decay in nuclear matter at 4.1 GeV/c momentum. In addition the study of rare decay of charmed particles could require a single muon identification. The most severe PID requirements to the muon system are set by the DY dimuon production, that has been selected as benchmark channel. Looser identification requirements are set by the J/ψ production channels, because of the strong kinematics constraint on the dimuon mass.

In general the interesting processes having muons in the final state have small cross section compared with the background, e.g. the DY channel features a very low cross section ($\approx 1nb$) and the unfavourable signal-to-noise ratio ($\approx 10^{-6}$). As a consequence the muon system must provide the maximum acceptance and efficiency. In the dimuon channels the simultaneous identification of a slow and of a fast muon is needed, with a strong correlation angle-momentum.

Muon counters are foreseen both in the Target barrel part and endcap. In the Forward spectrometer the muon counters and filters will act as hadronic calorimeter. The azimuthal angle covered by the muon system ranges from 0° to 120° with a 2π polar angle coverage. With respect to the Letter of Intent the muon system has retained the original idea to use the solenoid yoke as muon filter. However the concept design has changed following the results of a preliminary acceptance study and the iron segmentation has been considered for the system optimization.

The momentum range of the DY muons reaching the barrel extends up to few GeV/c. The lower end of the range is fixed by the energy losses and the magnetic bending in the inner detectors (500 MeV/c).

The DY muons crossing the forward endcap show an energy range going from 1 to 3 GeV, with an average energy loss of 250 MeV before to enter the muon counters. The energy of the muons travelling through the Forward spectrometer can be greater than 10 GeV. *here relevant plots*

As a consequence slow muons, mainly produced in transverse direction cannot reach the muon system and must be identified by the inner detector. Medium and high energy muons are identified by the muon system only if they are positively detected by the muon detectors and properly match a charged primary track detected by the central tracker. The muon detector output that can be considered for identification purposes is the hit multiplicity in a selected region and, for isolated tracks, a direction and, where possible, a momentum measurement. Range measurement was also suggested as an effective tool for μ/π separation and the arrangement presently under simulation is conceived for this purpose, see fig. 38 and fig. 39.

The following plots show the behaviour of some parameters useful for the muon identification.

The background coming from primary hadrons (mostly pions) could be rejected by the evaluation of the number of planes in the muon system crossed by the charged particle (see fig. for muon and pion of equal energy).

The contamination coming from secondary muons produced by the pion decay could be reduced by considering the angular correlation between the track extrapolated from the vertex and the track segment measured by the muon detectors. In this case (see fig. 40) the measurement of the track momentum by the muon detectors could help.

here(relevant plots
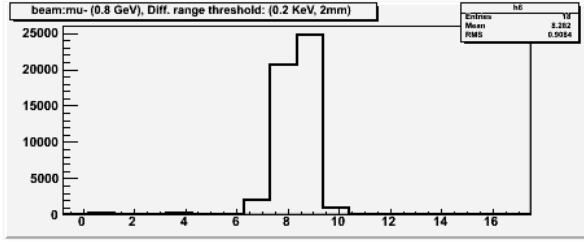
Figure 38: *Range measured as number of crossed planes for a muon with 0.8 GeV energy.*
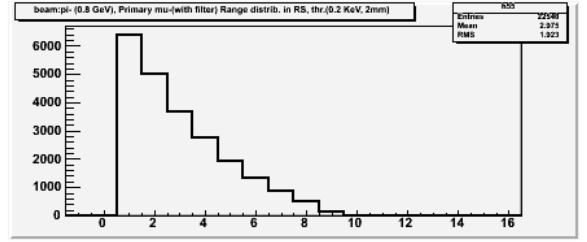
Figure 39: *Range measured as number of crossed planes for a pion with 0.8 GeV energy.*
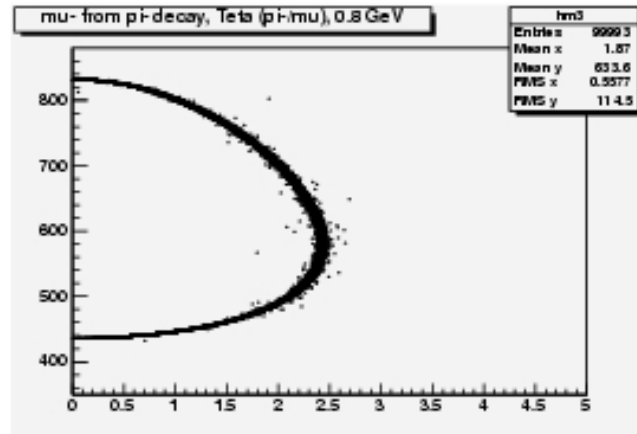
Figure 40: *Muon from decaying pion with 0.8 GeV energy: energy vs decay angle in the Lab system.*

3.8.1   Muon system overview

The parameters considered in the choice of the muon detectors are the spatial and time resolution, to allow independent reconstruction of the track segment direction, the simplicity and flexibility of the design, since the area to be covered is large and divided in different shapes, the robustness the reliability, also in terms of ageing and finally the cost. the MDT have been proven to be a mature and widely used technique that join a very high detection efficiency ($\approx 95\%$) to a great semplicity of production, construction and operation. Following the proposal of thye JINR-Dubna group an eight-cell module of MDT is constituted by a metallic cathode extruded with a comb-like profile and covered by a stainless steel cover. The signal wires pitch is 10 mm, the thickness of the profile is ≥ 0.45 mm and gives the main contribution to the inefficiency of the counter.

here the MDT cross section and the table of the performances

The MDT are one-coordinate detectors and minimum two layers must be installed to get a track space point. An R&D project is going on at JINR Laboratories aiming to use MDT as two-coordinate detector. For this purpose the stainless steel cover should be removed and substituted by a plastic support for strips or pads. In this case the second coordinate is obtainted by reading out the induced signal.

The MDT are operated in proportional mode. Both the Yes/No readout or the wires and drift
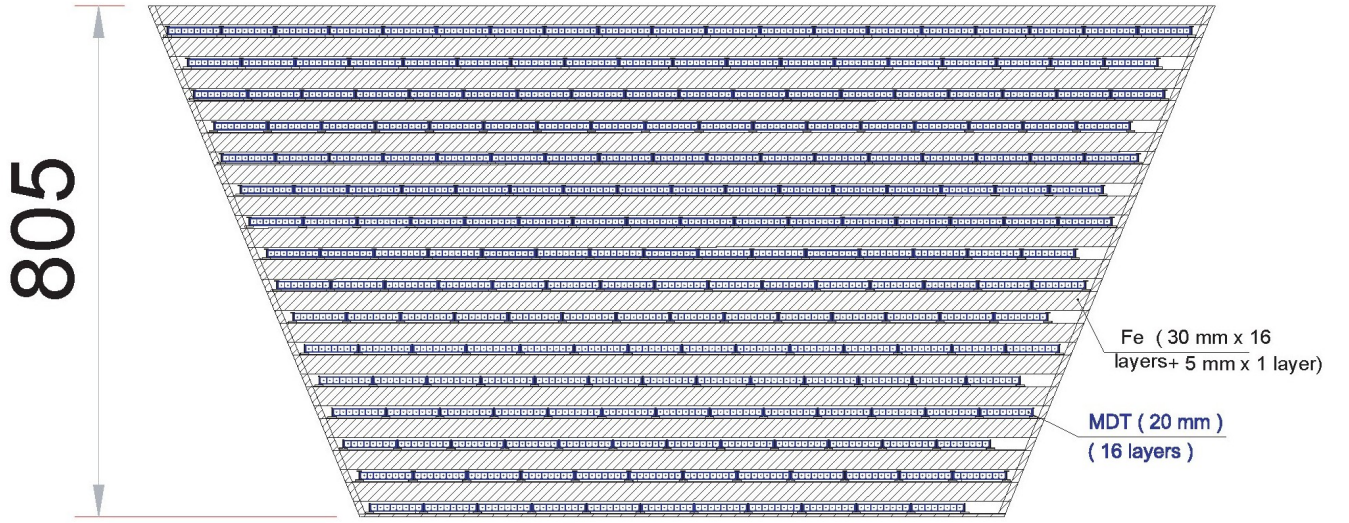
Figure 41: *Cross section of the Muon range system in the Target Spectrometer.*

time measurement are considered for the PANDA operation. The best spatial resolution is obtained in drift mode operation, corresponding to 0.5-0.8 mm r.m.s.

The detector coverage presently considered corresponds to a full coverage of the Target Spectrometer in the trasverse direction with respect to the beam axis (Barrel) and in the forward direction (Forward Endcap), using the yoke of the solenoid as a muon filter. One of the eight parts of the barrel will be only partially covered by muon counters to allow the insertion and the operation of the target and its services. In the Forward Spectrometer (angular coverage from $5° − 10°$ to $0°$ thehadronic calorimeter could be equipped with muon counters.

4 Tools

In this section the TAG work is described. To evaluate the performance of the detectors the PID TAG defined the "Separation Power" as the right tool (see section 4.1. With the help "Phase Space Plots" (section 4.2) the angular coverage and the coresponding particle momenta could be determined. The "Fast Simulation" (section 4.3) was used to map the separation power over the full angular and momentum range. In a second step important reactions and their relevant background channels were simulated. Thus the regions where a good separation power is needed could be identified and checked whether the detector performance is sufficient there.

4.1   Separation Power

This document completely deals with the quality of the particle identification of the projected PANDA detector. Thus the major issue upon which decisions can be made is a proper definition of classification quality or performance.

The according concept chosen for that purpose called 'Separation Power' bases on the assumption that the particular observables of objects of different classes exhibit more or less gaussian distributions.

Consider the situation illustrated in fig. 42.
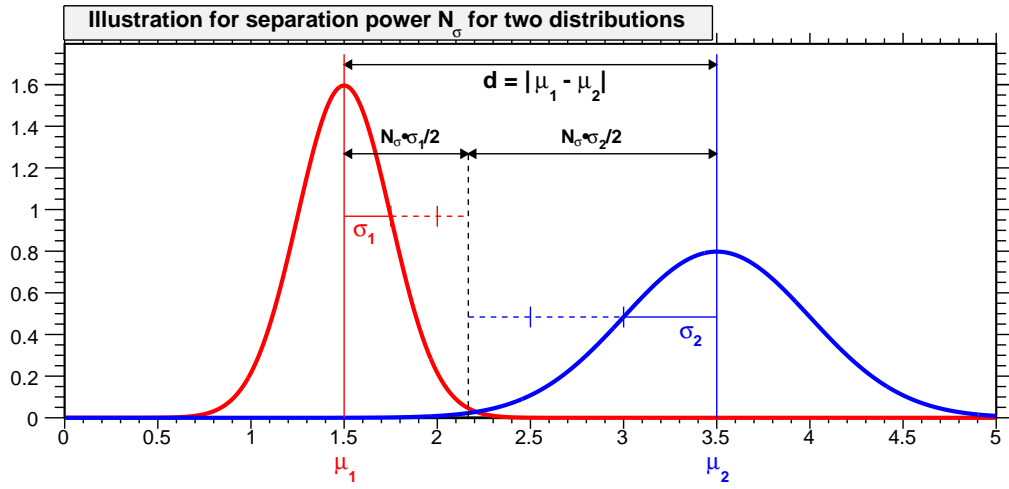
Figure 42: Illustration for the definition of separation power.

There are plotted two gaussian distributions $G_1(x) \equiv G(x; \mu_1, \sigma_1)$ and $G_2(x) \equiv G(x; \mu_2, \sigma_2)$ with mean values $\mu_1 = 1.5$ and $\mu_2 = 3.5$ and standard deviations $\sigma_1 = 0.25$ and $\sigma_2 = 0.5$. This could be e. g. the probability density distributions of the dE/dx measurements for two particle species in a small momentum range. Obviously the distributions are separable quite reasonable, but what is the measure for the separation potential?

A proper definition would be to define a particular classificator, e.g. every particle with property $x_0 < 2$ is considered as member of class 1 (red). Then one can determine two quantities which are of relevance for the qualtiy of classification. The first one ist the efficiency, which is part of the distribution 1 (or a random sample of measurements following this distribution) which is identified correctly analytically corresponding to the integral

$$\epsilon = \int_{-\infty}^{x_0} G_1(x)\, dx \tag{6}$$

for a normalized Gaussian. The second quantity is the misidentification level given by the integral

$$\text{mis-id} = \int_{-\infty}^{x_0} G_2(x)\, dx \tag{7}$$

which is part of the distribution 2 in the same region thus identified incorrectly as being of class

1. These two values would define clearly the performance of the classificator[3]. But this solution cannot be applied in case when one does not want to define a particular selector. It rather has to be defined a measure for the prospective performance of a possible selector.

Exactly this is the aim of the separation power N_σ which relates the distance of the mean values $d = |\mu_1 - \mu_2|$ of the two distributions to their standard deviations σ_1 and σ_2. The usual unit of N_σ is 'number of gaussian sigmas of the separation potential', which is supposed to relate the number with gaussian integral values.

There are actually a lot of different definitions for that quantity on the market but it has been found an agreement within the PID TAG on the following definition:

$$N_\sigma = \frac{|m_1 - m_2|}{\sigma_\beta} = \frac{|m_1 - m_2|}{(\sigma_1/2 + \sigma_2/2)} \tag{8}$$

This relationship is illustrated in fig. 42. The black dashed line marks the position x_0 between the two distributions, for which the differences to each mean value $|m_1 - x_0| = N_\sigma \cdot \sigma_1/2$ and $|m_2 - x_0| = N_\sigma \cdot \sigma_2/2$ are the same in terms of σ's.

This means a separation of e. g. $N_\sigma = 4\sigma$ corresponds to a gaussian integral

$$I = \int_{-\infty}^{\mu+4\sigma/2} G(x; \mu, \sigma)\, dx = 0.9772 \tag{9}$$

which shall express an efficiency around $\epsilon \approx 97.7\%$ or a mis-ID level around mis$=100\% - 97.7\% \approx 2.3\%$ or both. This integration up to half the number of sigmas $N_\sigma/2$ seems a bit contra intuitive but is common notion and therefore has kept for the considerations in this document. Another feature of this definition is that it is symmetric for both classes or distributions, even with different σ's. Furthermore for the particular case of normalized gaussian distributions and a selector requiring $x < x_0$ for classifying class 1 objects in the upper example, the efficiency ϵ and purity π for this selection have the same value, since

$$\epsilon = \frac{\int_{-\infty}^{x_0} G_1(x)\, dx}{\int_{-\infty}^{+\infty} G_1(x)\, dx} = \frac{\int_{-\infty}^{x_0} G_1(x)\, dx}{1} = \frac{\int_{-\infty}^{x_0} G_1(x)\, dx}{\int_{-\infty}^{x_0} G_1(x)\, dx + \int_{x_0}^{+\infty} G_1(x)\, dx} \tag{10}$$

$$= \frac{\int_{-\infty}^{x_0} G_1(x)\, dx}{\int_{-\infty}^{x_0} G_1(x)\, dx + \int_{-\infty}^{x_0} G_2(x)\, dx} = \frac{\int_{-\infty}^{x_0} G_1(x)\, dx}{\int_{-\infty}^{x_0} G_1(x) + G_2(x)\, dx} = \pi \tag{11}$$

Tab. 7 lists on the left hand side the mis-id levels $1 - \int G(x) dx$ with 1-sided and 2-sided gaussian integrals for different values of N_σ, on the right hand side the corresponding values of the separation power for given levels of mis-id according to the upper definition. It shall be emphasized again that for given values N_σ the integration is only performed up to $N_\sigma/2$, therefore the mis-id levels might seem surprisingly high for given number of σ's separation.

Taking into account that quantities in reality never have gaussian shape the values σ in fact are not necessarily gaussian sigmas but calculated as the root-mean-square (which actually is the standard deviation)

$$\sigma_{\mathrm{rms}} = \sqrt{\sum_i (x_i - \mu)^2} \tag{12}$$

---

[3]For Bayes' classification a flux correction would have to be taken into account additionally. This requires of course knowledge about a posteriori probabilities of particle fluxes which not necessarily is available since significantly dependent on the given trigger and reaction type.

what in case of gaussian distribution would be indeed identical with the gaussian σ from above. For the given example in fig. 42 the definition (8) computes to

$$N_{\sigma,1} = \frac{2}{0.25/2 + 0.5/2}\,\sigma = \frac{2}{0.375}\,\sigma = 5.333\,\sigma \quad .$$

Another issue with directly is connected with the upper definition is the question how to define the combined separation $N_{\sigma,\text{tot}}$ e.g. for values $N_{\sigma,i}$ achieved by various detector components to express the overall performance. The agreement of the PID-TAG concerning this was to consider the quadratic sum

$$N_{\sigma,\text{tot}} := \left(\sum_i N_{\sigma,i}^2\right)^{1/2} \tag{13}$$

as a good measure. In order to evaluate the goodness of that expression it first of all is necessary to make aware what meaning the value N_σ has in terms of probablity. When considering something similar to equation (9) as a appropriate measure, namely the integral of a Gaussian from $-N_\sigma/2$ to $+N_\sigma/2$ the expression for the corresponding probability of mis-identification is given by

$$P_{\text{mis}}(N_\sigma) = 1 - \int_{-N_\sigma/2}^{+N_\sigma/2} G(x; \mu = 0, \sigma = 1)\,dx \tag{14}$$

which directly defines the mis-identification probability for n statistically independent separation capabilities as the product

$$P_{\text{mis,tot}} = P_{\text{mis}}(N_{\sigma,1}) \times \cdots \times P_{\text{mis}}(N_{\sigma,n}) \tag{15}$$

in addition. Hence equation (14) implicitly specifies $N_{\sigma,\text{tot}}$ as that value where the intergral yields exactly $P_{\text{mis,tot}}$. This procedure has been pursued for two values $N_{\sigma,1}$ and $N_{\sigma,2}$ as presented in fig. 43. In (a) the combined separation power is shown as 2-dimensional function of the two input values, (b) presents the difference

$$\Delta = \left| N_{\sigma,\text{tot}} - \sqrt{N_{\sigma,1}^2 + N_{\sigma,2}^2} \right| \tag{16}$$

of the resulting value and equation (13), which obviously reasonably reproduces the correct value with a maximum deviation of about 0.5σ in the range of single values up to $N_\sigma = 6$.

4.1.1   Parametrization of the Electromagentic Calorimeter

Although not implemented in the Fast Simulation, a parametrization of part of the response of the EMC has been persued for the estimation of overall PID quality. It is based on fully simulated data but only information about electron-pion-separation was taken into account up to now. Fig. 44 (a) shows the distributions of the parametrized ratio of the calibrated cluster energy in the electromagnetic calorimeter and the reconstructed track momentum E_{clus}/p for simulated electrons (green) and pions (black). The source for modelling the parametrizations can be found in the PANDA Physics Book [?]. It is clearly visible that above momenta of approximately 500 MeV this quantity is a powerful tool to separate electrons from pions, demonstrated in fig.44 (b), where the separation power has been determined dependend of the track momentum p by the
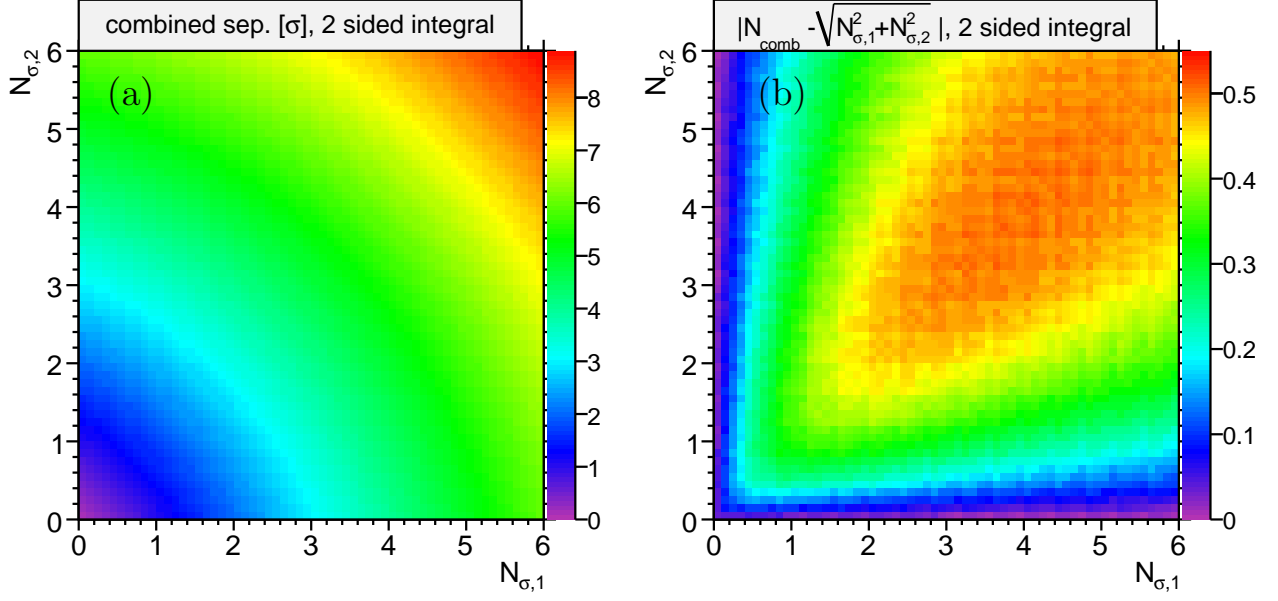
Figure 43: (a) Graphical representation of the combined separation power $N_{\sigma,\text{tot}}$ of two values $N_{\sigma,1}$ and $N_{\sigma,2}$, (b) the corresponding difference $\left| N_{\sigma,\text{tot}} - \sqrt{N_{\sigma,1}^2 + N_{\sigma,2}^2} \right|$.

N_σ	mis-id (1s) [%]	mis-id (2s) [%]	mis-id [%]	N_σ (1s)	N_σ (2s)
1.0	30.854	61.708	10.000	2.6	3.3
2.0	15.769	31.538	5.000	3.3	3.9
3.0	6.681	13.361	1.000	4.6	5.1
4.0	2.254	4.507	0.500	5.1	5.6
5.0	0.621	1.242	0.100	6.2	6.6
6.0	0.133	0.266	0.050	6.6	7.0
7.0	0.023	0.047	0.010	7.4	7.8
8.0	0.003	0.006	0.005	7.8	8.1
9.0	0.000	0.001	0.001	8.5	8.8

Table 7: Relation between separation power and mis-id level

definitions given above. Since no θ dependence was available this separation power is assumed to be constant over the complete θ range.

According to the software chapter of the PANDA Physics Book e/π separation is the most difficult one. Therefore this distribution is assumed to also hold for separating electrons from any other particle species.

As a very naive assumption without a proof the additional separation power provided by the EMC for any other particle combination is taken to be 1σ over the complete phase space covered by the EMC.
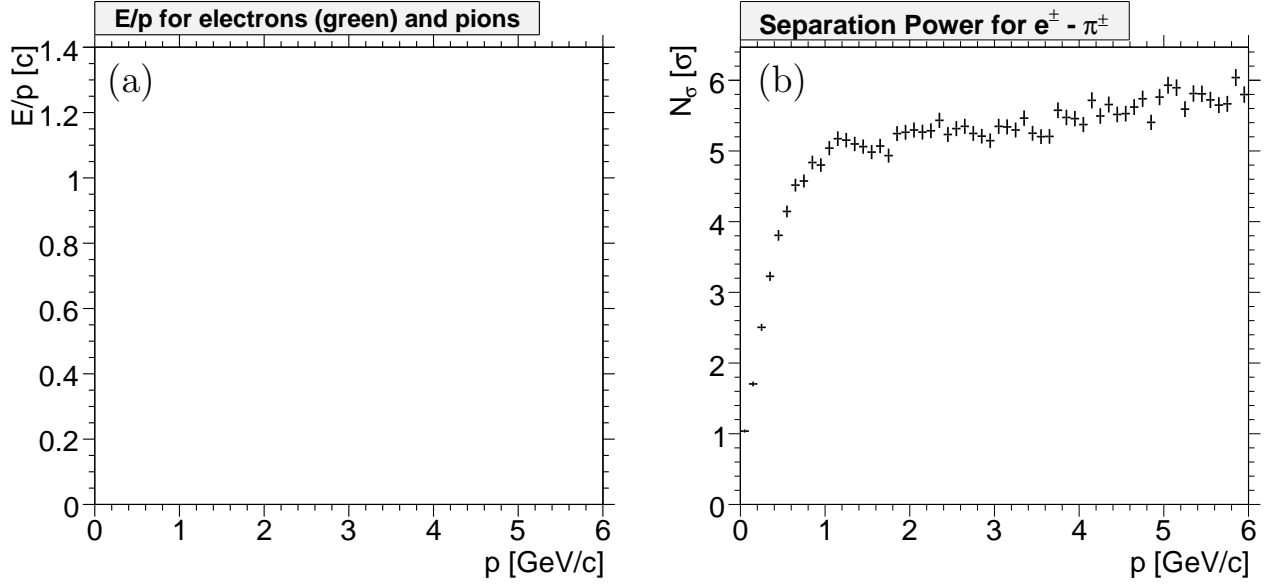
Figure 44: (a) Parameterized distribution of E_{clus}/p for electrons and pions and (b) the resulting separation power N_σ as function of the track momentum p.

4.1.2   Mapping Separation Power

For the purpose of illustration the relationship between kinematic distributions of physics channels and the PID quality the separation power defined in (8) has been determined as 2-dimensional histogram in phase space (p, θ). Therefore it was necessary to computed the mean value μ and standard deviation σ for every bin i with $[p_i \ldots p_i + dp; \theta_i \ldots \theta_i + d\theta]$ for bin widths dp and $d\theta$ for every detector and particle species.

One technical remark: To avoid the computation of $(x - \mu)$ for every measurement in order to determine σ, which is very time consuming for large datasets, the relationship

$$\sigma = \frac{1}{N} \sqrt{\sum x_i^2 - \left(\sum x_i\right)^2} \qquad (17)$$

has been exploited which does not require a previous calculation of the mean value $\mu = \bar{x}$.

In order to evaluate the contributions of the various detectors to the overall classification potential, the separation power defined above has been determined for every single detector component and all possible particle combinations, which add up to the following 10 possibilies:

1. $e^\pm - \mu^\pm$, $e^\pm - \pi^\pm$, $e^\pm - K^\pm$, $e^\pm - p/\bar{p}$,

2. $\mu^\pm - \pi^\pm$, $\mu^\pm - K^\pm$, $\mu^\pm - p/\bar{p}$,

3. $\pi^\pm - K^\pm$, $\pi^\pm - p/\bar{p}$,

4. $K^\pm - p/\bar{p}$.

The results are determined based upon 5 million isotropic distributed single track events with particle momenta up to 6 GeV/c.

Figs. 45 and 47 show as examples the p–θ–dependent separation power for $e^{\pm} - \pi^{\pm}$, $\pi^{\pm} - K^{\pm}$ and $K^{\pm} - p/\bar{p}$ for all 8 detector components

- Micro Vertex Detector (MVD)

- Barrel Time of Flight System (TOF)

- Barrel DIRC

- Disc DIRC

- Ring Image Cherenkov Detector (RICH)

- Electro Magnetic Calorimeter (EMC)

- Straw Tube Tracker (STT)

- Time Projection Chamber (TPC)

under investigation. The color codes in these 2 dimensional representations correspond to the numbers of σ's N_{σ} of separation with a cutoff $N_{\sigma} > 8$, so in the red regions are possibly values above that limit.

To get an impression of the overall particle identification performance the values $N_{\sigma,i}$ from the different detectors i have been combined by quadratic summation according to (13) under the assumption of statistically uncorrelated $N_{\sigma,i}$. Since there are two central tacker options (STT and TPC) which cannot contribute to the same total separation, two different scenarios with either the STT or the TPC are considered separately. Fig. 48 shows the combined information for the STT option and fig. 49 for the detector setup with the TPC as central tracker. All maps are based on the requirement of positiv identification of a particle species. This means, that particle type A is only considered to be dsitinguishable from another particle type B when both create a signal in the particular detector and the given phase space region.

One should keep in mind that the conclusive power of separations involving electrons and muons is limited for the time being since only limited information from the electromagnetic calorimeters and none for the muon detectors has been incorporated so far, which has significant impact on electron and muon identification respectively.
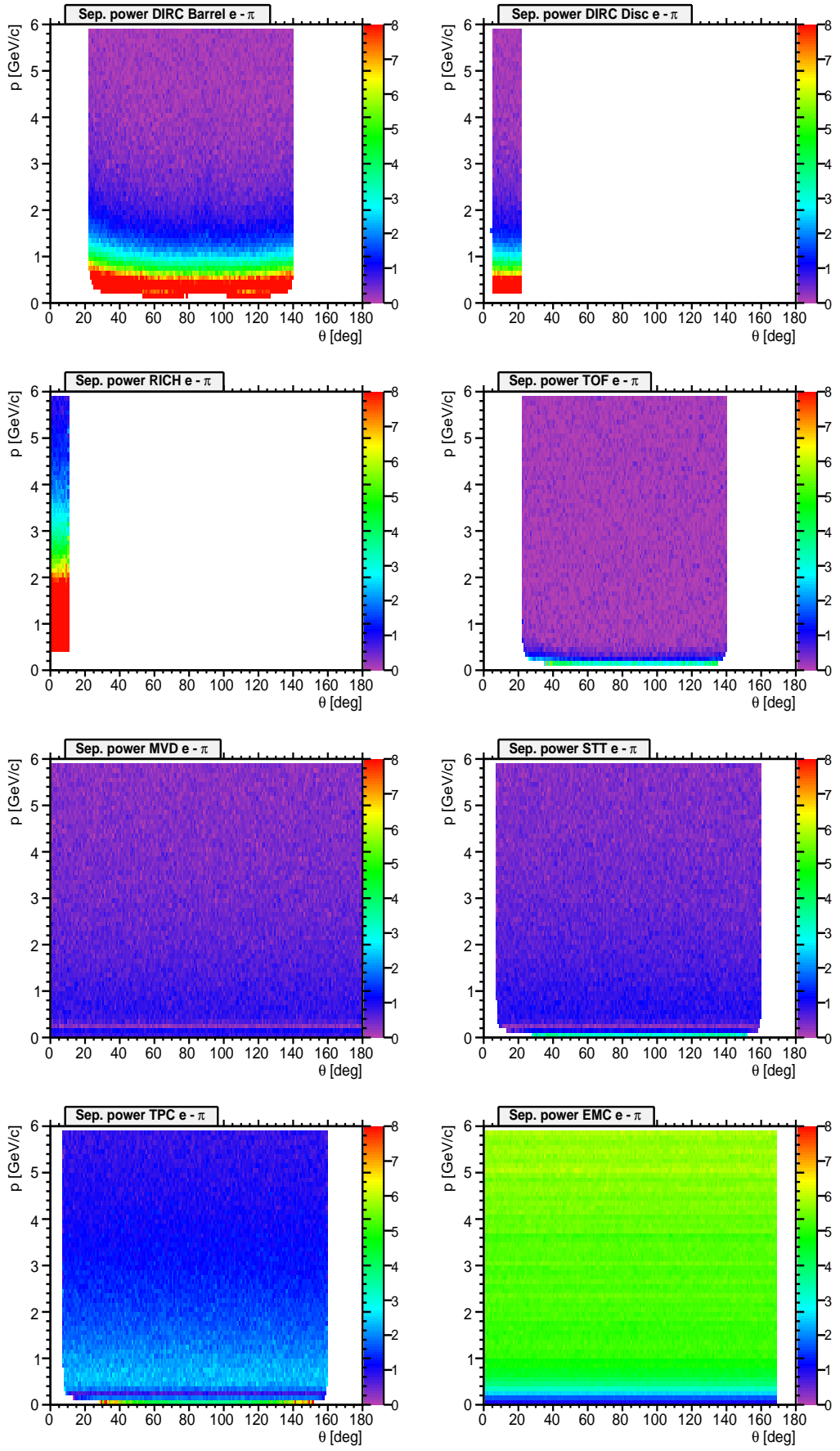
Figure 45: Map of separation power for $e^{\pm}$–$\pi^{\pm}$ separation. Color code corresponds to $N_{\sigma} = 0 \ldots 8$.
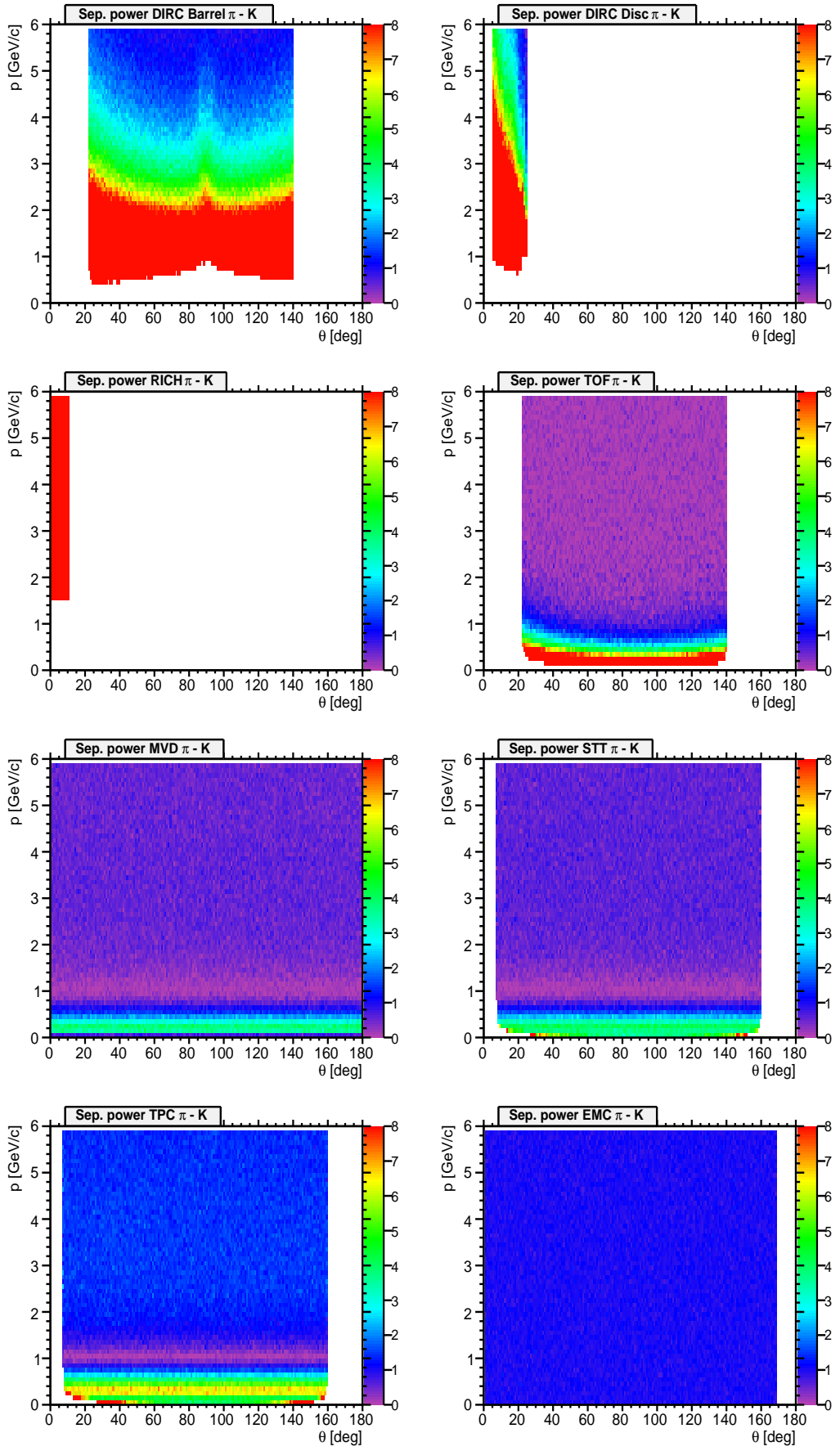
Figure 46: Map of separation power for $\pi^{\pm}$–$K^{\pm}$ separation. Color code corresponds to $N_\sigma = 0 \dots 8$.
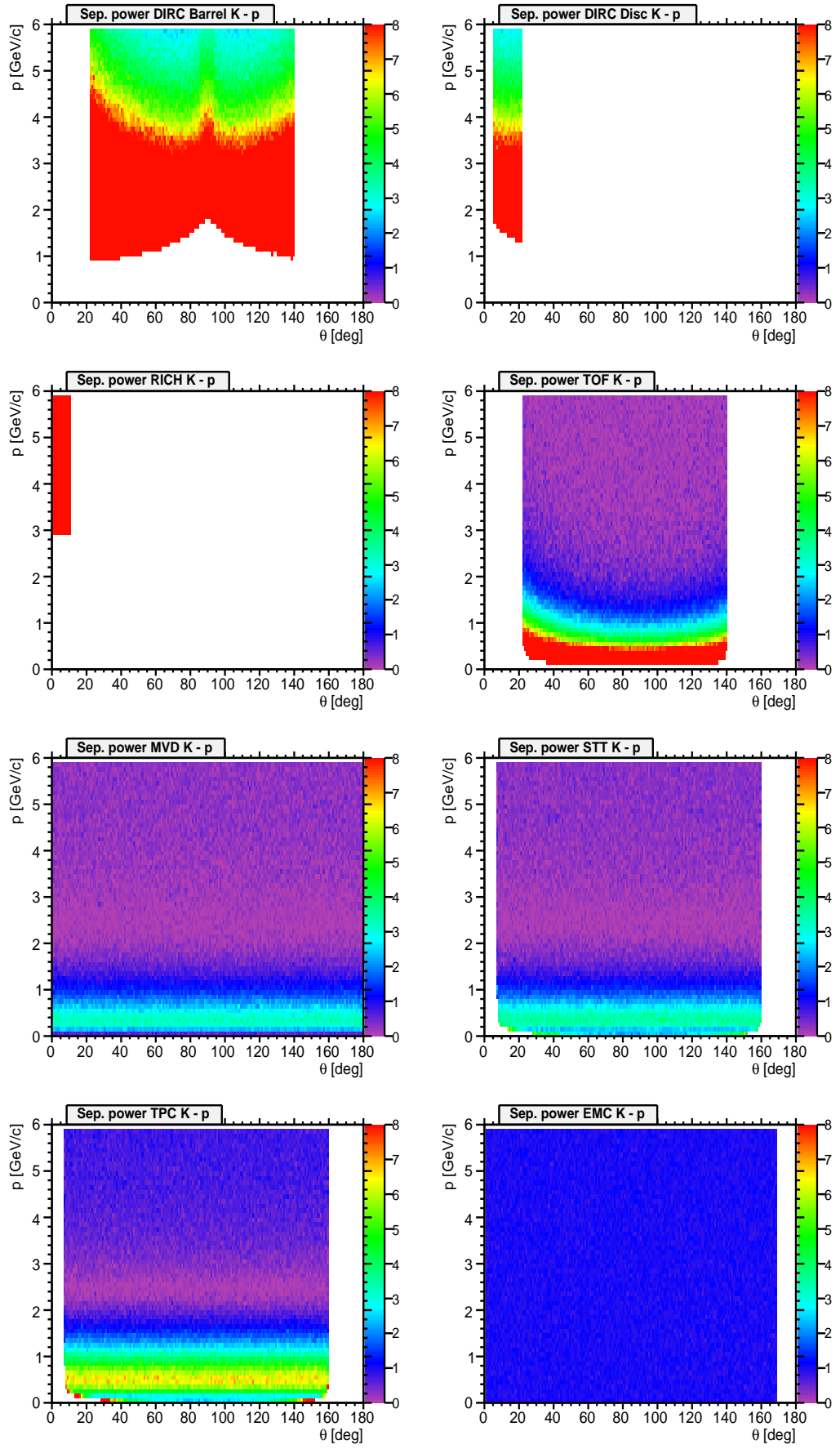
Figure 47: Map of separation power for $K^{\pm}$–$p/\bar{p}$ separation. Color code corresponds to $N_\sigma = 0 \ldots 8$.
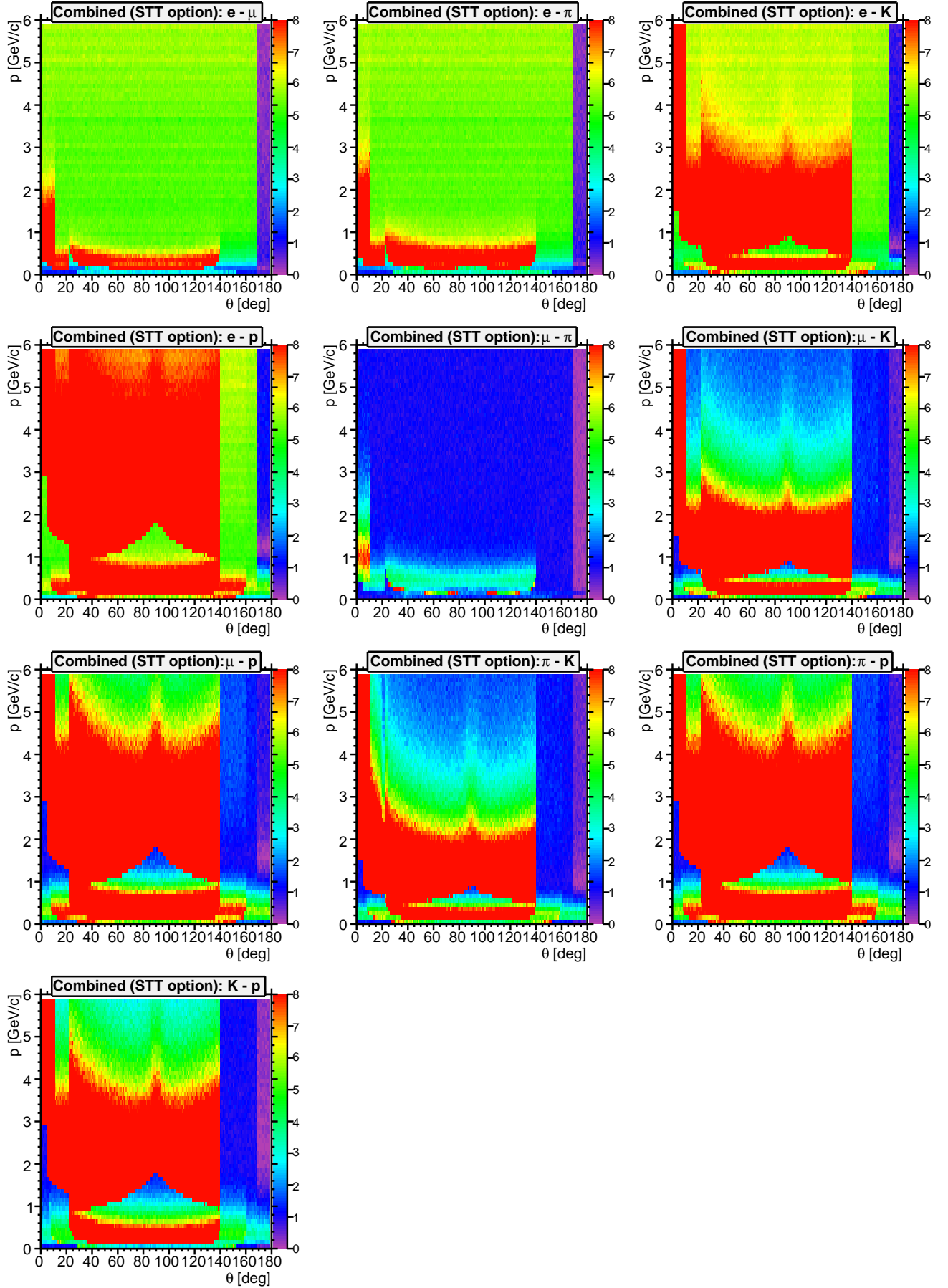
Figure 48: Combined map of Separation Power with STT as central tracker option including the TOF system. Color code corresponds to $N_\sigma = 0 \ldots 8$.
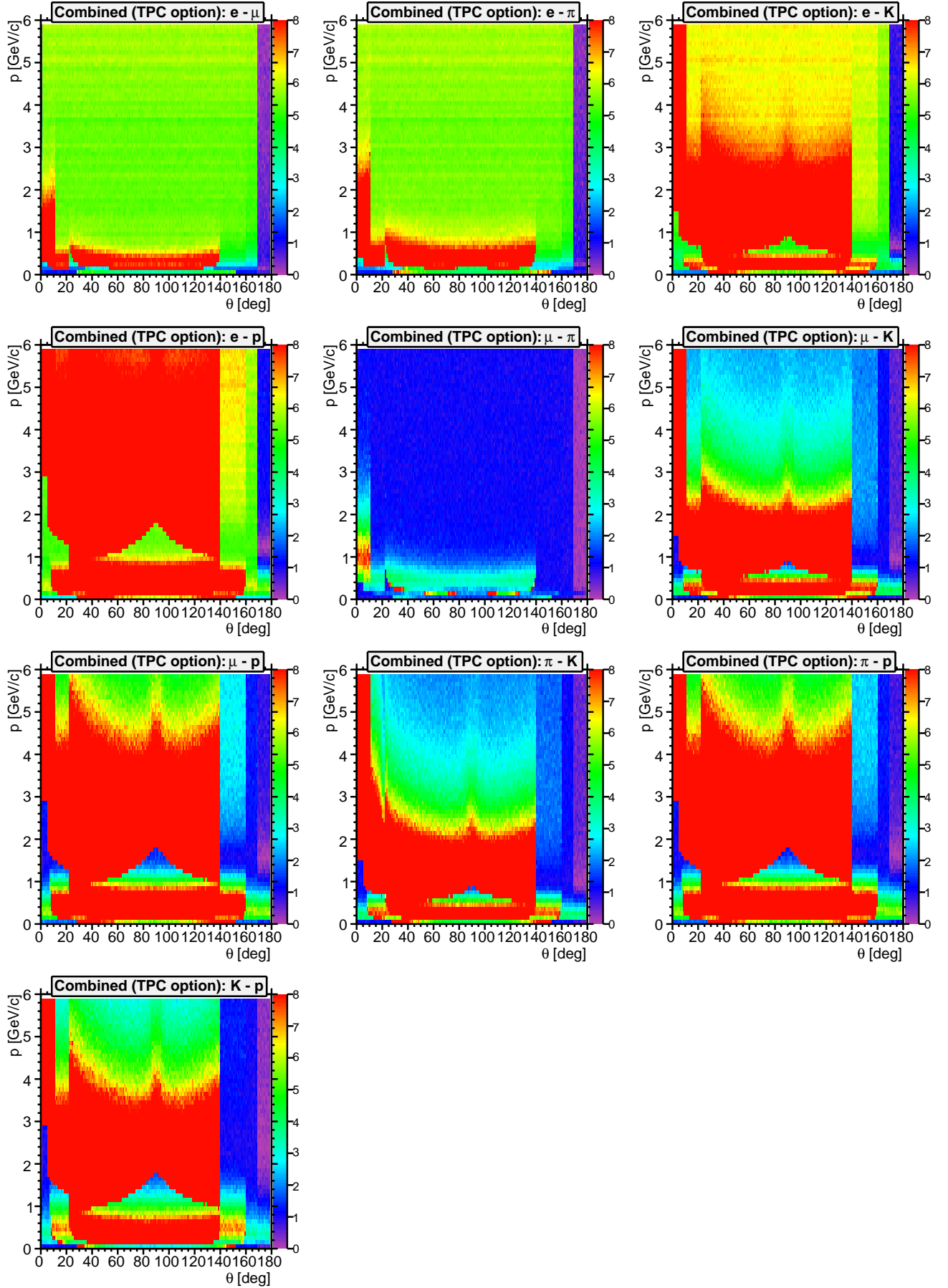
Figure 49: Combined map of Separation Power with TPC as central tracker option including the TOF system. Color code corresponds to $N_\sigma = 0 \ldots 8$.
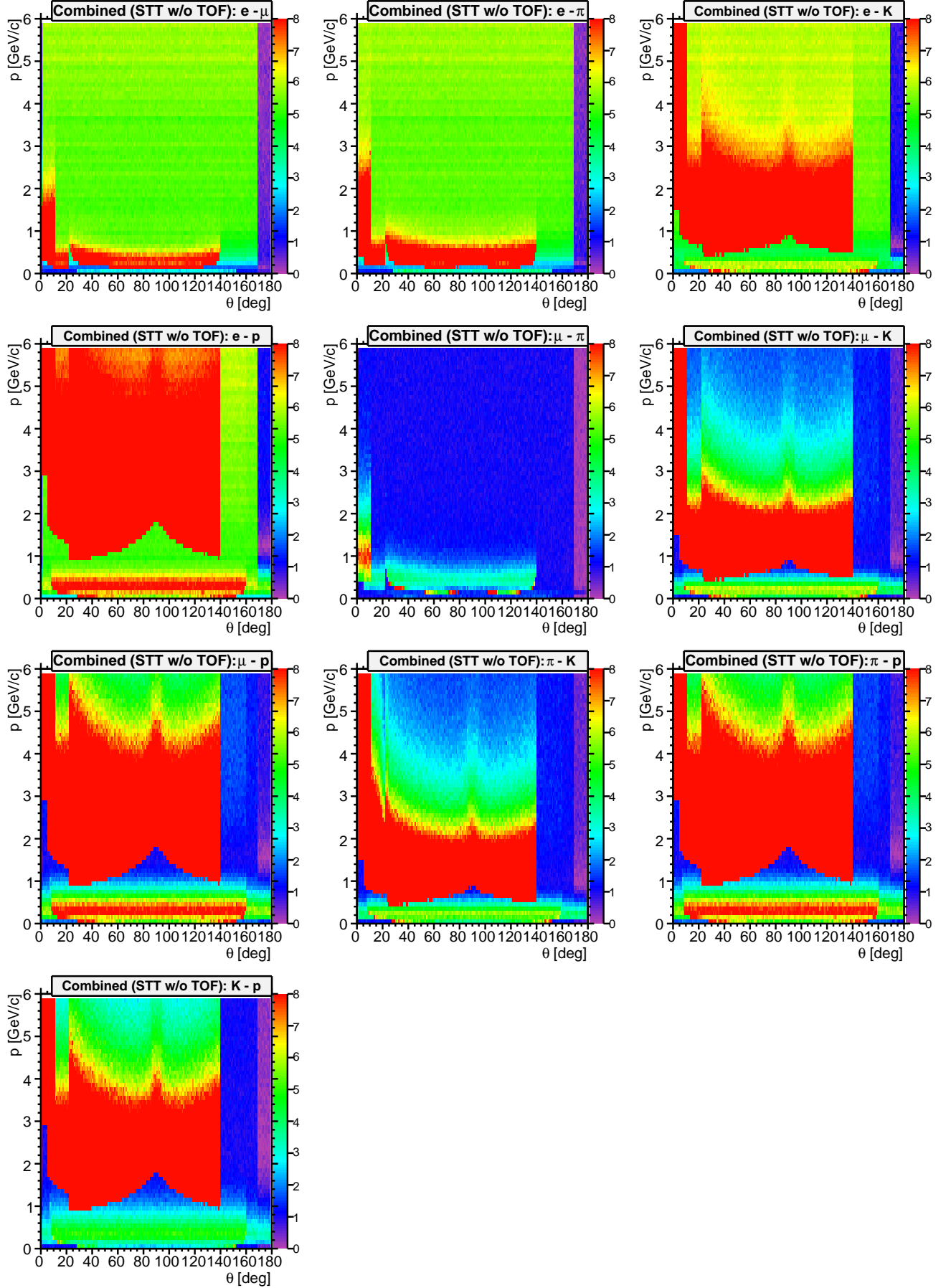
Figure 50: Combined map of Separation Power with STT as central tracker option without the TOF system. Color code corresponds to $N_\sigma = 0 \ldots 8$.
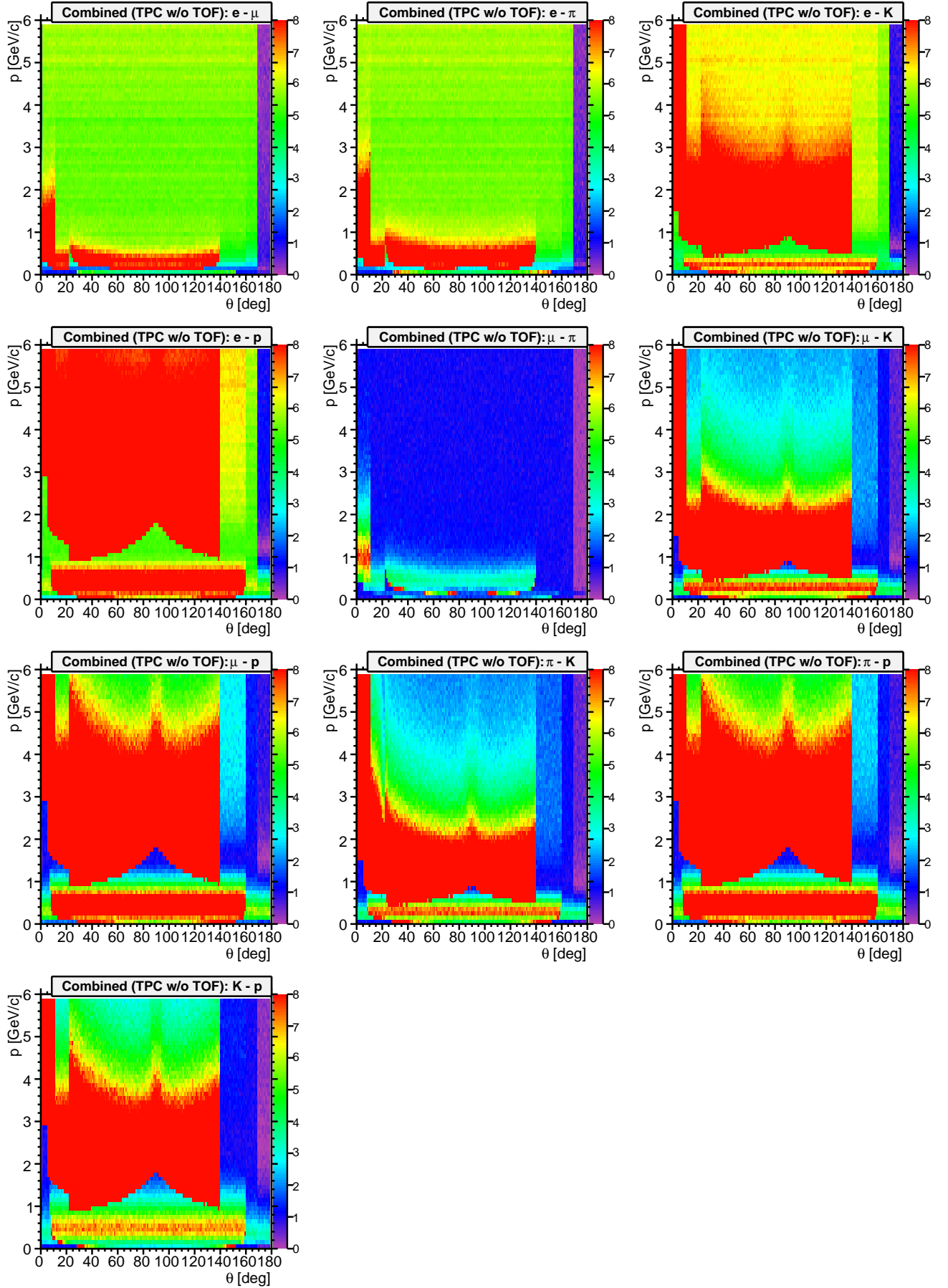
Figure 51: Combined map of Separation Power with TPC as central tracker option without the TOF system. Color code corresponds to $N_\sigma = 0 \ldots 8$.

4.2   Phase Space Plots

The question which has to be answered concerning particle identification is not only how good the classification works or has to work, but also in which region of the phase space one needs good separation, and in which parts one possibly doesn't need almost any.

Therefore it is a crucial task to visualize the kinematic behaviour of various important physics channels to get a better insight to the above issue. Furthermore not only kinematic distributions of signal events are relevant, since good PID is only useful in cases where kinematic overlap of particles of species A from signal events and particles of species B from background events really exists. In scenarios where particles of the same type A appear in signal as well as background events in the same phase space location the background suppression cannot be improved by means of PID.

Following a request of the PID TAG phase space plots from all the reactions relevant for the physics book were produced. The set of plots shows for each particle species of the reaction the particle momentum versus theta angle.

Tab. 9 lists part of the benchmark channels discussed in the PANDA Physics Booklet and some additional ones to study inclusive open charm analysis together with relevant background channels. In particular channels were investigated which might suffer significantly from insufficient PID capabilities[4].

The acronym DPM in the table refers to generic background evens generated with the **D**ual **P**arton **M**odel generator. In the last column references to the corresponding figures are given. Tab. 8 gives some standard decay channels which apply to cases where nothing different is specified in tab. 9.

In figs. 52 - 56 kinematic distributions (momentum p vs. dip angle θ) at various beam momenta are shown for some of the signal-background scenarios listed in 9, one particle species per plot. To easier spot signal and background, the latter ones are colored blue.

Particle	Decay channel
J/ψ	50% e^+e^-, 50% $\mu^+\mu^-$
η	$\pi^+\pi^-\pi^0$
D^0	$K^-\pi^+$
D^+	$K^-\pi^+\pi^+$
D^{*+}	50% $D^0\pi^+$, 50% $D^+\pi^0$
D^{*0}	$D^0\pi^0$
D_s^+	$\phi\pi^+$
ϕ	K^+K^-
Λ	$p\pi^-$
π^0	$\gamma\gamma$

Table 8: Standard decay channels for some particles

---

[4]Signal channels with background reactions comprising the same final state can only be identified due to different kinematic behaviour, which goes beyond the capabilities of PID
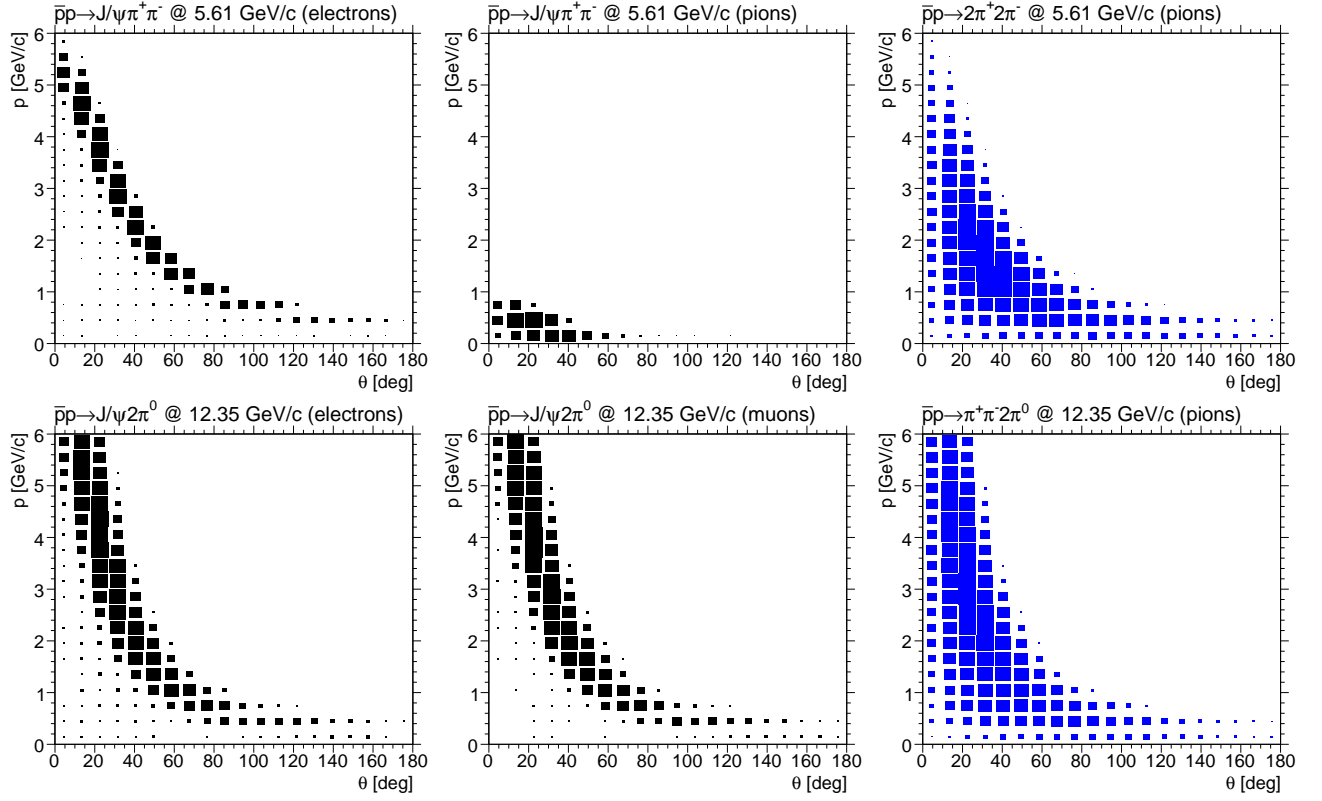
Figure 52: $\bar{p}p \rightarrow J/\psi\pi^+\pi^-$ @ 5.609 GeV/c (top), $\bar{p}p \rightarrow J/\psi2\pi^0$ @ 12.3485 GeV/c (bottom)
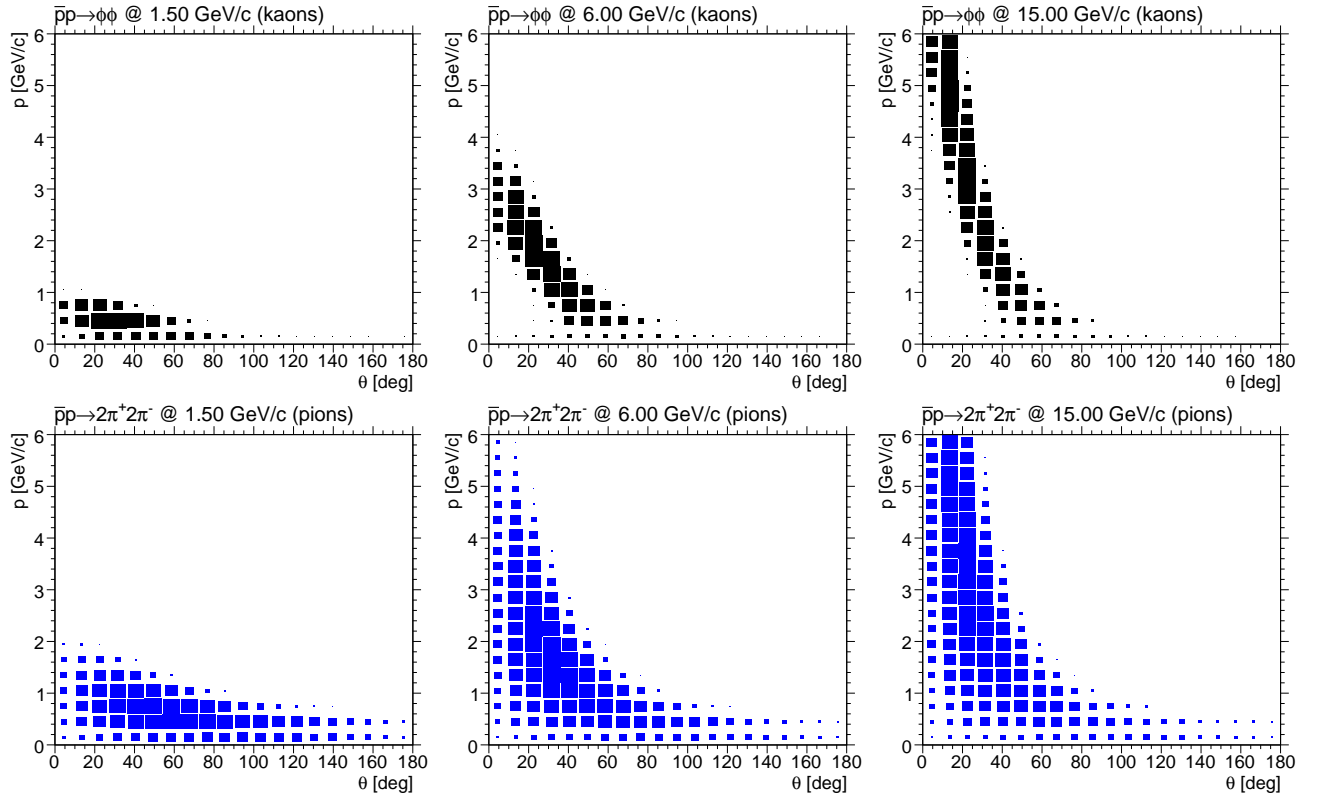
Figure 53: $\bar{p}p \rightarrow \phi\phi$ @ 1.5, 6.0, 15.0 GeV/c
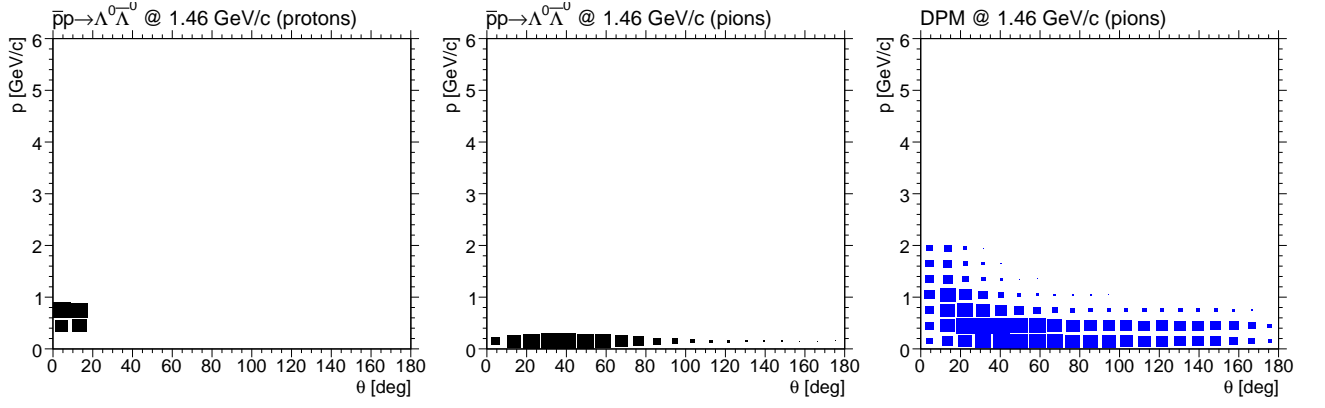
Figure 54: $\bar{p}p \rightarrow \Lambda^0\bar{\Lambda}^0$ @ 1.4601 GeV/c
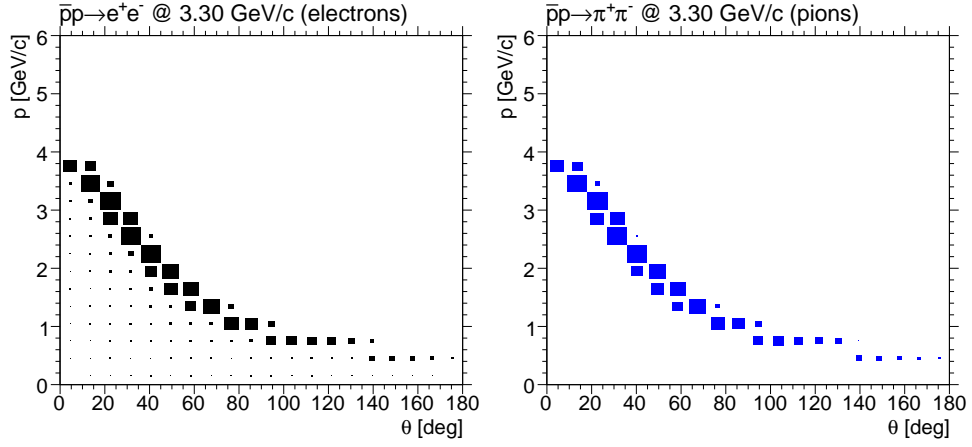
Figure 55: $\bar{p}p \rightarrow e^+e^-$ @ 3.30 GeV/c
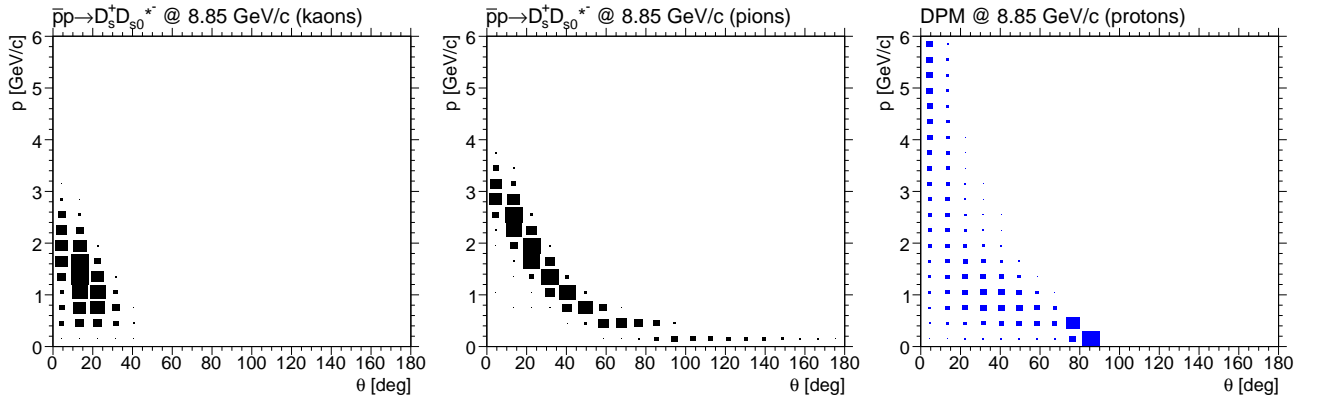
Figure 56: $\bar{p}p \rightarrow D_s^+D_{s0}^*(2317)^-$ @ 8.847 GeV/c

Signal	Background	$p_{\bar{p}}$ [GeV/c]	Fig.
$J/\psi 2\pi^0$	$\pi^+\pi^- 2\pi^0$	5.609 / 6.232 /8.682	
		10.295 / 12.349	52
$J/\psi\pi^+\pi^-$	$2\pi^+ 2\pi^-$	5.609 / 6.232 / 6.988	
		8.682 / 10.295 / 12.349	-
	$2\pi^+ 2\pi^- \pi^0$	6.990 / 8.7	-
$J/\psi\eta$	$2\pi^+ 2\pi^-$	6.080 / 6.990 / 8.7	-
	$3\pi^+ 3\pi^-$	6.080 / 6.990 / 8.7	-
$\phi\phi$	$2\pi^+ 2\pi^-$	1.5 / 6.0 / 12.0 / 15.0	53
	$3\pi^+ 3\pi^-$	1.5 / 6.0 / 12.0 / 15.0	-
$\Lambda^0\bar{\Lambda}^0$	$\Sigma^0\bar{\Sigma}^0$	1.914 / 3.101 / 6.0	54
	DPM	1.460 / 8.0 / 10.0	-
e^+e^-	$\pi^+\pi^-$	1.7 / 3.3 / 7.9 / 10.9 / 15.0	55
$D_s^+ D_{s0}^*(2317)^-$	DPM	8.847	56
	$3\pi^+ 3\pi^- \pi^0$	8.847	-
$D_s^+ D_s^- \gamma$	$3\pi^+ 3\pi^-$	8.847	-
	DPM	7.361 / 7.746 / 8.0 / 12.0 / 15.0	-
$D^{*0}\bar{D}^{*0}\gamma$	DPM	7.746 / 8.0 / 12.0 / 15.0	-
$D^{*+} D^{*-}\gamma$	DPM	7.746 / 8.0 / 12.0 / 15.0	-
$D^0\bar{D}^0\gamma$	DPM	6.488 / 8.0 / 12.0 / 15.0	-
$D^+ D^-\gamma$	DPM	6.488 / 8.0 / 12.0 / 15.0	-

Table 9: Table of Phase Space Channels

4.3   Fast Simulation

In order to get information about phase space (i.e. momentum-polar angle dependence) coverage of the different PID relevant subsystems maps of separation power have been generated based on fast simulations of single track events, i.e. the particles properties are modified with an effective parametrization of detectors responses and PID information is estimated and attached to the resulting particle candidate. Since no microscopic simulation is performed and no exact geometry information is taken into account, the accuracy of this approach is limited, the computation time on the other hand is orders of magnitude shorter offering the possibility to do studies with higher statistics.

4.4   General Technique

In contrast to microscopic simulations using software systems like Geant or Fluka the Fast Simulation is based on acceptance filtering and effective parametrization of all observables of the particular subsystems. Underlying assumption is that the detector system will be able to recontruct the true particles properties like momentum, direction, energy, charge and particle identification (PID) information with uncertainties which are basically uncorrelated and can be described reasonable by parametric models. That could as simple example be gaussian uncertainty for momentum reconstruction with $\delta p/p = \sigma_p = 2\%$, which will be used to modify the true (i.e. generated) tracks parameters accordingly. Additionally a simple geometric accptance requirement will decide whether a track has been detected by a particular detector component or not.

There is a lot of freedom for the implementation of the subsystems, but a minimalistic detector description comprises

- Sensitivity information: Detects charged or neutral particles or both?

- Polar angle coverage: $\theta_{\min} < \theta < \theta_{\min}$

- Gaussian resolution of observables: $\sigma_1, \ldots, \sigma_n$

In order to apply these simulation scheme for every trackable particle coming from the event generator the following procedure is processed:

1. For all detectors D_j, $1 < j < m$

    - In case D_j detects the particle, collect resolution information for all measurable quantities.

2. When no detector detected the track, skip it.

3. Merge all resolution information; when e. g. the particle has been detected by n devices capable of measuring momentum p with resolutions $\sigma_{p,1}, \ldots, \sigma_{p,n}$, the total resolution is

$$\sigma_p = \left(\sum_{i=0}^{n} \frac{1}{\sigma_{p,i}^2} \right)^{-\frac{1}{2}}$$

906   4. Modify the according quantities x of the original track in the way $x' = x + \delta x$, with δx
907   randomly chosen from gaussian distribution $G(\mu = 0, \sigma_x)$

908   5. Create PID information according to the particles properties and attach to the particle; add
909   particle to the track list

910   6. (Optional) Create secondary particles related to particles properties and add to the track
911   list

912   With the so prepared track list analysis can be performed. The interface for doing that is exactly
913   the same as the one for full simulated events.

914   Since this document is focussing on PID the relevant features will be describe in more detail in
915   the following chapters. This will be done effect– or observable–wise instead of detector–wise, since
916   the observed quantities

917   • specific energy loss dE/dx (MVD, TPC, STT)

918   • Cherenkov angle θ_C (Barrel DIRC, Disc DIRC, RICH)

919   • reconstructed squared mass m^2 (TOF)

920   • EMC related measurements like E_{cluster}/p or Zernike momenta

921   • signals from Muon Chambers

922   govern the PID quality and performance and thus are a better ordering criterion. Unfortunately
923   the latter two informations from e.-m. calorimetry and the muon detectors are not implemented
924   in the Fast Simulation for the time being.

925   4.5   Tracking Detectors

926   Although not of direct impact to the field of PID the process of tracking delivers vital information
927   for many of the PID relevant systems. Most of these like e.g. the Time-of-flight (TOF) system
928   or Cherenkov devices (DIRCs and RICH) do not allow for performing a stand alone position
929   measurement, thus their information have to be linked to tracks reconstructed by tracking devices.
930   In addition for the purpose of evaluating PID likelihood functions one usually needs to compute
931   expected values for observables like the Cherenkov angle θ_C or energy loss dE/dx which will be
932   computed for the reconstructed momentum value of the track. This certainly will differ from
933   the true momentum value and therefore track reconstruction accuracy has important impact on
934   likelihood based classification methods.

935   The approach for reconstruction of momenta in the Fast Simulation nevertheless is a very simple
936   one assuming a global momentum resolution $\delta p/p$ for the track reconstruction, since due to tech-
937   nical reasons the particular detector components cannot exchange information. This implies that
938   the tracking devices are not able to feed their information into the PID systems.

4.6   Energy Loss Parametrization

The computation of the specific energy loss is based on the Bethe-Bloch formula

$$-\frac{dE}{dx} = \kappa \cdot \frac{Z}{A} \cdot \frac{e^2}{\beta^2} \cdot \left[\ln \left(\frac{2 m_e \beta^2 \gamma^2 T_{\max}}{I^2} \right) - 2\beta^2 - \delta \right] \qquad \left[\frac{\text{MeV} \cdot \text{cm}}{\text{g}} \right] \tag{18}$$

which very precisely takes into account the processes of charged particles interacting with matter. The formula and detailed information about parameter meanings in this term can be found in [16].

The expression looks quite complicated but can be evaluated straight forward with momentum p and mass m given as input. Additionally one has to substitute a lot of other, material related constants. Since we are not interested in the absolut energy loss but only in relative losses for different particle species it is not crucial to have very precise knowledge about the fixed parameters.

In order to generate a simulated detector response for detectors capable of measuring dE/dx a gaussian resolution $\sigma_{dE/dx}$ has been set for each of them. The simulated measured $(dE/dx)_{\text{sim}}$ value thus has been simply computed with formula (18) to

$$\left(\frac{dE}{dx} \right)_{\text{sim}} = \left(\frac{dE}{dx} \right) + \delta \left(\frac{dE}{dx} \right) \tag{19}$$

with randomly chosen value $\delta(dE/dx)$ from a gaussian distribution $G(\mu = 0, \sigma_{dE/dx})$.

4.7   Cherenkov Angle Parametrization

Basic theoretical information about the origin of Cherenkov radiation can be found elsewhere and will not be discuss here. The Cherenkov angle defined as the opening angle of the cone of radiation relativ to the direction of the incident charged particles momenta in medium with refractive index n is given by the expression

$$\theta_C = \arccos \left(\frac{1}{\beta \cdot n} \right) \tag{20}$$

with $\beta = p \cdot c / E$ being the velocity of the particle. Obviously computation of the expected Cherenkov angle for any given particle detected by the specific detector is straight forward. Key ingredient of the parametrization of the detector response is the resolution estimation. In case of DIRC detectors experience from the working device in the BaBar experiment tells us that the overall reconstruction resolution of the Cherenkov angle can be based on a single photon resolution $\sigma_{\text{s.phot.}} \approx 10$ mrad. Responsible for the overall resolution then exclusively is the number of detected Cherenkov photons N through

$$\sigma_{\text{tot}} = \frac{\sigma_{\text{s.phot.}}}{\sqrt{N}},$$

which is simple count statistics. This number N has to be estimated and depends on

- the number of generated photons

$$N_0 = 2\pi \cdot \alpha \cdot L \left(\frac{1}{\lambda_{\min}} - \frac{1}{\lambda_{\max}} \right) \cdot \sin^2 \theta_C = 2\pi \cdot \alpha \cdot L \left(\frac{1}{\lambda_{\min}} - \frac{1}{\lambda_{\max}} \right) \cdot \left(1 - \frac{m^2 + p^2}{p^2 \cdot n^2} \right) \tag{21}$$

  with parameters

967   − fine structure constant α

968   − trajectory length L in the radiator material

969   − mass and momentum m and p of the incident track

970   − wave length region $\lambda_{\min}$ and $\lambda_{\max}$ where the photon detector is sensitive and

971   − refraction index n

972   • the trapping fraction r_{trap} which is the fraction of the photons kept in the radiator/lightguide
973   due to total reflection and

974   • the detection efficiency ϵ of the photon detector, e.g. a photo multiplier tube (PMT)

975 In order to derive the path length L in the material one has to distinguish between the different
976 Cherenkov devices.

977 In case of the **Barrel DIRC** on first of all has to compute the curvature due to the motion of a
978 charged particle in a magnetic solinoidal field $B = B_z$. The radius r of the circular shape in (x, y)
979 projection is given by

$$r = \frac{p_t}{q \cdot B} = \frac{3.3356 \cdot p_t \ [\text{GeV}/c]}{B \ [\text{T}]}. \tag{22}$$

980 for a particle with charge $q = \pm e$ and transverse momentum $p_t = p \cdot \sin\theta$. Based on this one can
981 calculate the entering angle ψ in ϕ direction to

$$\psi = \arccos \frac{r_B}{2 \cdot r} \tag{23}$$

982 with r_B being the radius of the DIRC Barrel i.e. the distance between the bars and the beam
983 line. Here it is obvious that particles with $2 \cdot r < r_B$ will not hit the detector at all defining a
984 minimum transverse momentum $p_{t,\min}$. The path length after some geometrical considerations
985 then computes to

$$L \approx d_{\text{bar}} \cdot \sqrt{\frac{1}{\sin^2\theta} + \frac{1}{\tan^2\psi}} \tag{24}$$

986 where d_{bar} is the thinkness of the radiator bars and θ the dip angle of the helix of the track. The
987 expression is an approximation because curvature within the bar has been neglected. This leads
988 to significant wrong values for particles with $2 \cdot r \approx r_B$.

989 For the **Disc DIRC** and the **RICH** computing the radiator path length is much simpler. Here
990 L only depends on the dip angle and the radiator thinkness d_{rad} resulting in

$$L = \frac{d_{\text{rad}}}{\cos\theta}. \tag{25}$$

991 Also here no curvature within the radiators has been taken into account. This anyway would lead
992 to more complicated estimates since angular changes along the radiator path results in systematic
993 worsening of the Cherenkov angle which is neglected completely.

994 Finally we still need the trapping fraction r_{trap} to determine the number of detected photons. There
995 is no known analytic expression to compute this, thus 2 dimensional lookup tables $r_{\text{trap}}(\theta, p)$ for
996 every particle species have been prepared. Figure 57 shows as an example the trapping fraction
997 in the Barrel DIRC bars for muons and protons as a function of momentum p and dip angle θ.
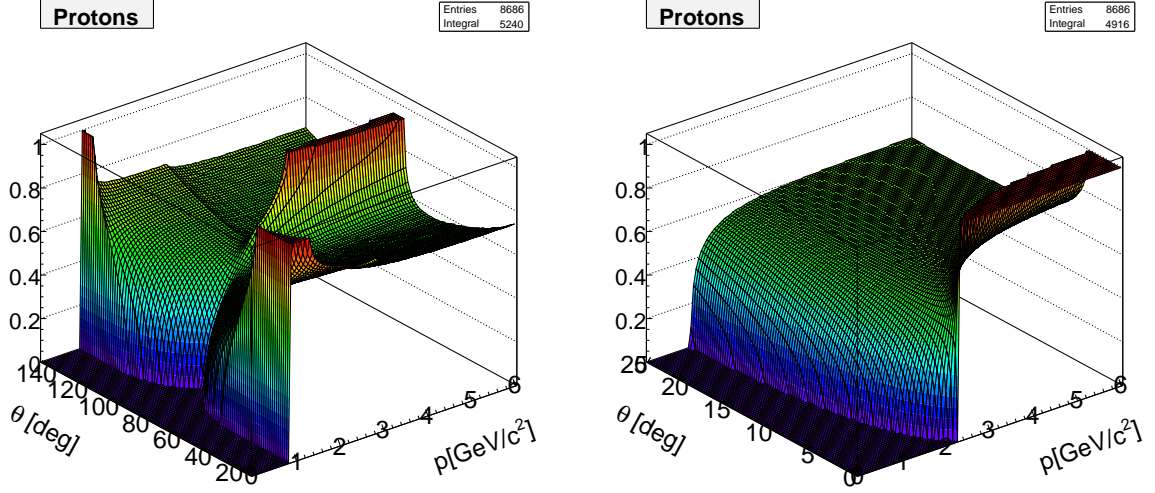
Figure 57: 2-dimensional picture of the trapping fraction for protons in the Barrel DIRC (left) and the Disc DIRC as a function of momentum p and dip angle θ.

With the path length L one can evaluate expression (21) so that the detected number of photons can be estimated to

$$N = N_0' \cdot \epsilon \cdot r_{\text{trap}} \tag{26}$$

where the N_0' is randomly generated from Poisson distibution with input value $\lambda = N_0$. This directly leads to the expected resolution σ_{tot} which is taken as the absolute uncertainty of the measurement of the Cherenkov angle. The simulated measured Cherenkov angle thus has been computed with formula (20) to

$$\theta_{C,\text{sim}} = \theta_C + \delta\theta_C \tag{27}$$

with randomly chosen value $\delta\theta_C$ from a gaussian distribution $G(\mu = 0, \sigma_{\text{tot}})$.

4.8   Time Of Flight Parametrization

From the geometrical point of view the calculation of the expected time of flight of a particle has similarities to the considerations done in 4.7 for the Barrel DIRC, since the TOF detector has also cylindrical shape. This requires also the particles with curvatures given by equation (22) to have a minimum transverse momentum p_t to reach the detector and produce a signal.

In order to compute the time of flight $t_{\text{TOF}} = s/v$ one in principal only needs the traveled distance s and the velocity v of the particle. While the latter one is simple to get by via the particles $\beta = p \cdot c/E$, the distance is not so easy to calculated due to the tracks curvature in the magnetic field. Nevertheless the calculation can be simplified exploiting the fact that the particles motion in z direction is independent of that one in th (x, y) plane. Therefore t can also be calculated via the ratio of the travelled angle Φ and the angular velocity ω

$$t_{\text{TOF}} = \frac{\Phi}{\omega} = \frac{1}{\omega} \cdot 2 \arcsin \frac{r_B}{2r} \tag{28}$$
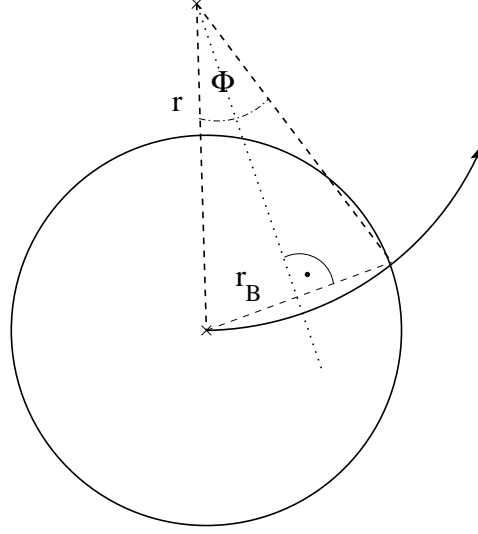
Figure 58: Projection of particle trajectory to (x, y) plane in order to determine Φ.

with the determination of Φ illustrated in fig. 58. The angular velocity in the projected plane is given by

$$\omega = \frac{B}{3.3356 \cdot E} \tag{29}$$

for a magnetic field B [T] and E [GeV]. With these expressions one can derive the true expected time of flight. What now has to be simulated is the expected accuracy of the measurement achieved by the detector. This depends on the time resolution assumed to be $\sigma_t \approx 100$ ps on one hand and on the resolution connected to track reconstruction on the other hand since the transverse momentum $p_t = p \cdot \sin(\theta)$ is needed to compute the flight length. Only a relative uncertainty $\sigma_p = \delta p/p \approx 2\%$ for the reconstructed absolute value of the momentum has been taken into account with respect to this, neglecting errors in polar angle measurement.

This results in measured values

$$t'_{\text{TOF}} = t_{\text{TOF}} + \delta t \tag{30}$$
$$p' = p \cdot (1 + \delta p) \tag{31}$$

with gaussian distributed deviations δt and δp according to $G(\mu = 0, \sigma_t)$ and $G(\mu = 0, \sigma_p)$. The primes denote from now the 'measured' or 'simulated' quantities. Now one basically has to reverse the process from above to get the simulated reconstructed value for the energy E needed to compute the squared mass

$$m'^2 = E'^2 - p'^2 \tag{32}$$

which acts as the observable of the TOF detector. Starting point is eq. (29) which forms to $E' = B/(3.3356 \cdot \omega')$ etc. The resulting term depending only on the quantities t'_{TOF}, p' and θ looks like

$$m'^2 = \left(\frac{B \cdot t'_{\text{TOF}}}{2 \cdot 3.3356 \cdot \arcsin\left(\frac{r_B}{2 \cdot 3.3356 \cdot p' \sin(\theta)} \right)} \right)^2 - p'^2 \tag{33}$$

4.9 Parameter Settings

Tab. 10 presents the complete set of relevant parameters which were used in the Fast Simulation to extract most of the results presented in this note, in particular in section 5.3.

Meaning	Quantifier	Value
Global		
Magnetic Field Strength	$B = B_z$	2 T
Relative Momentum Resolution	σ_p/p	1 %
Micro Vertex Detector (MVD)		
Angular Acceptance	$[\theta_{\min}; \theta_{\max}]$	$[0.0°; 180.0°]$
Relative dE/dx Resolution	$\sigma_{dE/dx}$	22 %
Straw Tube Tracker (STT)		
Angular Acceptance	$[\theta_{\min}; \theta_{\max}]$	$[7.765°; 159.44°]$
Relative dE/dx Resolution	$\sigma_{dE/dx}$	20 %
Inner Radius	R_I	15 cm
Time Projection Chamber (TPC)		
Angular Acceptance	$[\theta_{\min}; \theta_{\max}]$	$[7.765°; 159.44°]$
Relative dE/dx Resolution	$\sigma_{dE/dx}$	8 %
Inner Radius	R_I	15 cm
Barrel DIRC		
Angular Acceptance	$[\theta_{\min}; \theta_{\max}]$	$[22.0°; 140.0°]$
Inner Radius	R_I	48 cm
Single Photon Resolution	σ_{ph}	10 mrad
Thickness of Slab	d_S	1.7 cm
Refractive Index of Quarz	n_Q	1.472
Total Photon Detector Efficiency	ϵ_{PD}	7.5 %
Disc DIRC		
Angular Acceptance	$[\theta_{\min}; \theta_{\max}]$	$[5.0°; 22.0°]$
Single Photon Resolution	σ_{ph}	10 mrad
Thickness of Disc	d_D	1.7 cm
Refractive Index of Quarz	n_Q	1.472
Total Photon Detector Efficiency	ϵ_{PD}	7.5 %
Ring Image Cherenkov Detector (RICH)		
Angular Acceptance	$\theta_{\min}$	0.0°
	$\alpha_{\max}$ (vert.)	5.0°
	$\alpha_{\max}$ (hor.)	10.0°
Single Photon Resolution	σ_{ph}	10 mrad
Thickness of Radiator	d_D	1 m
Refractive Index of Radiator	n_R	1.05
Total Photon Detector Efficiency	ϵ_{PD}	7.5 %
Time of Flight system (TOF)		
Angular Acceptance	$[\theta_{\min}; \theta_{\max}]$	$[22.0°; 140.0°]$
Inner Radius	R_I	38 cm
Total Time Resolution	σ_t	141 ps

Table 10: Parameter Settings used for the Fast Simulation

5 Evaluation

5.1 Potential of the Subsystems

5.2 Matching of the Subsystems

5.3 Maps of Separation

In order to evaluate the PID performance applied to specific physics channels the information about

1. kinematic distribution of signal channel

2. kinematic distribution of possible bakcground

3. separation power in phase space

have been combined in the way, that signals distributions for every particle species have been projected on the according map of separation power with either STT or TPC option. Since the implementation of the TOF detector is still under investigation at the time of writing, the studies for both options also have been performed without the information of the TOF system.

Background has been taken into account by punching the according separation map with its distribution leaving only regions colored where in fact background particles appear.

For instance to determine the PID quality for kaons from $\bar{p}p \to D^+D^-\gamma$ reactions at a particular energy against pions from DPM background, the phase space histogram of kaons from the signal channel has been projected on the $\pi^\pm - K^\pm$ separation map which has been punched with the distribution of pions from DPM events at the same total energy.

This procedure gives access to the information how good a particle type for a specific signal channel can be identified. In particular it offers the possibility to identify regions with insufficient PID quality. As a quantitative measure for the goodness or badness of a certain projection two quantities have been determined:

1. the fraction of the signal f where separation power is $N_\sigma < 8$

2. the average σ_{avg} for that region

As an arbitrary criterion all projections fulfilling

$$f > 0.2 \quad \&\& \quad \sigma_{\mathrm{avg}} < 5\sigma \qquad \text{or} \qquad f > 0.5$$

have been listed as problematic cases. Tab. 11 contains all channels with $\bar{p}$ momentum below 8.7 GeV/c, tab. 12 shows channels with $p_{\bar{p}} > 8.7$ GeV/c. In order to assign additional structure to this vast amount of information the numbers have been colored according to the severeness of PID deficiency. Since intuitively higher values f and smaller values σ_{avg} can be considered as bad

and vice versa smaller fractions f and larger σ_{avg} are considered as good, the coloring scheme was chosen as:

$$f \quad = \quad 0\ldots 30 \quad \boxed{\ldots 40} \quad \ldots 50 \quad \ldots 60 \quad \ldots 70 \quad \ldots 80 \quad \ldots 90 \quad \boxed{\ldots 100} \, \%$$

$$\sigma_{\mathrm{avg}} \quad = \quad \boxed{0\ldots 1.5} \quad \ldots 2.0 \quad \ldots 2.5 \quad \ldots 3.0 \quad \ldots 3.5 \quad \ldots 4.0 \quad \boxed{\ldots 4.5} \quad \ldots 5.0 \; \sigma$$

with values marked red being worse than values marked green or yellow. The four different combinations (f, σ) correspond to the combinations

1. TPC option including TOF

2. STT option including TOF

3. TPC option w/o TOF

4. STT option w/o TOF

i. e. to contrast TPC and STT PID performance compare either (f_1, σ_1) and (f_2, σ_2) with TOF or (f_3, σ_3) and (f_4, σ_4) without TOF. The PID hypothesis column has always been colored with the 'worst' color in the row in order to easier spot separation problems between particular hypothesis.

Figs. 59 – 61 present the corresponding plots for some selected channels. Each column shows the results for one particular channel and the four different detector setups in the same order from top to bottom as given in the list. In tabs. 11 and 12 those channels are marked with a bullet ($\bullet$) in the PID column.
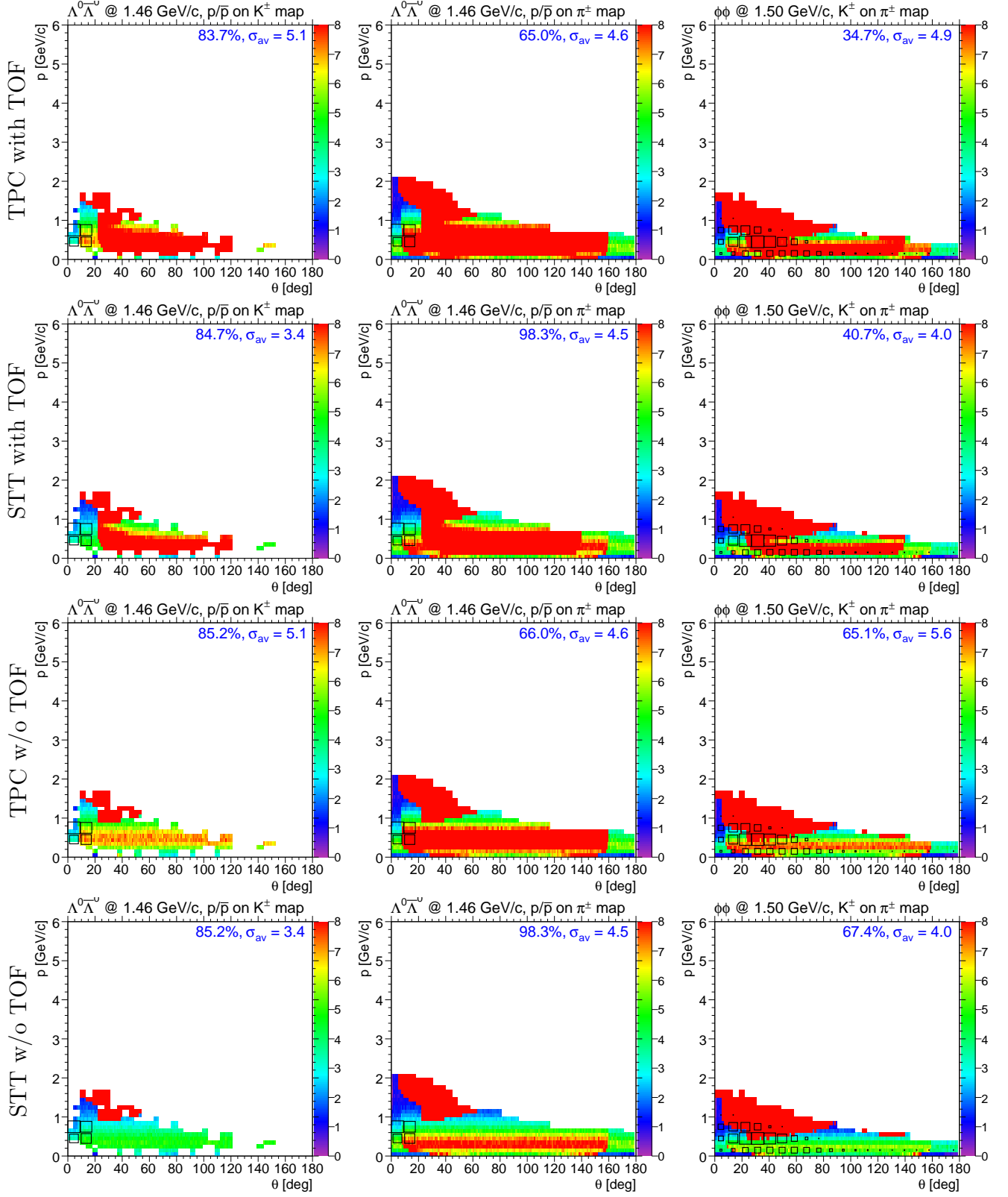
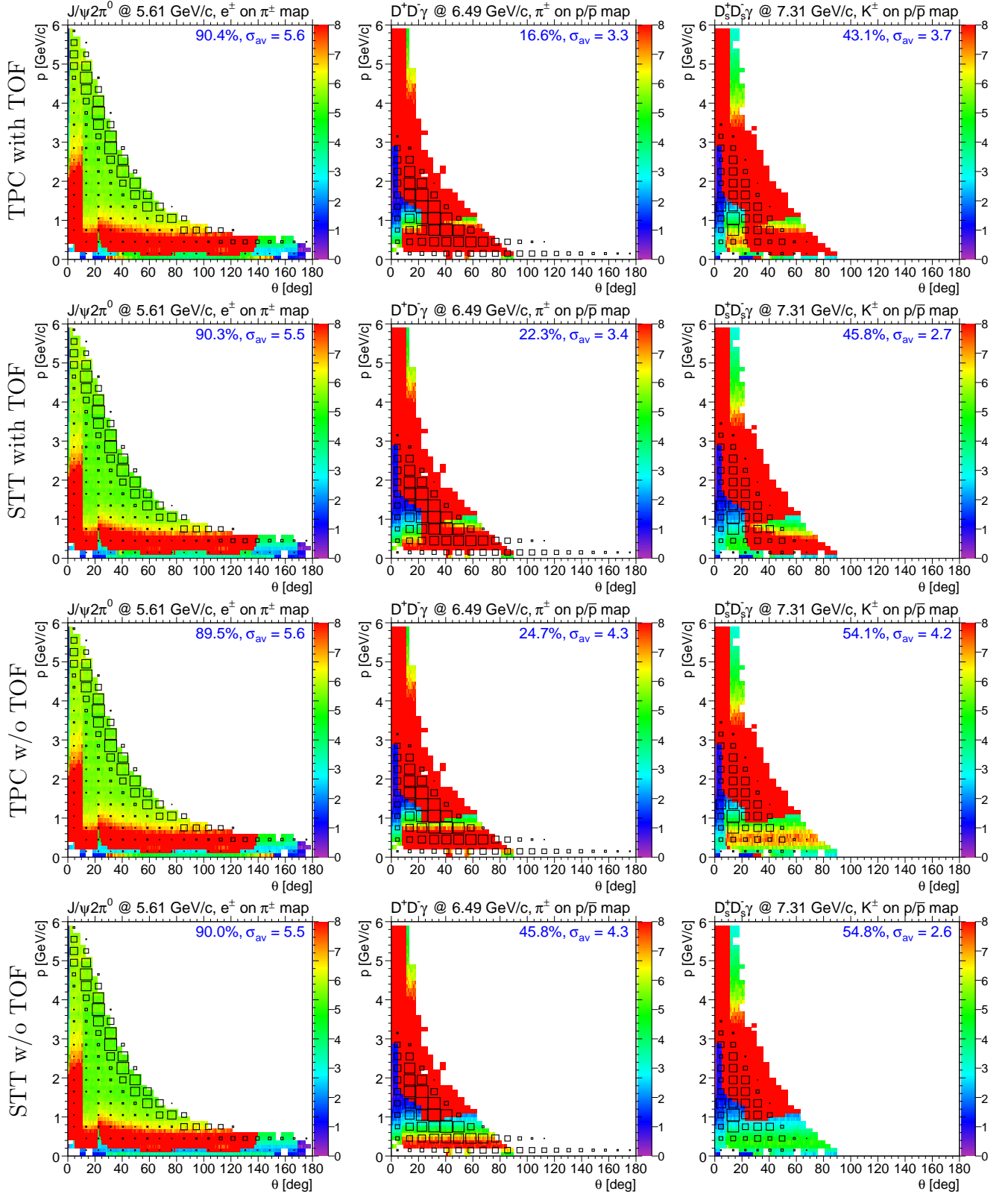Figure 59: Projection of kinematic distributions on separation maps (1).

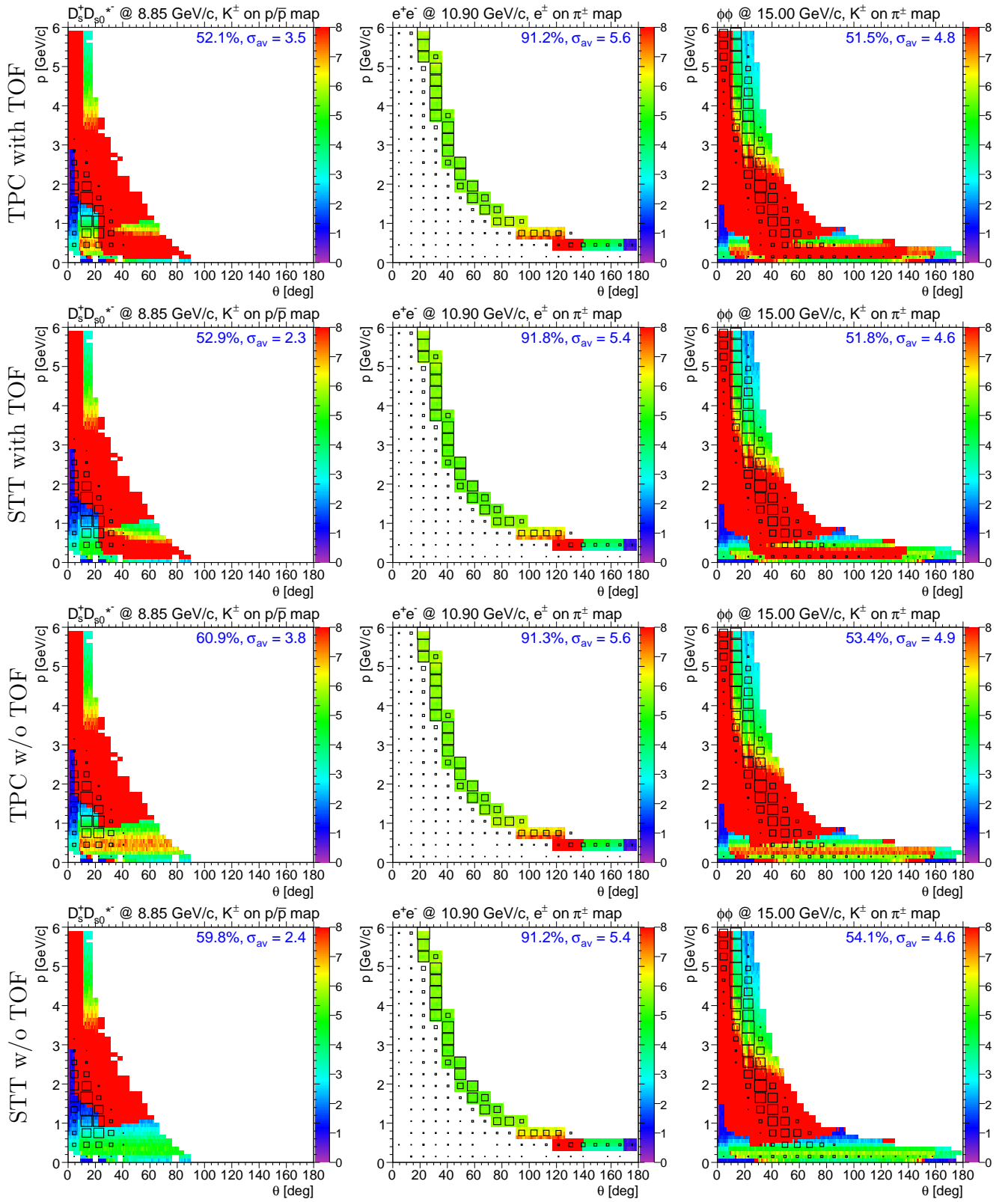Figure 60: Projection of kinematic distributions on separation maps (2).

Figure 61: Projection of kinematic distributions on separation maps (3).

$p_{\bar p}$ [GeV/c]	Signal	PID	f_1 [%]	σ_1	f_2 [%]	σ_2	f_3 [%]	σ_3	f_4 [%]	σ_4
1.460	$\Lambda^0\bar\Lambda^0$	π - e	64	4.0	64	3.3	64	3.7	66	2.9
		π - μ	30	2.6	30	2.5	31	2.5	30	2.3
		p - e	49	5.3	72	5.6	50	5.3	72	5.6
		p - π ●	63	4.6	98	4.5	65	4.6	98	4.5
		p - K ●	85	5.1	85	3.4	84	5.0	84	3.4
1.500	$\phi\phi$	K - π ●	34	4.9	41	4.0	65	5.6	65	4.0
1.700	e^+e^-	e - π	91	5.9	92	5.6	91	5.9	92	5.6
3.300	e^+e^-	e - π	93	5.7	93	5.5	94	5.7	93	5.5
5.609	$J/\psi 2\pi^0$	e - π ●	90	5.7	89	5.5	90	5.6	90	5.5
		μ - π	92	1.3	92	1.2	92	1.2	92	1.2
	$J/\psi\pi^+\pi^-$	e - π	88	5.7	88	5.5	88	5.6	89	5.5
		μ - π	92	1.3	91	1.2	92	1.3	92	1.2
6.080	$J/\psi\eta$	e - π	65	5.6	64	5.5	65	5.6	65	5.5
6.232	$J/\psi 2\pi^0$	e - π	90	5.6	89	5.5	89	5.6	89	5.5
		μ - π	93	1.3	92	1.2	92	1.2	92	1.2
	$J/\psi\pi^+\pi^-$	e - π	90	5.6	91	5.5	91	5.6	91	5.5
		μ - π	93	1.3	94	1.2	94	1.2	94	1.2
6.488	$D^+D^-\gamma$	π - p ●	16	3.4	21	3.5	25	4.5	45	4.3
		K - p	23	4.0	27	3.4	38	4.9	38	3.0
6.988	$J/\psi\pi^+\pi^-$	e - π	92	5.6	93	5.5	93	5.6	93	5.5
		μ - π	96	1.2	96	1.2	96	1.2	96	1.2
6.990	$J/\psi\eta$	e - π	77	5.6	77	5.5	77	5.6	77	5.5
7.314	$D_s^+D_s^-\gamma$	π - p	13	4.1	23	4.6	21	4.9	43	4.8
		K - p ●	42	3.7	44	2.7	54	4.2	54	2.6
7.746	$D^{*+}D^{*-}\gamma$	π - K	17	4.2	18	3.9	20	4.5	21	3.7
		π - p	24	4.8	27	4.8	28	4.9	38	4.8
		K - p	14	5.0	17	4.7	24	5.4	25	3.4
	$D_s^+D_s^-\gamma$	π - p	13	4.0	23	4.4	19	4.8	40	4.8
		K - p	41	3.6	43	2.7	51	4.1	51	2.6
7.900	e^+e^-	e - π	91	5.6	91	5.5	91	5.6	91	5.5
8.000	$\Lambda^0\bar\Lambda^0$	π - K	22	4.2	24	3.2	35	5.2	36	3.5
		π - p	35	3.8	49	3.8	45	4.4	80	4.6
	$D^{*0}\bar D^{*0}\gamma$	K - p	10	6.5	13	5.9	19	6.1	20	4.2
	$D^+D^-\gamma$	π - p	17	3.4	22	3.5	25	4.4	44	4.3
		K - p	23	4.0	26	3.3	36	4.6	35	3.0
	$D^0\bar D^0\gamma$	K - p	13	6.1	17	5.6	23	5.9	22	4.4
	$D_s^+D_s^-\gamma$	π - K	12	4.9	14	3.7	20	5.4	20	3.6
		π - p	13	4.1	23	4.5	22	4.8	41	4.8
		K - p	40	3.6	43	2.6	50	4.0	51	2.6
	$D^{*+}D^{*-}\gamma$	π - K	22	4.0	23	3.5	25	4.4	26	3.3
		π - p	26	4.3	31	4.6	29	4.5	40	4.6
		K - p	13	5.1	17	4.5	25	5.4	24	3.6
8.682	$J/\psi\pi^+\pi^-$	e - π	91	5.6	93	5.5	92	5.6	93	5.5
		μ - π	96	1.3	96	1.2	96	1.3	96	1.2
	$J/\psi 2\pi^0$	e - π	92	5.6	92	5.5	92	5.6	92	5.5
		μ - π	96	1.3	96	1.2	96	1.3	96	1.2

Table 11: Table of projection results (1). Marked channels (●) appear in figs. 59 – 61.

$p_{\bar{p}}$ [GeV/c]	Signal	PID	f_1 [%]	σ_1	f_2 [%]	σ_2	f_3 [%]	σ_3	f_4 [%]	σ_4
8.700	$J/\psi\eta$	e - π	90	5.6	91	5.5	90	5.6	90	5.5
8.847	$D_s^+ D_{s0}^{*-}$	π - p	5	4.4	9	5.0	11	5.2	20	4.5
		K - p ●	53	3.4	53	2.3	59	3.8	61	2.4
10.000	$\Lambda^0 \bar{\Lambda}^0$	π - K	17	4.0	20	3.1	28	5.0	28	3.4
		π - p	32	3.5	43	3.4	41	4.3	71	4.3
		p - π	17	5.6	19	5.4	19	5.5	23	5.0
10.295	$J/\psi 2\pi^0$	e - π	93	5.6	93	5.5	92	5.6	93	5.5
		μ - π	97	1.3	97	1.2	97	1.3	97	1.2
	$J/\psi\pi^+\pi^-$	e - π	93	5.6	93	5.5	93	5.6	93	5.5
		μ - π	98	1.3	98	1.2	98	1.3	98	1.2
10.900	e^+e^-	e - π ●	90	5.6	91	5.5	91	5.6	91	5.4
12.000	$D^{*0}\bar{D}^{*0}\gamma$	π - p	10	5.8	12	5.6	13	5.9	20	5.0
		K - p	20	5.4	22	5.2	27	5.5	28	4.4
	$D_s^+ D_s^- \gamma$	π - p	16	4.1	23	4.0	22	4.6	38	4.5
		K - p	33	3.4	34	2.7	39	3.8	40	2.6
	$\phi\phi$	K - π	41	5.3	41	5.1	44	5.3	44	5.0
	$D^+D^-\gamma$	π - p	17	3.6	22	3.5	24	4.3	38	4.2
		K - p	26	4.1	27	3.5	33	4.5	34	3.3
	$D^0\bar{D}^0\gamma$	π - p	11	5.6	14	5.5	15	5.6	22	4.8
		K - p	22	5.1	24	5.0	29	5.3	29	4.3
	$D^{*+}D^{*-}\gamma$	π - K	31	4.4	32	3.4	34	4.5	33	3.4
		π - p	24	4.4	37	5.1	27	4.8	45	5.1
		K - p	22	4.9	24	4.6	30	5.2	30	4.0
	$\phi\phi$	K - π	41	5.3	42	5.1	44	5.3	44	5.0
12.349	$J/\psi 2\pi^0$	e - π	93	5.6	93	5.5	93	5.6	93	5.5
		μ - π	98	1.3	98	1.2	98	1.3	98	1.2
	$J/\psi\pi^+\pi^-$	e - π	93	5.6	93	5.5	93	5.6	93	5.5
		μ - π	98	1.3	98	1.2	98	1.3	98	1.2
15.000	$D^+D^-\gamma$	π - μ	22	3.3	22	3.2	22	3.2	23	3.3
		π - p	17	3.5	20	3.4	22	4.3	35	4.1
		K - p	24	4.1	26	3.5	30	4.3	31	3.2
	e^+e^-	e - π	90	5.6	89	5.4	89	5.6	90	5.5
	$D^{*+}D^{*-}\gamma$	π - μ	30	3.6	30	3.6	31	3.6	30	3.7
		π - K	25	3.9	26	3.0	27	4.1	28	2.9
		π - p	21	4.1	36	4.8	25	4.4	43	4.8
		K - π	22	5.3	22	5.1	24	5.4	24	5.0
		K - p	21	4.6	23	4.3	27	4.9	27	3.9
	$D^{*0}\bar{D}^{*0}\gamma$	K - p	19	5.1	20	4.8	25	5.3	25	4.2
	$\phi\phi$	K - π ●	51	4.8	52	4.7	54	4.9	53	4.6
	$D_s^+ D_s^- \gamma$	π - μ	23	3.4	22	3.3	22	3.4	23	3.4
		π - p	17	3.9	22	3.8	22	4.4	36	4.3
		K - p	30	3.3	30	2.8	34	3.7	34	2.7
	$\phi\phi$	K - π	51	4.8	52	4.6	53	4.9	53	4.5
	$D^0\bar{D}^0\gamma$	K - π	24	5.4	24	5.1	25	5.4	26	5.0
		K - p	18	5.0	20	4.6	24	5.2	24	4.1

Table 12: Table of projection results (2). Marked channels (●) appear in figs. 59 – 61.

6   Global PID Scheme

The PANDA spectrometer will feature a complete set of innovative detectors for particle identification. The detection of neutral particles will be performed by a highly granular electromagnetic calorimeter. Charged particles will be identified in the low momentum region by their energy deposit and ToF, in all other momentum regions by innovative DIRC detectors. The target spectrometer will be complemented by a forward spectrometer to detect high momentum particles and surrounding muon detectors. Each detector systems performance is optimised in itself. Studies have begun to combine the responses of various detectors in a common framework based on a likelihood scheme or a carefully trained neutral network. These combined likelihood schemes are successfully employed at various detector systems like HERMEs, Belle and BaBar. They rely on a reliable parametrisation of the detector component response from simulation and test-beams. This has to be taken into account in testing PANDA's individual components. The combined performance of the system will be significantly better than the individual separation powers.

7 Conclusion

In this report of the PANDA PID TAG

    all informations about the PID detectors of PANDA and their performance are gathered.

    the separation power is declared as the indication to determine the detector performance

    the Fast Simulation was explained as the tool for the overall treatment.

    parameterizations to evaluate Separation Power Maps we described. Simulations for some of the subsystems with other tools than the Fast Simulation verify the correctness of the approach with the Fast Simulation.

    Parameters (f and σ_{avg}) were found to evaluate the ability of detectors and systems.

The Pid TAG gives no recommendations but numbers and a clue how to read them. They are strong and serve as a basis for decisions to be take by the PANDA collaboration.

8   Acknowledgments

References

[1] P̄ANDA Collaboration, Technical Progress Report, FAI R-ESAC/Pbar 2005

[2] http://panda-wiki.gsi.de/cgi-bin/viewauth/Tagpid/WebHome, Wiki page of the P̄ANDA PID TAG

[3] F. Sauli, Nucl. Instrum. Meth. **A386**, 531 (1997)

[4] http://cnlart.web.cern.ch/cnlart/237/Pr/garfield.html

[5] "The HARP resistive plate chambers: Characteristics and physics performance", V.Ammosov et al., NIM **A578** (2007) 119-138

[6] "Four glass RPC as a candidate to a large area thin time-of-flight detector", V.Ammosov et al., preprint IHEP 2002-10, Protvino 2002

[7] "Prototype Performance on Novel Muon Telescope Detector at STAR", Lijuan Ruan (for the STAR), 24th Winter Workshop on Nuclear Dynamics, South Padre, USA, April 5-12 2008

[8] IHEP+JINR proposal, PANDA Workshop, ITEP, Moscow, April 17-18 2008,
$http://www-panda.gsi.de/html/panda\_russia/HARP\_PANDA\_ITEP.ppt$

[9] R. Aleksan et al., Nucl. Inst. Meth. **A397**, 261 (1997)

[10] http://www.zemax.com

[11] A. Galoyan, V.V. Uzhinsky, AIP Conf. Proc. 796, pp. 79-8 2, 2005

[12] P. Schönmeier et al., to appear in the proceedings of 6th In ternational Workshop on Ring Imaging Cherenkov Counters (RICH 2007), Trieste, It aly, 15-20 Oct 2007.

[13] The HERMES Dual-Radiator Ring Imaging Cerenkov Detector, N. Akopov et al.Nucl.Instrum.Meth.A479:511-530,2002

[14] A Review of recent techniques of TOF detectors, M.Bonesini, Publ. in Como 2003, Astroparticle, particles and space physics, detectors and medical physics applications, 455-461

[15] Characterization of the HADES spectrometer in PP collisions at 2.2 GeV: Elastic Scaterring and Eta reconstructions. Stefano Spatario PhD thesis.

[16] W.-M. Yao et al. 2006 J. Phys. G: Nucl. Part. Phys. **33** 1

[17] G.S. Atoyan et al., Nucl. Instrum. Meth. **A320**, 144 (1992)

[18] G. Atoyan et al., Test beam study of the KOPIO Shashlyk calorimeter prototype, in *Proceedings of "CALOR 2004"*, 2004

[19] Acta Phys. Polon. **B38**, 899 (2007)

9 Appendix

Members of the PID TAG

- G. Schepers, C. Schwarz - Barrel Dirc (Chairs)

- B. Kopf, R. Novotny - Barrel Calorimeter

- B. Seitz - Cherenkov Counter (Global PID)

- O. Denisov / M. P. Bussa - Muon Counter

- K. Föhl / P. Vlasov - Forward Cherenkov

- J. Smyrski / O. Wronska - Forward Calorimeter

- Q. Weitzel / S. Neubert - Time Projection Chamber

- C. Schwarz, A. Galoyan - Time of Flight

- K. Götzen - Fast Simulation

- K. Peters - Physics